

# INAUGURAL-DISSERTATION

zur  
Erlangung der Doktorwürde  
der  
Naturwissenschaftlich-Mathematischen  
Gesamtfakultät  
der  
Ruprecht-Karls-Universität  
Heidelberg



vorgelegt von

**Dipl.-Phys. Jürgen C. Reich**

aus Schwäbisch Hall

Tag der mündlichen Prüfung: 25.11.1999



# Winkelkorrelationen im Zerfall polarisierter Neutronen

Gutachter: Prof. Dr. Dirk Dubbers  
Prof. Ph.D. Jürgen v. Krogh



Dissertation  
submitted to the  
Combined Faculties for the Natural Sciences and for Mathematics  
of the Rupertus Carola University of  
Heidelberg, Germany  
for the degree of  
Doctor of Natural Sciences

# Angular Correlations in Polarized Neutron Decay

presented by  
Diplom-Physicist: **Jürgen C. Reich**  
born in: Schwäbisch Hall

Heidelberg, 25.11.1999

Referees: Prof. Dr. Dirk Dubbers  
Prof. Ph.D. Jürgen v. Krogh



# Winkelkorrelationen im Zerfall polarisierter Neutronen

Das große Interesse am Neutronenzerfall kommt daher, daß er als einfachster Baryonenzerfall theoretisch gut verstanden ist. Im Vergleich zu Kernzerfällen sind die strukturabhängigen Korrekturen, die aus der Bindung durch die starke Kraft kommen, klein. Das Neutron kann in diesem Sinn als elementares Teilchen angesehen werden. Damit eignen sich Präzisionsmessungen der Zerfallsparameter, wie Winkelkorrelationen und Lebensdauer, zur Untersuchung der dem Zerfall zugrundeliegenden schwachen Wechselwirkung. PERKEO II ist ein Spektrometer zum Nachweis von Elektronen, das speziell zur Messung von Winkelkorrelationen im Zerfall polarisierter Neutronen optimiert wurde.

Im ersten Teil dieser Dissertation wird eine neue Messung der Korrelation zwischen Richtung des Elektronenimpulses und Stellung des Neutronenspins vorgestellt. Die Auswertung ergab den bisher genauesten Wert für den entsprechenden Korrelationskoeffizienten:  $A = -0.1189(8)$ . In Kombination mit der Neutronenlebensdauer und der Fermi-Kopplungskonstanten führt dies zu einer Verletzung der Unitarität der CKM Matrix mit  $\sim 3\sigma$  und ist damit ein Hinweis auf Physik jenseits des Standardmodells.

Die Vorbereitung einer Messung der Korrelation zwischen (Anti-)Neutrinoemissionsrichtung und Neutronenspin ist Inhalt des zweiten Teils dieser Arbeit. Das Neutrino muß indirekt über koinzidenten Nachweis des Elektrons und des Protons beobachtet werden, wobei die Besonderheit darin besteht, daß Protonen und Elektronen in demselben Detektor registriert werden sollen. Die Testmessungen mit dem konstruierten Protonendetektor und Simulationen zur optimalen Integration in das PERKEO II Spektrometer werden präsentiert.

## Angular Correlations in the Decay of Polarized Neutrons

Neutron decay, being the simplest baryonic beta decay, is well understood theoretically. The structure dependent corrections, due to the binding by the strong force, are small compared to the case of nuclear decays. In this sense the neutron can be regarded as a true elementary particle. Thus neutron decay parameters, like angular correlations and the lifetime, are well suited to examine the weak interaction leading to the decay. PERKEO II is an electron spectrometer, dedicated to the measurement of angular correlations in the decay of polarized neutrons.

A new measurement of the correlation between electron emission rate and neutron spin direction is presented in the first part of this dissertation. The result is the most precise determination of the corresponding correlation coefficient:  $A = -0.1189(8)$ . This leads, in combination with the value of the neutron lifetime and the Fermi coupling constant, to a violation of the unitarity condition of the CKM matrix on the level of  $\sim 3\sigma$ , presenting an indication for physics beyond the standard model.

The second part of this thesis treats the preparation of a measurement of the correlation between (anti-)neutrino emission and neutron spin. The neutrino momentum direction has to be inferred from a coincident detection of electron and proton which in our scheme will be achieved in only one detector. The performance of the detector is discussed and simulations regarding its integration into the PERKEO II spectrometer are presented.



# Contents

<b>Abstracts</b>	<b>i</b>
<b>1 Introduction</b>	<b>1</b>
<b>2 Theory</b>	<b>3</b>
2.1 Historical overview . . . . .	3
2.2 Recoil terms . . . . .	6
2.3 Goldberger Treiman Relation . . . . .	8
2.4 Observables in neutron decay . . . . .	8
2.5 Radiative corrections . . . . .	12
<b>3 Instrument</b>	<b>15</b>
3.1 Measurement principle . . . . .	15
3.1.1 The setup of the experiment . . . . .	15
3.1.2 The spectrometer . . . . .	16
3.1.3 Shielding . . . . .	18
3.2 Effects of the magnetic field gradient . . . . .	19
3.2.1 Magnetic mirror effect . . . . .	19
3.2.2 Stern Gerlach effects . . . . .	20
3.3 Detector response function . . . . .	21
3.3.1 Pedestal and threshold . . . . .	22
3.3.2 Detector calibration . . . . .	23
3.3.3 Detector drifts and rebinning . . . . .	32
3.3.4 Edge effect . . . . .	33
3.4 Backscattering . . . . .	34
3.4.1 Time resolution . . . . .	34
3.4.2 Threshold effect in backscattered events . . . . .	37

<b>4</b>	<b>The <math>A</math> measurement</b>	<b>41</b>
4.1	Polarization analysis . . . . .	41
4.1.1	Mathematical description . . . . .	42
4.1.2	The wavelength cutter . . . . .	44
4.1.3	Supermirror polarization analysis . . . . .	44
4.1.4	Polarized $^3\text{He}$ spin filter . . . . .	47
4.1.5	Spin filter versus supermirror analyzer . . . . .	49
4.1.6	The polarization monitor . . . . .	50
4.2	Background . . . . .	50
4.2.1	Beam independent background . . . . .	51
4.2.2	Beam dependent background . . . . .	52
4.2.3	The effect on the asymmetry . . . . .	55
4.3	Determination of the correlation coefficient $A$ . . . . .	56
4.3.1	Beta spectra . . . . .	56
4.3.2	Experimental Asymmetry . . . . .	57
4.3.3	Summary of systematic effects . . . . .	59
4.4	Comparison with other experiments . . . . .	61
4.5	Implications of the result . . . . .	62
4.5.1	Unitarity of the CKM matrix . . . . .	62
4.5.2	Goldberger Treiman relation . . . . .	65
4.5.3	Right handed currents . . . . .	66
<b>5</b>	<b>Preparations for the <math>B</math> measurement</b>	<b>69</b>
5.1	The measurement principle . . . . .	69
5.2	Statistical sensitivity . . . . .	71
5.3	Systematic effects . . . . .	72
5.3.1	Proton time of flight . . . . .	72
5.3.2	Magnetic mirror effect . . . . .	75
5.3.3	Accidental coincidences . . . . .	76
5.3.4	The potential of the neutron beam . . . . .	78
5.3.5	Primary electrons and high voltage . . . . .	79
5.3.6	Summary of design criteria . . . . .	80
5.4	Detector design . . . . .	80
5.5	Test measurements . . . . .	82

<b>6 Summary</b>	<b>89</b>
<b>A The fit function for the experimental asymmetry</b>	<b>91</b>
<b>Acknowledgements</b>	<b>95</b>
<b>Bibliography</b>	<b>97</b>



# Chapter 1

## Introduction

In weak interactions parity is violated. That means, there is a real fundamental difference between ‘right’ and ‘left’, between the world as we see it and its mirror image. This has been demonstrated first in the famous Wu experiment [Wu57] upon a suggestion by Lee and Yang [Lee56]. In the meantime this fact has been verified in numerous experiments, yet the basic origin of this symmetry violation remains unexplained. In the standard model of particle physics parity violation is merely incorporated by requiring that only left-handed particles can take part in the weak interaction. Left-handedness implies for an electron that its momentum is oriented predominantly antiparallel to its spin while for an antineutrino momentum and spin are parallel to each other.

Due to the weak interaction a free neutron decays into a proton, an electron and an (electron-) antineutrino. All these particles have two possible spin states, referred to as ‘up’ and ‘down’. When a neutron with spin up decays into a proton with spin down, the electron and the antineutrino both have to be in the spin up state in order to conserve total spin (Fig. 1.1). Therefore, the electron will be emitted mostly antiparallel and the antineutrino parallel to the neutron spin. The coupling constant in this type of decay is  $C_A$ .

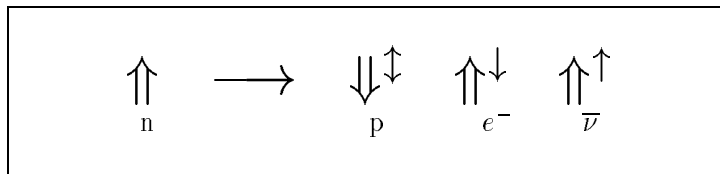


**Figure 1.1:** Neutron decay with spin flip: the double arrows indicate the spins of the particles, whereas the small arrows indicate the preferred directions of the momenta.

In the other case, when the proton spin points in the same direction as the neutron spin, the spins of the electron and the antineutrino have to cancel. With no preferred direction of the electron and neutrino spins their handedness does not lead to an emission asymmetry (Fig. 1.2). The coupling constant  $C_V$  leads only to this kind of transitions<sup>1</sup>.

---

<sup>1</sup>This simple picture ignores that there is also a Gamow Teller amplitude leading to no spin change for the nucleons that interferes with the Fermi amplitude. This interference does lead to an additional contribution to the asymmetry as will be discussed later.

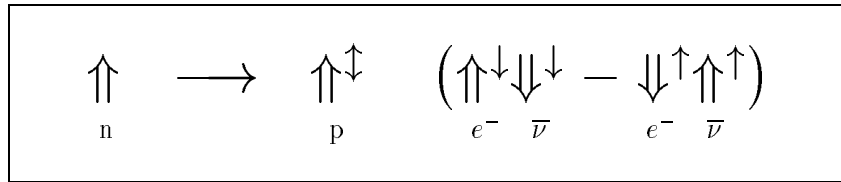


**Figure 1.2:** Neutron decay without spin flip: the double arrows indicate the spins of the particles, whereas the small arrows indicate the preferred directions of the momenta.

As it turns out, measuring the asymmetry of the electron emission in polarized neutron decay is the most sensitive way to determine the ratio of the two coupling constants  $\lambda = C_A/C_V$ . It is important to measure  $\lambda$  because it can not yet be calculated precisely while its knowledge is required in many fields ranging from particle physics to cosmology [Dub91]. One example is the expected neutrino flux from the sun that strongly depends on the value of  $\lambda$  since it determines the rate of the primary hydrogen fusion reaction.

Nowadays, the measurements have reached a precision allowing not only to determine the coupling constants but rather to use their values to test the validity of the standard model of particle physics and to set limits on possible extensions. Namely from the electron asymmetry and from the value of the neutron lifetime, the coupling constants  $C_A$  and  $C_V$  are obtained separately. The coupling constant  $C_V$ , together with the Fermi coupling constant  $G_F$  known from muon decay, can be used to check the unitarity condition of the CKM matrix (Section 4.5.1), while  $C_A$  presents a link to the strong interaction, i.e. via the Goldberger Treiman relation (Section 4.5.2). Possible extensions of the standard model that would actually explain the origin of parity violation are so-called left-right symmetric models (Section 4.5.3). The electron and the neutrino asymmetry yield complementary information with regard to these models since they are sensitive to different parameters. In this way, the angular correlation measurements may even shed light on the origin of parity violation.

In this thesis a new measurement of the correlation between electron momentum and neutron spin is presented. Chapter 2 provides a review of the relevant theoretical background. The spectrometer PERKEOII, dedicated to the determination of angular correlations in polarized neutron decay, is described in Chapter 3. In Chapter 4, the measurements leading to the new evaluation of the electron asymmetry are shown and the result is discussed. The preparations for a measurement of the neutrino asymmetry, including the construction and testing of a proton detector as well as simulations of the experimental realization, are treated in Chapter 5.

# Chapter 2

## Theory

In this chapter an overview over the theory of neutron decay is given. The motivation for studying the weak interaction by doing neutron decay experiments lies in the relative simplicity of the theory. Experiments using nuclear beta decay involve nuclear structure dependent corrections that do not exist in neutron decay. With increasing experimental precision the uncertainties in these corrections became more and more important. The neutron, being the simplest baryonic beta decay, offers a high potential for precision tests of the standard model less troubled by theoretical corrections. The disadvantages are the difficulty of the experiments and the usually limited statistics. In this sense, the interest in neutron decay studies can be understood as development from ‘simple’ nuclear experiments with more complicated theory to more difficult experiments with easier theory driven by the increasing availability of neutrons and the development of new experimental techniques.

### 2.1 Historical overview

The first working theory<sup>1</sup> of beta decay was invented by Fermi [Fer34] shortly after the proposition of the neutrino by Pauli [Pau33]. This original theory was formulated in close analogy to quantum electrodynamics. Even though it was based on little experimental evidence at the time, the basic form is still in use. In quantum electrodynamics the interaction of an electron with the electromagnetic field is given by the Lagrangian density :

$$\mathcal{L} = -j_\mu A^\mu , \tag{2.1}$$

where

$$j_\mu = e\bar{\Psi}\gamma_\mu\Psi \tag{2.2}$$

is the electromagnetic current density and  $A^\mu$  is the 4-vector potential of the electromagnetic field. The Feynman graph corresponding to this process is shown in Fig. 2.1. In Fermi’s model the electric charge  $e$  is replaced by the Fermi coupling constant  $G_F$ , the electromagnetic

---

<sup>1</sup>This chapter follows mostly Commins [Com73][Com83] and Holstein [Hol74].

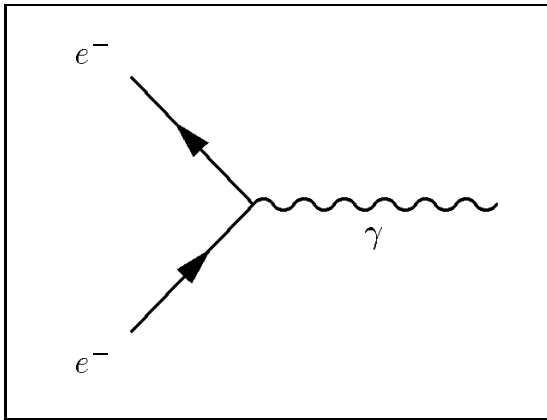


**Figure 2.1:** The Feynman graph showing the coupling of an electron to a virtual photon.

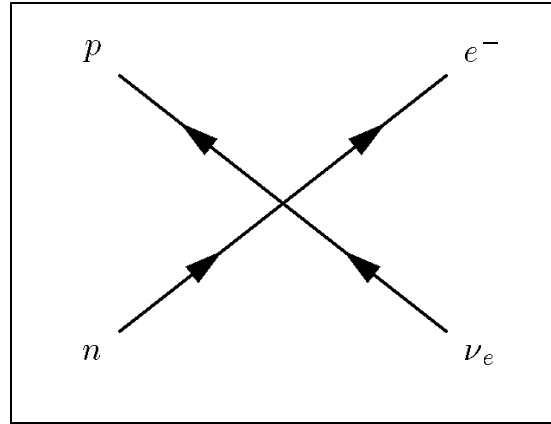


**Figure 2.2:** The Feynman graph of the current-current interaction of neutron decay.

current by a leptonic current and the 4-vector potential by a hadronic current<sup>2</sup>. Hence the resulting interaction is called a current-current interaction:

$$\mathcal{L} = \frac{G_F}{\sqrt{2}} \bar{\Psi}_p \gamma_\mu \Psi_n \cdot \bar{\Psi}_e \gamma^\mu \Psi_\nu + h.c. \quad (2.3)$$

The corresponding Feynman graph of such a current-current interaction is shown in Fig. 2.2. Since both currents transform like polar vectors under Lorentz transformations, the Lagrangian density is a true scalar. In nuclear weak interactions, including neutron decay, the hadrons are always non relativistic. Thus the non relativistic approximation is excellent for the hadronic current. This approximation leads to the selection rule  $\Delta J = 0$  for the hadronic current defined in Eq. (2.3), limiting this Lagrangian to decays without spin change.

However, one can use more terms to build a scalar Lagrangian density using the Dirac fields for the particles. The most general scalar Lagrangian density assuming Lorentz invariance is:

$$\mathcal{L} = \frac{G_F}{\sqrt{2}} \sum_i C_i \bar{\Psi}_p O_i \Psi_n \cdot \bar{\Psi}_e O_i \Psi_\nu, \quad (2.4)$$

where the operators  $O_i$  represent the  $4 \times 4$  matrices  $I$ ,  $\gamma_\mu$ ,  $\sigma_{\mu\nu}$ ,  $\gamma_\mu \gamma_5$  and  $\gamma_5$  that transform as scalar, polar vector, second rank tensor, axial vector and pseudo scalar respectively. The  $C_i$  are the corresponding coupling constants that have to be determined from experiment. The non relativistic approximation for the hadronic current in each of these terms leads to the pseudo scalar coupling being negligible, for the scalar and vector coupling it leads to the Fermi selection rule  $\Delta J = 0$ , and for the tensor and axial vector coupling to the Gamow Teller<sup>3</sup> selection rule  $\Delta J = 0, 1$  (no  $0 \rightarrow 0$ ). Thus in transitions with  $\Delta J = 1$  the axial vector and tensor coupling can interfere, as can the vector and scalar couplings in  $0 \rightarrow 0$  transitions. These are the so-called Fierz interferences. Since experimentally these interference terms were not found, one was able to conclude that only one of either the scalar and vector couplings and one of either the tensor and the axial vector couplings dominate.

<sup>2</sup>Considering the case of neutron decay.

<sup>3</sup>Gamow and Teller first suggested this generalization of Fermi's theory.

However, another complication arose due to the discovery of parity violation. This is implemented in Eq.(2.4) by rewriting it :

$$\mathcal{L} = \frac{G_F}{\sqrt{2}} \sum_i \bar{\Psi}_p O_i \Psi_n \cdot \bar{\Psi}_e O_i (C_i - C'_i \gamma_5) \Psi_\nu. \quad (2.5)$$

The newly introduced couplings  $C'_i$  lead to each  $O_i$  having a scalar and a pseudo scalar contribution to  $\mathcal{L}$  thus leading to parity violation in the observables. Experimentally, the scalar and tensor couplings were shown to be consistent with zero and  $C_V = C'_V$  and  $C_A = C'_A$  was found for the vector and axial vector couplings (see [Boo84], [Ade93], [Glü95]). Using these results one can rewrite Eq. (2.5) as:

$$\mathcal{L} = \frac{G_F}{\sqrt{2}} \bar{\Psi}_p \gamma_\mu (C_V - C_A \gamma_5) \Psi_n \cdot \bar{\Psi}_e \gamma^\mu (1 - \gamma_5) \Psi_\nu. \quad (2.6)$$

The theory was then generalized to the so-called V-A law. There, the weak Lagrangian density is written as:

$$\mathcal{L} = \frac{G_F}{\sqrt{2}} J_\lambda^\dagger J^\lambda. \quad (2.7)$$

Where the currents  $J_\lambda = J_\lambda^{lept} + J_\lambda^{hadr}$  each contain a leptonic and a hadronic part, with both parts being of the V-A form. Thus Eq.(2.7) describes purely leptonic, purely hadronic and mixed weak decays. That all these processes can be described in the same framework with one coupling constant  $G_F$  is called the universality of weak interactions. The hadronic current is described on the quark level. In neutron decay a down quark is transformed into an up quark. However, there are also flavor changing weak decays, e.g. the decay of the Kaon where a strange quark transforms into an up quark. This can be accounted for by assuming that the weak quark eigenstates are not the same states as the mass eigenstates. The corresponding transformation from one basis to the other is done by the Cabibbo-Kobayashi-Maskawa (CKM) matrix [Kob73] [Cab63]:

$$\begin{pmatrix} d \\ s \\ b \end{pmatrix}_{\text{weak}} = \begin{pmatrix} V_{ud} & V_{us} & V_{ub} \\ V_{cd} & V_{cs} & V_{cb} \\ V_{td} & V_{ts} & V_{tb} \end{pmatrix}_{\text{CKM}} \cdot \begin{pmatrix} d \\ s \\ b \end{pmatrix}_{\text{mass}}. \quad (2.8)$$

This hypothesis accounts for the relative coupling strength of strangeness conserving and strangeness changing weak decays, thus saving the universality of the weak interaction. Including the appropriate matrix element  $V_{ud}$ , the correct V-A Lagrangian for neutron decay is given by:

$$\mathcal{L} = V_{ud} \frac{G_F}{\sqrt{2}} \bar{\Psi}_p \gamma_\mu (C_V - C_A \gamma_5) \Psi_n \cdot \bar{\Psi}_e \gamma^\mu (1 - \gamma_5) \Psi_\nu. \quad (2.9)$$

The shortcoming of such a theory, however, is that it is not renormalizable, i.e. the calculated cross section for neutrino electron scattering diverges for high energies, even taking higher order corrections into account. This problem was solved in the standard model. There

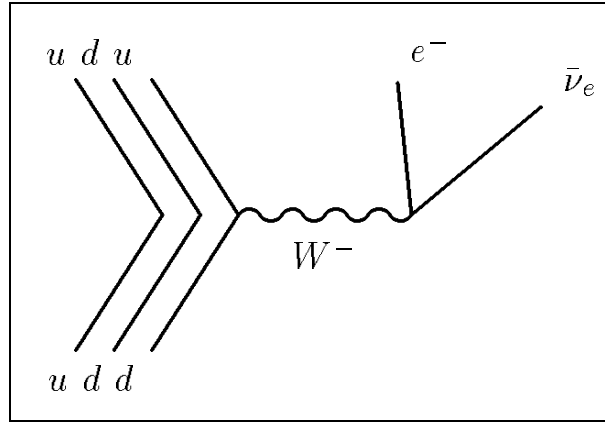


**Figure 2.3:** The Feynman graph describing neutron decay in the standard model.

the electromagnetic and the weak interactions are unified in the Glashow-Salam-Weinberg theory [Gla61][Sal68][Wei67]. The interaction is described on the quark level, i.e. pointlike quarks and leptons and is mediated by the exchange of vector bosons. The corresponding Feynman graph describing neutron decay is shown in Fig. 2.3. The vector bosons lead to an additional term in the Lagrangian density, the propagator:

$$G_V^{\mu\nu}(q^2) = \frac{-g^{\mu\nu} + \frac{q^\mu q^\nu}{M^2}}{q^2 - M^2}, \quad (2.10)$$

where  $q$  is the momentum transfer and  $M$  is the boson mass. For energies small compared to the boson mass the propagator is a constant, explaining why the current-current interaction is sufficient for nuclear beta decay. Like in the V-A theory, parity violation is included in the standard model without explanation of its origin. In the standard model this is achieved by placing only the left-handed particles in SU(2) doublets whereas the right-handed particles are singlets under SU(2) transformations and therefore do not participate in the weak interaction. This leads to the V-A form of the Lagrangian due to the projection operator for left-handed particles:

$$\Psi_L = \frac{1}{2}(1 - \gamma_5)\Psi. \quad (2.11)$$

## 2.2 Recoil terms

Due to the neutron being a composite object two modifications appear. The first modification is that in the nuclear medium the coupling constants are changed to effective coupling constants that differ from the ones on the quark level. The other modification appears when corrections due to nucleon recoil are included. Since nucleons are extended objects, structure functions are introduced. These allow to describe the nucleons by their spins and momenta with all the internal structure dependent effects being included in the structure functions (or form factors). In the hadronic current all terms are included that transform as vector or axial

vector under Lorentz transformations (Holstein's notation [Hol74]):

$$\begin{aligned} J_\mu^{hadr} &= \bar{\Psi}_f (V_\mu + A_\mu) \Psi_i \\ \bar{\Psi}_f V_\mu \Psi_i &= \bar{\Psi}_f \left[ g_V \gamma_\mu + \frac{1}{2M} g_S q_\mu - i g_{WM} \frac{1}{2M} \sigma_{\mu\nu} q^\nu \right] \Psi_i \end{aligned} \quad (2.12)$$

$$\bar{\Psi}_f A_\mu \Psi_i = \bar{\Psi}_f \left[ g_A \gamma_\mu \gamma_5 + \frac{1}{2M} g_P q_\mu \gamma_5 - i g_{II} \frac{1}{2M} \sigma_{\mu\nu} q^\nu \gamma_5 \right] \Psi_i \quad (2.13)$$

All form factors ( $g_V, g_A, g_S, g_P, g_{WM}, g_{II}$ ) can only be functions of  $q^2$ , since this is the only Lorentz invariant variable available. In the limit where  $q^2 = 0$  the form factors  $g_V$  and  $g_A$  can be identified with the coupling constants  $C_V$  and  $C_A$  in the infinite nucleon mass or allowed approximation, Eq. (2.9). The other terms are referred to as the induced form factors:  $g_S, g_P$  induced scalar and pseudo scalar form factor,  $g_{WM}, g_{II}$  weak magnetism and induced tensor form factors. And  $M$  is the average of the initial and final nucleon mass.

These form factors can be further restricted using symmetry arguments. In Eq. (2.2) the electromagnetic current of a pointlike particle was used. For a spin  $\frac{1}{2}$  baryon, including recoil terms, the electromagnetic current is:

$$\bar{\Psi} J_\mu^{em} \Psi = \bar{\Psi} \left[ f_V \gamma_\mu + \frac{1}{2M} f_S q_\mu - i f_M \frac{1}{2M} \sigma_{\mu\nu} q^\nu \right] \Psi. \quad (2.14)$$

From the continuity equation, the Dirac equation and the fact that  $\sigma_{\mu\nu}$  is antisymmetric  $f_S = 0$  can be derived [Com73]. Here  $f_V(q^2 = 0)$  is the charge and  $f_M(q^2 = 0)$  is the anomalous magnetic moment of the baryon. This explains the introduction of the factors  $1/2M$  leading to  $f_M$  being expressed in units of the nuclear magneton<sup>4</sup>. Using isospin, proton and neutron can be described together:  $\Psi = \begin{pmatrix} p \\ n \end{pmatrix}$  leading to:

$$\begin{aligned} \bar{\Psi} J_\mu^{em} \Psi &= \bar{\Psi} \left\{ \left[ (f_{V,p} + f_{V,n}) \gamma_\mu - i (f_{M,p} - f_{M,n}) \frac{1}{2M} \sigma_{\mu\nu} q^\nu \right] + \right. \\ &\quad \left. \left[ (f_{V,p} - f_{V,n}) \gamma_\mu - i (f_{M,p} - f_{M,n}) \frac{1}{2M} \sigma_{\mu\nu} q^\nu \right] I_3 \right\} \Psi. \end{aligned} \quad (2.15)$$

The first line is an isoscalar contribution whereas the second line corresponds to the third component of an isovector, with  $I_3$  being the third Pauli (iso)spin matrix. In Eq. (2.12) the isospin matrices have been omitted. Since a proton is changed in a neutron or vice versa, there are isospin raising ( $I^+$ ) and lowering ( $I^-$ ) operators required, leading for the vector part, Eq. (2.12), to:

$$V_\mu^{W\pm} = \bar{\Psi}_f V_\mu I^\pm \Psi_i. \quad (2.16)$$

The conserved vector current hypothesis now states that the isovector part of the electromagnetic current and the (polar) vector part of the weak currents form one isospin triplet of conserved currents. The conservation of the currents (weak form of CVC) implies that  $C_V = 1$ , and putting them in one isospin triplet (strong form of CVC) directly leads to the equality of the corresponding form factors. Namely:

$$g_S = f_S = 0 \quad (2.17)$$

$$g_{WM} = f_{M,p} - f_{M,n} = 3.7 \quad (2.18)$$

---

<sup>4</sup>In this section  $\hbar = c = 0$  is used.

A symmetry valid in the strong interaction is called  $G$ -parity, which is a combination of the charge conjugation operation  $C$  and a rotation by  $\pi$  in isospin space:

$$G = C \cdot e^{i\pi I_2}. \quad (2.19)$$

The form factors can be classified according to their transformation properties under  $G$ -parity [Wei58]. In the vector current  $g_S$  transforms with the opposite sign as  $g_V$  and in the axial current  $g_{II}$  transforms with the opposite sign as  $g_A$ , therefore  $g_S$  and  $g_{II}$  are denoted second class currents and the other ones first class<sup>5</sup>. In the standard model second class currents are not allowed [Com73] and experimentally none have been found so far.

## 2.3 Goldberger Treiman Relation

There are several connections between weak interactions and strong interactions. The axial vector is not conserved, meaning that in a system bound by strong interactions the value of the axial vector coupling constant,  $C_A$ , depends on the medium. While on the quark level its value is 1, it changes to about 1.27 for neutron decay and decreases again for nuclear decays where the axial vector coupling strength depends on the individual decay. Also, if the axial current was conserved the pion would not decay. In the limit that the pion is massless ( $m_\pi/M \approx 15\%$ ) the axial vector can be considered conserved. This partially conserved axial vector hypothesis then leads to the Goldberger Treiman relation, connecting the axial vector coupling constant to pion decay parameters:

$$f_\pi g_{\pi NN} \approx C_A \frac{M_n + M_p}{2}. \quad (2.20)$$

Here  $f_\pi$  is the pion decay constant with  $\sqrt{2}f_\pi = 130.7 \pm 0.1 \pm 0.36$  MeV and  $g_{\pi NN}$  is the pion nucleon coupling constant. On a more fundamental level the Goldberger Treiman relation is a consequence of the approximate chiral symmetry of the strong interaction [Pag75]. In this sense the Goldberger Treiman relation is useful to actually measure the deviation from this symmetry.

## 2.4 Observables in neutron decay

The observables in neutron decay are the neutron lifetime and the spins and momenta of all the particles involved. The lifetime is calculated using Fermi's golden rule. From the phase space of the decay the electron energy distribution is obtained:

$$d\phi \propto (E_0 - E)^2 \sqrt{E^2 - m_e^2} (E + m_e) dE = F(E) dE. \quad (2.21)$$

Here  $E_0 = 782$  keV is the maximum electron energy and  $E$  is the kinetic energy of the electrons. This distribution has to be modified:

$$F(E)' = F(E)(1 + \delta_R(E))(1 + R_0(E))F_C(E), \quad (2.22)$$

---

<sup>5</sup>This is correct since neutron decay is a transition within an isotopic multiplet. For transitions outside an isotopic multiplet all form factors can have first and second class contributions making the experimental search for second class currents in transitions outside an isotopic multiplet more difficult [Bow99].

where the terms refer to external radiative corrections,  $\delta_R(E)$ , corrections for the proton recoil terms discussed above,  $R_0(E)$ , and Coulomb corrections,  $F_C(E)$ . These functions, changing the beta spectrum on the order of about 1%, are included in our fit function which is explicitly given in appendix A. In the electron spectrum the Matrix element  $|M|^2 = |C_V|^2 + 3|C_A|^2$  and the coupling strength  $G_F^2|V_{ud}|^2$  enters as well:

$$d\Gamma \propto G_F^2|V_{ud}|^2 F(E)' |M|^2 dE. \quad (2.23)$$

The decay rate and its inverse, the lifetime, is obtained by integration over the electron energy:

$$\tau = \frac{K/\ln 2}{f^R \cdot |C_V|^2} \frac{1}{1 + 3\lambda^2}. \quad (2.24)$$

The Fermi integral  $f^R = 1.71489(2)$  is the integral of  $F(E)'$  defined in Eq. (2.22) over the electron energy, containing essentially the phase space and the corrections, and  $K = (8120.271 \pm 0.012) \times 10^{-10} \times (\hbar c)^6 \text{ GeV}^{-4} \text{ s}$  is a combination of constants [Tow98].

For polarized neutron decay the most general decay probability, obeying Eq. (2.5), was given by Jackson [Jac57]<sup>6</sup>. Using only the terms relevant when the spins of the final state particles are not observed, it is:

$$d\Gamma = \frac{G_F^2|V_{ud}|^2}{(2\pi)^5} F(E)' |M|^2 dE d\Omega_e d\Omega_\nu \cdot \left\{ 1 + a \frac{\vec{p}_e \vec{p}_\nu}{EE_\nu} + \langle \vec{\sigma}_n \rangle \left[ A \frac{\vec{p}_e}{E} + B \frac{\vec{p}_\nu}{E_\nu} + D \frac{\vec{p}_e \times \vec{p}_\nu}{EE_\nu} \right] \right\}, \quad (2.25)$$

where  $\langle \vec{\sigma}_n \rangle$  is the neutron spin and  $\vec{p}_e, \vec{p}_\nu$  and  $E, E_\nu$  are the electron and neutrino momenta and energies respectively. The different correlation coefficients defined in this way are  $a$ , the correlation between electron and neutrino momentum, the two parity violating correlation coefficients  $A$  and  $B$  between neutron spin and electron and neutrino momentum respectively, and the triple correlation coefficient  $D$  that would violate time reversal invariance if found to be nonzero. In the V-A theory the correlation coefficients are all functions of  $\lambda = C_A/C_V$  the ratio of axial to polar vector coupling constants:

$$a = \frac{1 - |\lambda|^2}{1 + 3|\lambda|^2} \quad (2.26)$$

$$A = -2 \frac{|\lambda|^2 + \text{Re}(\lambda)}{1 + 3|\lambda|^2} \quad (2.27)$$

$$B = 2 \frac{|\lambda|^2 - \text{Re}(\lambda)}{1 + 3|\lambda|^2} \quad (2.28)$$

$$D = 2 \frac{\text{Im}(\lambda)}{1 + 3|\lambda|^2} \quad (2.29)$$

---

<sup>6</sup>One additional term due to Fierz interference appearing in the original work has been omitted, since here a V-A interaction is assumed. Actually, while in the calculations the general interaction Lagrangian as given in Eq. (2.5) was used, it was stated that the interaction was assumed to be primarily S and T as was the general opinion until one year later the V-A theory was published.

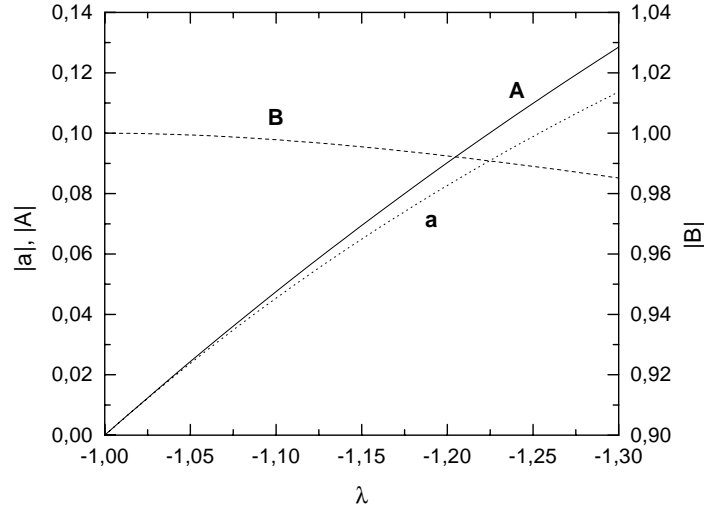


**Figure 2.4:** The correlation coefficients  $a$ ,  $A$  and  $B$  as functions of  $\lambda$ .

As can be seen from Fig. 2.4,  $a$  and especially  $A$  have the highest sensitivity to  $\lambda$ . The main interest in measuring  $B$  is the possibility to set limits on hypothetical right handed currents and the interest in measuring  $D$ , of course, is to look for time reversal and therefore CP violation. The lifetime  $\tau$  is needed in addition to  $\lambda$  to separately determine  $C_A$  and  $C_V$ , allowing for example to determine the  $V_{ud}$  matrix element and therefore to check the unitarity of the CKM matrix. For these reasons all these quantities are intensely studied. Due to recent developments in the techniques of neutron polarization and production, the precision of the experiments has increased and new experiments are being carried out and developed in a variety of groups. The current status as summarized by the particle data group for 1998 is given in Table 2.1

<i>Observable</i>	<i>Value</i>
$a$	$-0.102(5)$
$A$	$-0.1162(13)$
$B$	$0.983(4)$
$D$	$(-0.5 \pm 1.4) \times 10^{-3}$
$\tau$	$886.7 \pm 1.9$ s

**Table 2.1:** Summary of measured values for observables in neutron decay as given in [PDG98]<sup>7</sup>.

In the measurement of the electron asymmetry described here, only the electron is detected, but the neutrino (rather the proton) is not. Therefore Eq. (2.25) has to be integrated over the neutrino solid angle to obtain the electron distribution relative to the neutron spin:

$$d\Gamma \propto F(E)'dE d\Omega_e \{1 + A\beta \cos(\theta)\} . \quad (2.30)$$

<sup>7</sup>The uncertainty in  $A$  was scaled with a factor of 1.8 to account for disagreement between experiments. This will be discussed in more detail in Section 4.4.

The fact that  $A$  is close to zero and  $B$  is close to one can not be explained using such a simple picture as presented in the introduction<sup>8</sup>. The reason is that the values depend on the relative phase between the Fermi and Gamow Teller matrix elements. In general the correlation coefficients measure the average z-components of the lepton spins  $\langle m_e \rangle$  and  $\langle m_\nu \rangle$  as is derived in the ‘pedestrian approach’ [Lip62] to beta decay. However, their values can be deduced from angular momentum conservation only in the case of pure transitions. I.e. the decay of  $^{60}\text{Co}$  is a pure Gamow Teller transition since the nuclear spin changes from  $J_i = 5$  to  $J_f = 4$ . If the initial nucleus was polarized to  $\langle m_i \rangle = 5$ , it follows that both the leptons have to be polarized  $\langle m_e \rangle = \langle m_\nu \rangle = 1/2$  to conserve angular momentum. This corresponds to the case shown in Fig. 1.1. Therefore, both leptons are emitted asymmetrically with respect to the nuclear spin in a pure Gamow Teller transition. The lepton wave function in this case is:

$$|j_{\text{lep}}=1, m_{\text{lep}}=1 \rangle = | \uparrow \uparrow \rangle . \quad (2.31)$$

An example for a pure Fermi transition is the decay of  $^{10}\text{C}$  that has received interest recently as the lightest  $J = 0^+ \rightarrow 0^+$  transition [Fuj99]. In a pure Fermi transition the combined lepton spin is zero  $j_{\text{lep}} = 0$  and  $\langle m_e \rangle = \langle m_\nu \rangle = 0$  to conserve angular momentum (see Fig. 1.2). Thus both leptons are emitted isotropically as it has to be since there is no preferred axis in the nucleus. The lepton wave function in this case is:

$$|j_{\text{lep}}=0, m_{\text{lep}}=0 \rangle = \frac{1}{\sqrt{2}} (| \uparrow \downarrow \rangle - | \downarrow \uparrow \rangle) , \quad (2.32)$$

where the first arrow refers to the electron spin and the second one to the neutrino spin<sup>9</sup>.

However, neutron decay is an example of a mixed transition. In mixed transitions there is a third possible state for the leptons that is not allowed in pure transitions:

$$|j_{\text{lep}}=1, m_{\text{lep}}=0 \rangle = \frac{1}{\sqrt{2}} (| \uparrow \downarrow \rangle + | \downarrow \uparrow \rangle) , \quad (2.33)$$

corresponding to a Gamow Teller transition without spin change. If it was possible to observe this state alone it would not lead to an emission asymmetry as in the case of a pure Fermi transition. However, this state is only possible in a mixed transition and there it leads to an interference between the Fermi and the Gamow Teller matrix element. While both states by themselves lead to no asymmetry the interference term does, due to the different signs in Eqs. (2.32) and (2.33). This can be seen best by writing the total possible leptonic wave function for a mixed transition as:

$$|lept \rangle = a_{GT}^+ | \uparrow \uparrow \rangle + a_{GT}^- | \downarrow \downarrow \rangle + \frac{a_{GT} + a_F}{\sqrt{2}} | \uparrow \downarrow \rangle + \frac{a_{GT} - a_F}{\sqrt{2}} | \downarrow \uparrow \rangle , \quad (2.34)$$

where the different  $a$ ’s refer to the corresponding transition amplitudes. The probability for an electron to be emitted with spin up is then given by:

$$P(\uparrow) = \frac{1}{N} \left( |a_{GT}^+|^2 + \frac{1}{2} |a_{GT} + a_F|^2 \right) , \quad \text{with } N = |a_{GT}^+|^2 + |a_{GT}^-|^2 + |a_{GT}|^2 + |a_F|^2 .$$

<sup>8</sup>The formulae for the correlation coefficients however, can be derived in a simple picture described in [Dub91][Döh90].

<sup>9</sup>The relative phase of the functions is arbitrary, as can be seen from the fact that the sign of the Fermi wavefunction is reversed when electron and neutrino are interchanged. Thus in this kind of calculation the sign of the interference term is not fixed.

And the mean values of  $j_z$  for the electron and similarly for the neutrino are then given by:

$$\begin{aligned} \langle m_e \rangle &= \frac{1}{N} (|a_{GT}^+|^2 - |a_{GT}^-|^2 + 2|a_{GT}a_F|\cos\Phi) \\ \langle m_\nu \rangle &= \frac{1}{N} \left( \underbrace{|a_{GT}^+|^2 - |a_{GT}^-|^2}_{\text{pure GT}} - \underbrace{2|a_{GT}a_F|\cos\Phi}_{\text{interference}} \right). \end{aligned}$$

The first two terms leading to an asymmetry are the ones responsible for the asymmetries in pure Gamow Teller transitions. They lead to the same asymmetries for electrons and neutrinos, except for a different energy dependence due to the helicity. The third terms are caused by the interference in a mixed transition, leading to contributions with different signs for the two leptons. Which one is increased and which one is decreased had to be determined from experiment. Thus the fact that the electron asymmetry is smaller than the neutrino asymmetry is due to the relative phase of  $\Phi \approx 180^\circ$  between the matrix elements in neutron decay. If the Gamow Teller and the Fermi amplitudes are of the same size the cancellation is exact<sup>10</sup> and  $A = 0$ , therefore  $A$  is very sensitive to the relative size of the amplitudes as has been discussed before (Fig. 2.4).

## 2.5 Radiative corrections

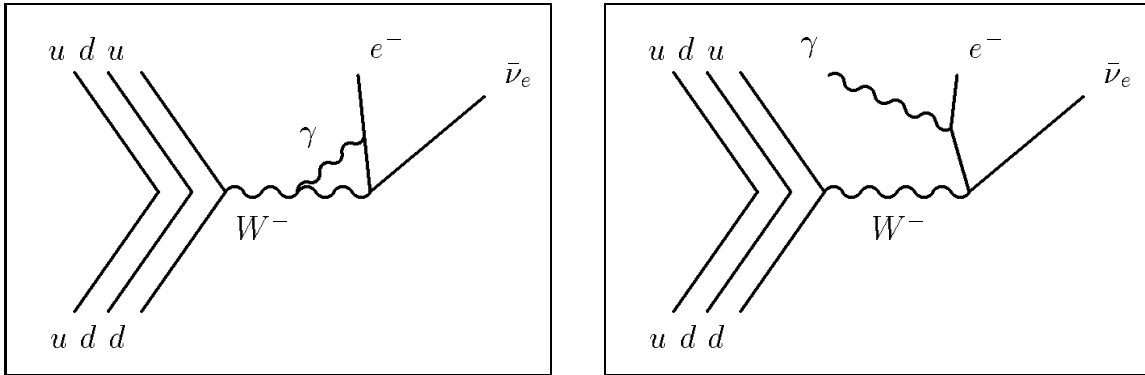


**Figure 2.5:** Feynman graphs of examples for contributions to the radiative corrections. The right one contributes to the external radiative corrections changing the electron spectrum since a real photon is emitted. This radiative neutron decay offers the possibility to actually measure one term of the radiative corrections.

Aside from the recoil corrections to the weak matrix elements in the case of hadronic decays, there are also additional theoretical corrections. These are the radiative corrections taking into account additional processes besides the basic W-boson exchange shown in Fig. 2.3. Possible processes are the additional exchange of virtual particles and the coupling to real particles as shown in Fig. 2.5. Following Sirlin [Sir67] these corrections can be separated into two parts: the outer radiative corrections which are independent of and the inner radiative corrections which depend on the details of the strong and weak interaction. The outer radiative (or

<sup>10</sup>This is a property of a  $(j_i = \frac{1}{2} \rightarrow j_f = \frac{1}{2})$  transition. The arguments given above can also be applied to nuclear decays. However, for  $J_i > 1/2$  the interference contribution dominates over the purely GT contribution to the asymmetry.

model independent) corrections lead to a change in the decay spectra but they can be explicitly calculated. In the case of neutron decay they lead to the function  $\delta_R(E)$  included in Eq.(2.22) and explicitly given in [Sir67]<sup>11</sup>.

The inner radiative (or model dependent) corrections only change the effective strength of the interaction but they are not themselves energy dependent. Thus they can be absorbed in effective coupling constants:

$$C_V'^2 = C_V^2(1 + \Delta_R^V) \quad (2.35)$$

$$C_A'^2 = C_A^2(1 + \Delta_R^A). \quad (2.36)$$

Therefore, in neutron decay we really measure the effective constants and particularly in our asymmetry measurement we determine  $\lambda' = C_A'/C_V'$ . The model dependent correction to the vector coupling constant is given by Towner and Hardy [Tow98] as:

$$\Delta_R^V = 2.40(8)\% \quad (2.37)$$

This will be important when  $V_{ud}$  is determined (Section 4.5.1) since in this case the bare coupling constants are needed. Otherwise this distinction between the effective and the bare coupling constants is not explicitly indicated in this thesis.

---

<sup>11</sup>There the calculation is done to first order in the fine structure constant  $\alpha$  which is the approximation we use. The Coulomb correction does belong in the same category since it is an additional virtual photon exchange between the electron and the proton but is corrected for by the separate Fermi function  $F_C(E)$  for historical reasons.



# Chapter 3

## Instrument

### 3.1 Measurement principle

We measure the asymmetry of the electron emission rate relative to the neutron spin direction. Therefore the basic idea is to put two detectors on either side of a polarized neutron beam and measure the relative intensity of decay electrons with the difference defining the asymmetry. The main feature of the PERKEOII spectrometer is the use of a strong magnetic field perpendicular to the neutron beam. The spins of the polarized neutrons align either parallel or antiparallel to the magnetic field depending on the state of the spin flipper. Electrons from neutron decay are forced to gyrate around the magnetic field lines. Thus the problem of measuring the distribution of electrons relative to the neutron spin is reduced to measuring the number of electrons guided parallel and antiparallel to the magnetic field. In this chapter the spectrometer PERKEOII is presented. First the general setup and the spectrometer itself are described. Then systematic effects and their consequences for the asymmetry measurement are analyzed. In particular, the detector response function is defined and its experimental determination explained.

#### 3.1.1 The setup of the experiment

To measure the electron asymmetry by the emission rates relative to the neutron spin direction, a polarized neutron beam is needed. The neutron beam for our experiment was provided by the European research reactor at the Institute Laue Langevin (ILL) in Grenoble. The experiment was set up at the PF1 experimental zone at the end of a guide (H53) for cold neutrons. The neutrons are moderated in liquid deuterium at 25 K leading to a maximum beam intensity at a wavelength of about 4 Å. A cold beam is a compromise of having slow neutrons to increase the probability of decay inside the apparatus and the need for high statistics. The neutron flux in our beam time was about  $1.7 \cdot 10^8 \text{ cm}^{-2} \text{ s}^{-1}$  (capture flux measured with gold foil activation) after the last baffle. The whole setup is shown, drawn to scale, in Fig 3.1. The first group of devices that were put in the beam are a wavelength cutter to remove neutrons with wavelength bigger than  $\sim 13$  Å, a polarizer to remove neutrons with one spin component and a spin flipper to allow to control the spin of the remaining polarized neutron beam. These devices will be described in more detail in Section 4.1.

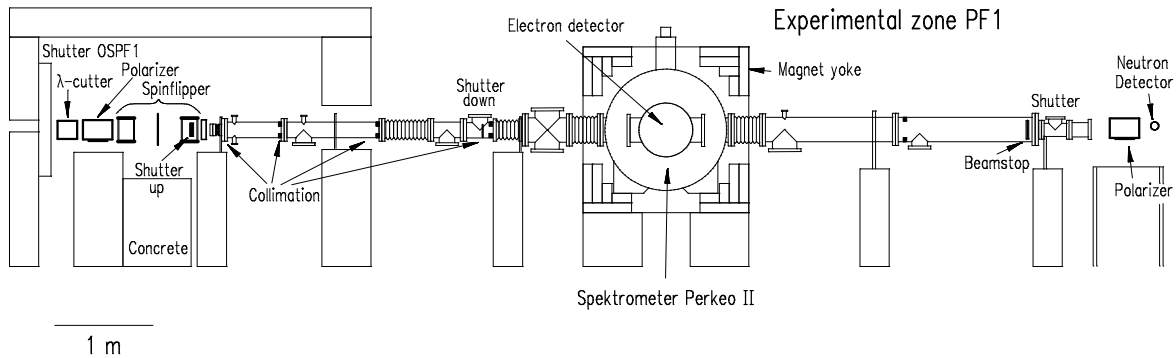


**Figure 3.1:** A schematic view of the whole setup at the ILL.

The following section of beam tube is used for the collimation system and for two beam shutters ('up' and 'down') used for background measurements. The collimation is achieved with 4 baffles limiting the beam size to  $35 \text{ by } 35 \text{ mm}^2$  with a divergence of about  $10 \text{ mrad}$ . This is a compromise between the goals of having a small divergence to reduce background and maximum transmission for high statistics. Thus the beam is well defined within a tube of  $25 \text{ cm}$  in diameter to avoid any risk of the neutron beam hitting the walls.

With regard to the previous beam time in 1995 several improvements have been introduced in order to reduce the background further. In the beam tubes before and after the spectrometer glass tubes have been installed around the beam. The boron content in the glass serves to absorb neutrons scattered from the baffles. The device to insert calibration sources inside the decay volume of the spectrometer was originally designed to let the neutron beam pass right through its center. In this beam time however, we placed it next to the neutron beam, thus providing a larger distance to the beam and avoiding any risk of neutrons hitting it. Also the beam stop had been redesigned for this beam time. In the new design the beam stop consists of two parts. The first part has the shape of a ring and is placed in front of the main beam stop. This has the advantage that the main beam stop could be placed further downstream from the spectrometer without having to use even larger diameter beam tubes. Also some of the neutrons that are reflected rather than absorbed by the main beam stop will then be absorbed in the ring. Another novel feature is a hole left in the main beam stop that could be controlled by a shutter. This allowed to monitor the beam polarization during the beam time using another polarizer and a neutron detector (Section 4.1.6).

### 3.1.2 The spectrometer

A schematic view of the spectrometer is shown in Fig. 3.2. The basic idea is that for a measurement of the correlation coefficient we need to measure the energy and the direction of the electrons emitted relative to the neutron spin. The most important advantage of the magnetic field in the spectrometer is that the electrons emitted from neutron decay are forced to gyrate around the field lines. Thus all electrons with a momentum component however small, either parallel or antiparallel to the magnetic field, are guided by the field lines to either one of two plastic scintillator detectors set up on both sides of the neutron beam. This way a solid angle of  $2 \times 2\pi$  is achieved.

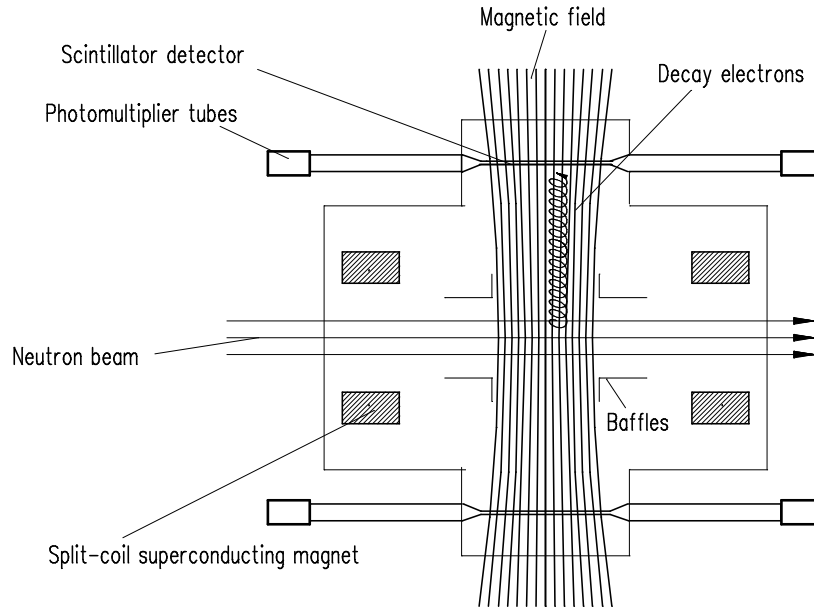


**Figure 3.2:** A schematic view of the spectrometer. Only the magnetic field lines crossing the decay volume are shown. The aluminum baffles defining the decay volume by stopping electrons emitted further up- or downstream are indicated. The path of an electron guided by the magnetic field is drawn with the gyration radius greatly exaggerated in relation to the size of the decay volume.

Another advantage of the magnetic field is that the spin of the polarized neutron beam will align exactly parallel or antiparallel to the field. Thus the magnetic field also divides up space into two hemispheres with respect to the neutron spin. Now instead of measuring the angle between the electron momentum and the neutron spin each detector measures a count rate integrated over one hemisphere. Thus the energy dependent count rate in the direction parallel to the neutron spin is (from Eq. (2.30)):

$$N^\uparrow(E) = F(E)' \int_0^{\pi/2} (1 + A\beta \cos \theta) \sin \theta d\theta = F(E)' \cdot \left(1 + A\beta \frac{1}{2}\right), \quad (3.1)$$

with the  $\cos \theta$  term integrated over one hemisphere being exactly 1/2. We then define the experimental asymmetry as:

$$A_{exp} = \frac{N^\uparrow - N^\downarrow}{N^\uparrow + N^\downarrow} = \frac{1}{2} A\beta. \quad (3.2)$$

In electron spectroscopy backscattering is always a problem. A fraction of the incident electrons will deposit only part of their energy inside the detector and then leave it again. This can lead to a systematic error in the determination of the electron energy. Furthermore, this effect has an unknown angular dependence. Here again the magnetic field is of great advantage. Electrons backscattered by one detector will either be guided by the magnetic field to the opposite detector or be reflected back to the same detector by the magnetic mirror effect (Section 3.2.1). Thus the magnetic field guarantees that for each event we determine the correct total energy since we always add the energy deposited in both detectors.

The magnetic field is produced by two superconducting coils with a radius of 475 mm at a distance of 364 mm. Thus the coils are somewhat closer than at the Helmholtz configuration to assure that the field is decreasing towards the detectors. The length of the decay volume is defined by adjustable aluminum baffles. All electrons with a center of motion closer to the baffles than their gyration radius have to hit the baffles. The cut is not ideal since it leads to the length of the decay volume effectively depending on the phase space of the electrons. This effect will be considered in more detail in Section 3.4. The maximum gyration radius at a field of 1 T is about 4 mm and the maximum pitch is 24 mm.

A capture flux<sup>1</sup> of  $\Phi_C = 1.7 \cdot 10^8 \text{cm}^{-2} \text{s}^{-1}$ , defined at a thermal velocity of  $v_{\text{therm}} = 2200 \frac{\text{m}}{\text{s}}$ , was measured at the position of the last baffle where the beam cross section was  $a = 37 \times 33 \text{mm}^2$ . With the length of the decay volume  $L = 25.5 \text{cm}$  and the neutron lifetime of  $\tau = 886 \text{s}$  the number of neutron decays inside the spectrometer can be calculated:

$$n = \frac{\Phi_C \cdot aL}{v_{\text{therm}}\tau} \approx 290 \text{ Hz.} \quad (3.3)$$

The detector itself has to meet the following requirements:

- Large size to obtain high statistics.
- High efficiency for electron detection and low efficiency for gammas.
- Fast timing to determine which detector was hit first when a backscatter event caused a trigger in both detectors.
- Low energy threshold, small dead layer.

All these requirements are best met by plastic scintillators. In this beam time we used ZA236 manufactured by Zinsser of dimensions  $400 \times 160 \times 5 \text{mm}^3$ . Each scintillator is read out by two photomultiplier tubes (R1332 by Hamamatsu) operated in coincidence to avoid dark counts. Since these tubes cannot be operated inside the magnetic field the light was guided out of the magnet yoke. With a fishtail arrangement the rectangular cross section of the scintillator side was adiabatically converted to a cylindrical light guide of 5 cm diameter. A gap of about 1 mm was left between the light guides and the vacuum windows in order to avoid any stress on the scintillator due to evacuation and thermal expansion of the apparatus. The PMT's were then coupled with optical grease to the vacuum windows and they were still covered by several layers of  $\mu$ -metal and iron against the remaining magnetic field.

### 3.1.3 Shielding

Shielding is of special concern to all neutron decay experiments. Due to the long lifetime of the neutron the signal to background ratio is usually rather poor. Most experiments use

---

<sup>1</sup>The capture flux was measured using gold foil activation. Due to the  $1/v$  law for the capture cross section the activation produced is a measure of the spatial neutron density rather than of the neutron flux [Byr94]. The capture flux is then defined as the beam flux assuming all neutrons had thermal velocity, which for most cases is a measure of the relevant quantity, the intensity weighted with  $1/v$ . The true neutron flux of the beam is obtained by an integration over the velocity spectrum,  $n(v)$ , of the beam:  $\Phi = \frac{\Phi_C}{v_{\text{therm}}} \int n(v)v dv$ .

coincidence techniques to suppress  $\gamma$  background. The PERKEO experiment chose a different approach by using the magnetic field to increase the rate of true events while not enhancing the background, thus improving the signal to background ratio. In this way at the same time the count rate is increased making PERKEO the experiment with the highest rate of neutron decay events observed. The price one has to pay is that gamma background events can not be distinguished from true electron events. Thus avoiding the production of any background is especially crucial for us. This is achieved mainly by designing the whole setup big enough for the neutrons to pass without hitting any material.

The points where the neutron beam had to be intercepted (i.e. the baffles and the beam stop) were placed far from the spectrometer (see Fig. 3.1). The only material used to tailor the beam was  ${}^6\text{LiF}$  since it combines a high absorption cross section of 940 barn with a minimum of secondary radiation emitted. The alpha particles emitted are immediately stopped in the surrounding material and can not reach the detectors. Fast neutrons and  $\gamma$  quanta are emitted with a probability of only about  $10^{-4}$ . To absorb the fast neutrons a combination of polyethylene and boron carbide is used. The polyethylene serves to thermalize the neutrons and the boron has a high absorption cross section for thermal and epithermal neutrons of 760 barn. Several tons of lead bricks were installed to absorb the  $\gamma$  radiation that had to undergo multiple scattering in order to reach the detector. The details of the arrangements are described in [Pes98].

## 3.2 Effects of the magnetic field gradient

### 3.2.1 Magnetic mirror effect

In the PERKEO spectrometer we take advantage of the fact that charged particles gyrate around magnetic field lines. However, in an inhomogenous magnetic field the motion of the particles is more complicated. When the magnetic field changes slowly, the magnetic moment produced by the gyrating motion of a charged particle is an adiabatic invariant. This leads to the ratio  $p_{\perp}^2/B$  being conserved. Thus if the center of motion is moving into a region with increasing field strength the transverse component of the momentum will increase and the longitudinal component will decrease accordingly. Electrons emitted from neutron decay inside the spectrometer will actually reverse their direction of motion if the angle of emission with respect to the magnetic field is larger than a critical angle

$$\theta_{\text{crit}} = \arcsin \sqrt{\frac{B_{\text{decay}}}{B_{\text{max}}}}, \quad (3.4)$$

where  $B_{\text{decay}}$  is the magnetic field at the point of the neutron decay and  $B_{\text{max}}$  is the maximum field encountered respectively. In order to avoid the possibility of trapping electrons by this mirror effect, the magnetic field in the spectrometer was designed in such a way that it has a maximum in the center and falls off towards the detectors (i.e. the field coils are somewhat closer together than in the Helmholtz configuration). However, since the neutron beam has a width of about 8 cm inside the decay volume there is still the possibility of electrons being reflected by the magnetic field if they are emitted from the side of the neutron beam towards the center. These electrons are then detected in the wrong detector washing

out the asymmetry. An analytical calculation of the effect [Rav95] shows that the correlation coefficient averaged over both detectors is systematically too small:

$$\bar{A} = \frac{A \cdot M}{1 - k^2}. \quad (3.5)$$

The parameter  $M = 0.9991(1)$  describes the curvature of the magnetic field and its uncertainty is given by the systematic accuracy of the calculation. This calculation was performed for a decay volume with a length of 29 cm as opposed to 25.5 cm which was used in this beam time. While this is not expected to change the result significantly we double the uncertainty given. The parameter  $k$  depends on the misalignment of the maximum of the magnetic field with respect to the center of the neutron beam.

In this experiment the magnetic field and the neutron beam were aligned to within less than 2 mm leading to  $k < 3 \cdot 10^{-3}$ . The difference of the correlation coefficient values in both detectors depends linearly on  $k$  accounting for a possible difference of up to  $\Delta A/A \leq 0.6\%$ . But in the correction to the average result, Eq.(3.5),  $k$  enters only quadratically and therefore can be neglected. In the final analysis  $\bar{A}$  has to be increased by 0.09(2)% to correct for  $M$ . The effect is that small due to the good homogeneity of the magnetic field and due to the fact that for electrons emitted at close to  $90^\circ$  with respect to the magnetic field the asymmetry reaches a minimum.

### 3.2.2 Stern Gerlach effects

By longitudinal Stern Gerlach effect we refer to the effect that neutrons with spins parallel to the magnetic field are slowed down when entering the field of PERKEOII whereas neutrons with spin antiparallel are accelerated. Thus the two spin states pass through the spectrometer with different velocities leading to an increased effective decay length for neutrons with spin parallel to the magnetic field. However, since we leave the magnetic field unchanged and flip the spin with respect to the magnetic field this effect has opposite signs for the two detectors:

$$\begin{aligned} A_{1,exp} = \frac{N^\uparrow - N^\downarrow}{N^\uparrow + N^\downarrow} \rightarrow A'_{1,exp} &= \frac{N^\uparrow - N^\downarrow + (N^\uparrow + N^\downarrow) \frac{\Delta v}{v}}{N^\uparrow + N^\downarrow + (N^\uparrow - N^\downarrow) \frac{\Delta v}{v}} \\ &\approx A_{1,exp} + \frac{\Delta v}{v} \\ A_{2,exp} \rightarrow A_{2,exp} - \frac{\Delta v}{v} \end{aligned} \quad (3.6)$$

The effect on the angular correlation coefficient  $A$  for a single detector can be calculated:

$$\frac{\Delta A}{A} = \frac{\Delta v}{v} \frac{2}{A\beta} \approx 25 \cdot \frac{\Delta v}{v}. \quad (3.7)$$

Averaged over the neutron wavelength spectrum the relative change of  $\Delta A/A$  is only about 0.03%. Thus a difference in the measured correlation coefficients of 0.06% between the two detectors can be attributed to this effect. In the averaged final result, however, the linear term cancels and the longitudinal Stern Gerlach effect only enters in the next higher order which is completely negligible.

In addition to the longitudinal Stern Gerlach effect there is also a transversal Stern Gerlach effect. Since the magnetic field has a maximum at the center of the neutron beam and falls off towards the detectors, one spin state is focused while the other spin state is defocused when entering the spectrometer. Thus the beam cross section will vary slightly leading to a spin dependent magnetic mirror effect. To first order this effect cancels as well when taking the average of the two detectors. In any case, a conservative estimate [Rav95] shows that already the first order term is negligible.

### 3.3 Detector response function

The detector response function gives for each ADC channel the probability that an event will be recorded in this channel depending on the amount of energy deposited. The detector function for PERKEO is not just an empirical function but rather follows closely the different physical processes inside the detector. While leading to a large number of parameters that have to be determined, this approach has the advantage of yielding more reliable results for physical interesting parameters, e.g. the number of photoelectrons produced. In this section the detector function is motivated and defined and in the following sections the determination of the needed parameters is presented.

An electron entering the plastic scintillator loses its energy to the scintillating material, producing a number of primary photons that is proportional to the deposited energy. These photons have to be guided to the photo multipliers operated outside the magnetic field. With a quantum efficiency of about 20 %, averaged over the photon wavelength spectrum, these photons are then converted into electrons in the photocathode of the PMT's. Subsequently the number of electrons is amplified by a factor of typically  $10^6$  giving the charge signal fed into the ADC's. In these processes the smallest number of particles is reached with the number of photoelectrons produced. Therefore the statistical uncertainty of this process gives the most important contribution to the width of the signal. In the detector function the number of photoelectrons  $N$  is assumed to follow a Poisson distribution:

$$P(N, \bar{N}) = \frac{\bar{N}^N e^{-\bar{N}}}{N!}, \quad (3.8)$$

with the average  $\bar{N} = p_{\text{MeV}} \cdot E$  proportional to the energy  $E$  deposited and  $p_{\text{MeV}}$  the number of photoelectrons produced per MeV deposited energy.

Thus the width of the signal is primarily determined by the statistical fluctuations of photoelectrons produced leading to :

$$\frac{\Delta \bar{N}}{\bar{N}} = \frac{1}{\sqrt{\bar{N}}} = \frac{1}{\sqrt{p_{\text{MeV}} \cdot E}}. \quad (3.9)$$

In the ADC the charge from the PMT is converted into a channel number  $C$ . If all processes involved are linear the channel number is proportional to the number of photoelectrons

$$C = g_{\text{PE}} N(E) + C_{\text{ped}}, \quad (3.10)$$

with the gain  $g_{\text{PE}}$  in units of channels per photoelectron and an adjustable offset, the pedestal  $C_{\text{ped}}$ . Due to statistical fluctuations introduced by the multiplication process in the PMT and by the electronics, this function is assumed to be broadened to a Gaussian distribution according to :

$$\phi(C, N) = \frac{1}{\sqrt{2\pi}\sigma(N)} e^{-\frac{(C - g_{\text{PE}}N(E) - C_{\text{ped}})^2}{2\sigma(N)^2}}. \quad (3.11)$$

The width of the distribution is given by:

$$\sigma(N) = \sqrt{\sigma_{\text{el}}^2 + \sigma_{\text{dyn}}^2}, \quad (3.12)$$

with  $\sigma_{\text{el}}$  and  $\sigma_{\text{dyn}}$  the contributions of the electronic width and the statistics of the first dynode respectively<sup>2</sup>. The total detector function  $f(C, E)$  is then given by a sum over the distribution of photoelectrons:

$$f(C, E) = T(C) \cdot \sum_N P(N, \overline{N(E)}) \cdot \frac{1}{\sqrt{2\pi}\sigma(N)} e^{-\frac{(C - g_{\text{PE}}N(E) - C_{\text{ped}})^2}{2\sigma(N)^2}} \quad (3.13)$$

In addition, the trigger function  $T(C)$ , giving the probability that the discriminator will recognize an event depositing the energy  $E$  corresponding to the channel  $C$ , was introduced. In order to analyse our data we first have to completely determine the detector function. Thus the main objective of the following sections is to show how the function  $T(C)$  and the parameters  $C_{\text{ped}}$ ,  $\sigma_{\text{el}}$ ,  $g_{\text{PE}}$ ,  $p_{\text{MeV}}$  have been measured.

### 3.3.1 Pedestal and threshold

During the beam time the pedestals were checked daily. For all four PMT's they were set to channel 5 leading to a pedestal of  $C_{\text{ped}}=20$  for the detector since the signal of all photomultipliers is added. A typical example is shown in Fig. 3.3. The pedestal spectra are obtained by using the data from one PMT whenever an event was recorded in the opposite detector only. From the width of the pedestal spectra  $\sigma_{\text{el}} = 1.2$  is determined.

The trigger function is determined using neutron decay data since there the electron spectrum extends to the lowest energies. In order to obtain the trigger function of detector 1, all the events are analysed when detector 2 registered an event:  $N_{D2}$ . Due to backscattering (Section 3.4) there remains the possibility that some energy was deposited in detector 1 as well. This energy can cause a second trigger to be generated from detector 1 in coincidence with detector 2. The number of events when both detectors registered one event in coincidence is  $N_{D1\&D2}$ . The fraction of events in each channel of detector 1 where both detectors triggered to cases where only the second detector triggered gives the trigger function  $T_1$  of detector 1:

$$T_1(C) = \frac{N(C)_{D1\&D2}}{N(C)_{D2}}. \quad (3.14)$$

<sup>2</sup>With a multiplication factor of  $\delta_1$  for the secondary electron emission at the first dynode  $\sigma_{\text{dyn}}$  can be calculated :  $\sigma_{\text{dyn}}^2 = \frac{C^2}{\delta_1 N} = g_{\text{PE}}^2 \frac{N}{\delta_1}$ . We use  $\delta_1 = 20$  as specified by the supplier.

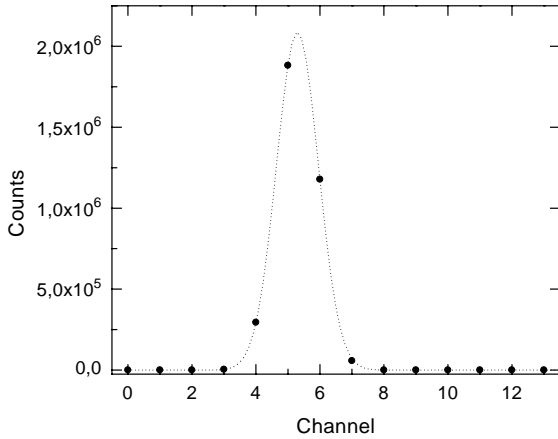


**Figure 3.3:** Pedestal spectrum of one PMT with a Gaussian fit from which  $\sigma_{el} = 1.2$  is determined.

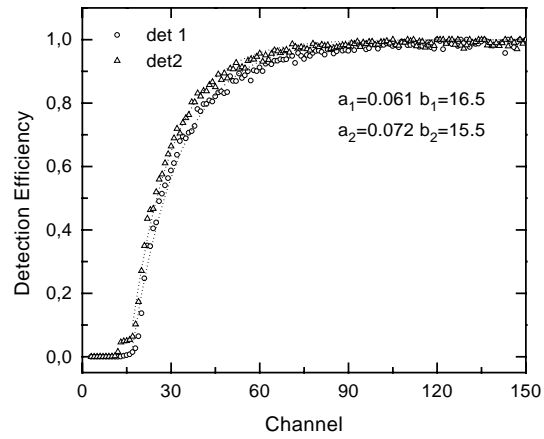


**Figure 3.4:** The measured trigger efficiencies of the two detectors together with the corresponding fits of the theoretical trigger functions.

The trigger functions for the two detectors are shown in Fig. 3.4. Also shown are the two parameter fit functions that are then used in the detector function:

$$T(C) = 1 - e^{-a(C-b)}, \quad (3.15)$$

where  $C$  is the channel number and  $a, b$  are the two fit parameters that are determined for both detectors. Strictly, the trigger functions are thus determined only for single detector events. However, a correction for backscattered events would be small since they make up only about 3.3% of all events.

### 3.3.2 Detector calibration

The remaining parameters that need to be determined in the detector function are the gain,  $g_{PE}$  and the resolution,  $p_{MeV}$ , that is the detector has to be calibrated. So far the detector was assumed to behave linearly, Eq.(3.10). To check this assumption experimentally we had the possibility of inserting different calibration sources. The sources are conversion electron sources where excited nuclei transfer their energy to electrons rather than to  $\gamma$  rays with a certain probability. The electron energy is then just the difference of the excitation energy and the binding energy of the shell from which it was emitted. However, after the emission of the conversion electron there remains a hole in the atomic shell. Besides X-rays there is then also the possibility of subsequent emission of Auger electrons. The electrons are thus not really monoenergetic and the energies  $E_e$  given in the list below are averages over the different processes involved. The sources are discussed in detail in [Sch92] and [Met95], except for  $^{137}\text{Cs}$  which was used for the first time. The following sources were used to cover the range of the beta spectrum:

- $^{109}\text{Cd}$ ,  $E_e = 87 \text{ keV}$
- $^{139}\text{Ce}$ ,  $E_e = 136.6 \text{ keV}$

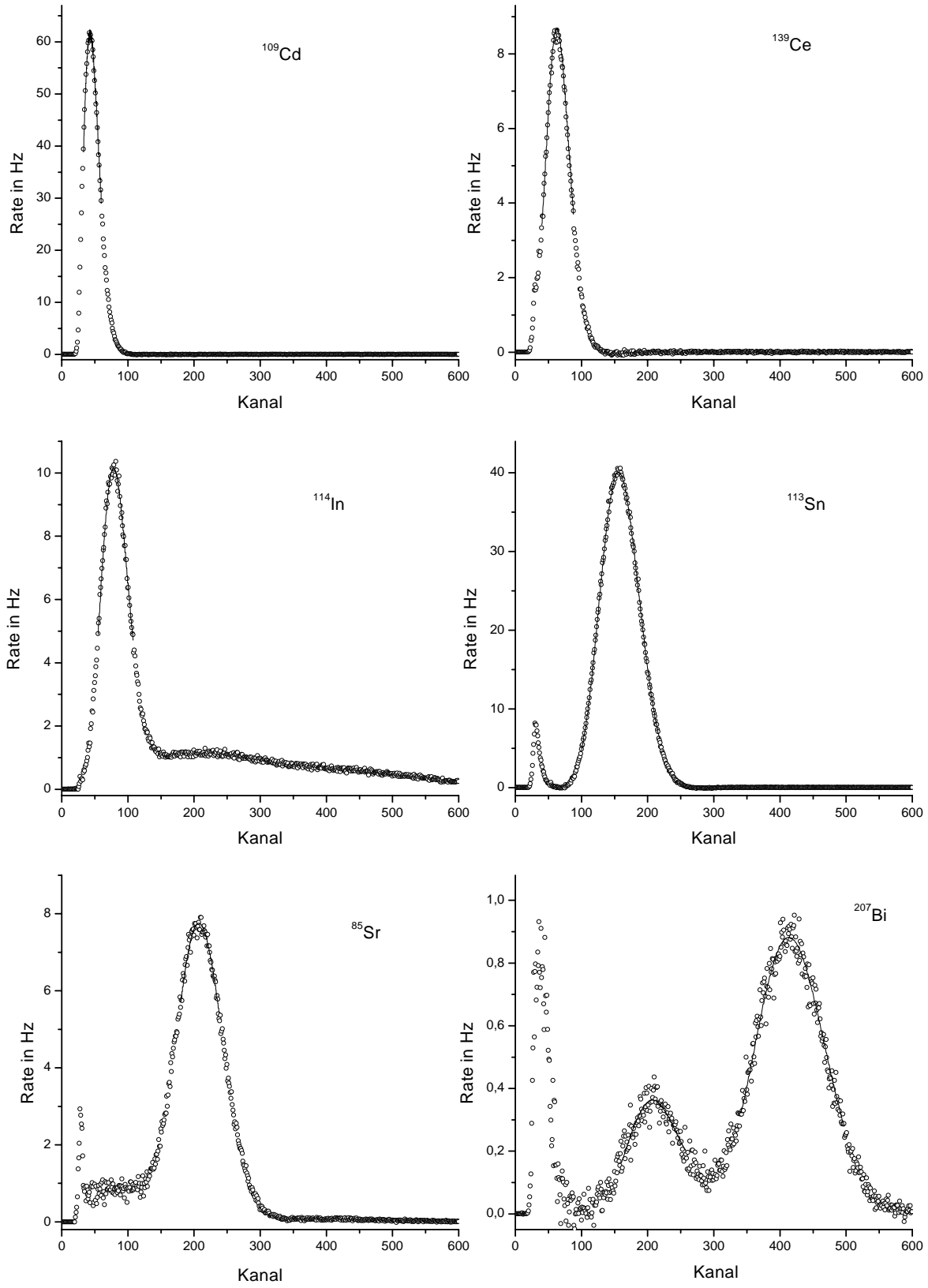


Figure 3.5: Spectra and fits to the calibration sources used in the analysis.

- $^{114}\text{In}^m$ ,  $E_e = 176.9$  keV
- $^{113}\text{Sn}$ ,  $E_e = 371.9$  keV
- $^{85}\text{Sr}$ ,  $E_e = 503.7$  keV
- $^{137}\text{Cs}$ ,  $E_e = 629.3$  keV
- $^{207}\text{Bi}$ ,  $E_e = 504.5$  keV and  $E_e = 996.9$  keV

In order to fit the spectra of the calibration sources a double difference of spectra is taken [Mül96]. The signal in the detector can be divided into contributions from electrons and  $\gamma$  rays from the source ( $e_S, \gamma_S$ ) and electrons and  $\gamma$  rays from background ( $e_B, \gamma_B$ ). To single out the contribution of electrons from the source only, we make use of the magnetic field. Spectra with and without the sources inserted are measured while the magnetic field is on  $S_{S,B}, S_{0,B}$  and off  $S_{S,0}, S_{0,0}$ . The double difference

$$\begin{aligned}
 S_{S,B} - S_{0,B} - (S_{S,0} - S_{0,0}) &\approx e_S + \gamma_S + e_B + \gamma_B \\
 &\quad - e_B - \gamma_B \\
 &\quad - 5\%e_S - \gamma_S - x\%e_B - \gamma_B \\
 &\quad + x\%e_B + \gamma_B \\
 &\approx 95\%e_S
 \end{aligned}$$

is then free of background. Due to the solid angle extended by the detectors about 5% of all electrons reach the detectors without the magnetic field. This leads to the factor of 95%. The fits to the different sources are shown in Fig. 3.5.

In the fit functions usually two monoenergetic electrons are used, corresponding to conversion electron emission from K and L shell. Their energies are corrected for the summing of Auger electrons. From the peak positions determined in the fits the detectors can be calibrated as shown in Fig. 3.6 and 3.7. The low energy Bi peak and the Sr peak were averaged into one data point, since the systematic uncertainty in the energy calibration was larger than their energy difference. In the same way, two calibration sources of the same isotope gave systematically slightly different values, in which case they were averaged (Sn and Bi). The systematic effects may be due to the spatial dependence of the gain and different source positions on the calibration device not being equivalent.

With the assumption of a linear detector response the data can be described very well. The gain in the fit routine is not parametrized as  $g_{\text{PE}}$  in units of channels per photo electron but rather as  $g_{\text{MeV}}$  in units of channels per MeV energy. Apart from an overall normalization constant  $p_{\text{MeV}}$  and  $g_{\text{MeV}}$  are the only free parameters in the fits to the calibration sources. They are also the two most important parameters of the detector function, determining the gain and the resolution. The results for the two detectors are shown in Table 3.1. With an average quantum efficiency of the photocathode of about 20%, the number of 75 photoelectrons per MeV translates into 375 scintillation photons reaching the photomultipliers per MeV energy deposited. With typically 10000 photons/MeV produced in the scintillator [Cla74], only about 4% of the light reaches the PMT's. The single largest loss factor is the fraction of photons that is not guided in the scintillator by total internal reflection but is lost immediately. Other significant loss mechanisms are the short attenuation length in the scintillator

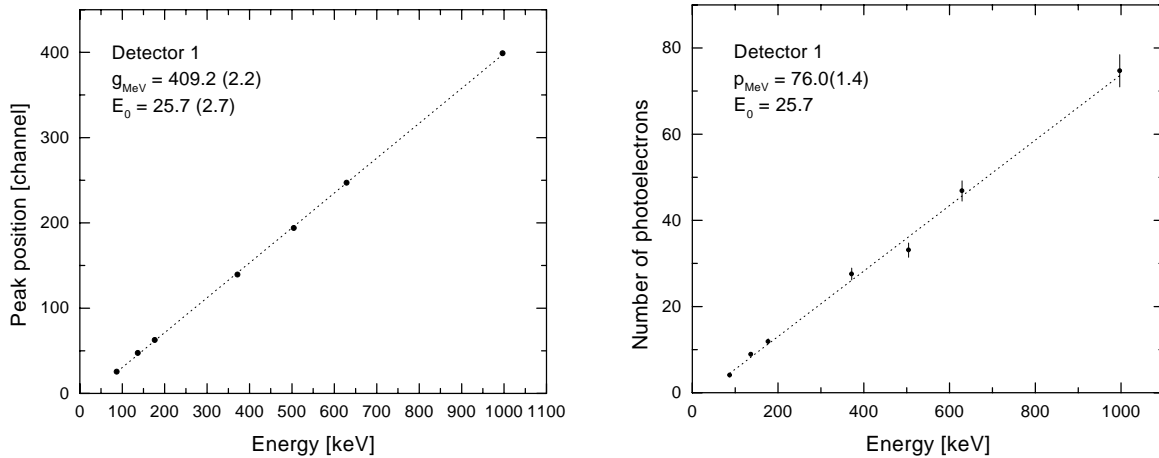


**Figure 3.6:** Calibration of detector 1.

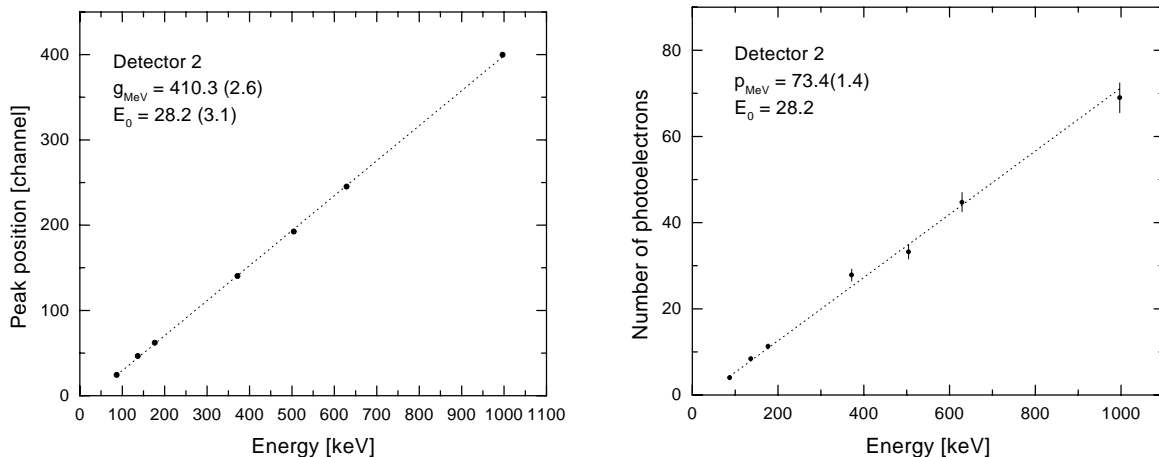


**Figure 3.7:** Calibration of detector 2.

due to its thinness (Figure 3.13), and losses in the light guide and couplings. For the proton detection it is crucial to improve the light collection efficiency and currently work is carried out to study the different possibilities [Plo00].

The average quadratic differences of  $g_{\text{MeV}}$  and  $p_{\text{MeV}}$  as obtained from the fits to individual sources and the linear fit shown in Figures 3.6 and 3.7 gives a measure for a possible detector nonlinearity. The results are given as  $\Delta_g$  and  $\Delta_p$  for the sources Sn, Sr and Bi<sub>low</sub>, and Cs since their energies fall in the region used in the data analysis.

	$g_{\text{MeV}}$	$p_{\text{MeV}}$	$\Delta_g$	$\Delta_p$
Detector 1	409.2(2.2)	76.0(1.4)	1.1%	6.3%
Detector 2	410.3(2.6)	73.4(1.4)	1.0%	10.0%

**Table 3.1:** Calibration of the detectors.

The Cs source was used for the first time in this analysis. It was measured only after the beam time was over but within the experimental accuracy the linearity of the detector remained stable. The fit is shown in Fig. 3.8. For the line an average energy of  $E_e = 629.3$  keV was used. In the fitting routine this was refined to one line with  $E_K = 624.26$  keV and an intensity of 7.66 %, corresponding to electron emission from the K shell, and a second line with  $E_{LMN} = 655.8$  keV and an intensity of 1.46 %, corresponding to an average over the outer shells. These data were derived from [Led78][Lar77][NDS94]. However, the conversion electron line leads only to a small peak on top of two continuous  $\beta$  spectra. The  $\beta$  spectra are distorted since they are first and second order forbidden transitions and could not be perfectly reproduced in the fit (an analytical expression given in [Wu66] was used). However, the influence of the shape of the beta spectra on the determination of the peak position was smaller than the statistical uncertainty of about 0.5 %.

The extension of the calibration curve to zero energy deposited does not lead to the channel number for the Pedestal as it should be. Instead with a linear extrapolation one has to assume that some energy  $E_0$ , 25.7 and 28.2 keV for the two detectors respectively, is lost. This can be explained by either a dead layer on the scintillator or a nonlinear detector function at low energies, below about 70 keV. The only consequence is that we may introduce an error when calculating the effective electron energy of the calibration sources since there we add the signal from low energy Auger electrons to the conversion electron signal. The error thus introduced in the gain has been estimated to be about 1% [Bae96].

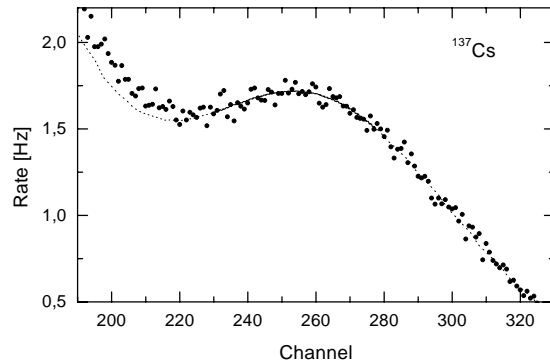


**Figure 3.8:** Fit to the line in the Cs spectrum.

However, this calibration of the detector, while showing well the linear detector response, is not sufficient since with the calibration sources only a small area close to the center of the detector panels is used. In the neutron decay measurements an average over the decay volume is performed. Thus the spatial dependence of the gain has to be taken into account. This can be achieved by two different methods. The more direct approach is to try to measure the spatial dependence over the decay volume and to correct the gain accordingly. The other approach is to use the calibration sources only as proof of the linearity of the detector response and fix the gain by fits to the background free difference of neutron decay spectra measured with the two different spin states.

### Gain determined from the difference of spectra with two spin states

In this section the gain of the detector function is determined from the difference of neutron decay spectra for the two spin states. Since the background does not depend on the spin state and a time dependence is averaged out by changing the spin every 30 seconds, this difference is free of background:

$$\left(N^\uparrow - N^\downarrow\right) \propto \beta F(E)' \quad (3.16)$$

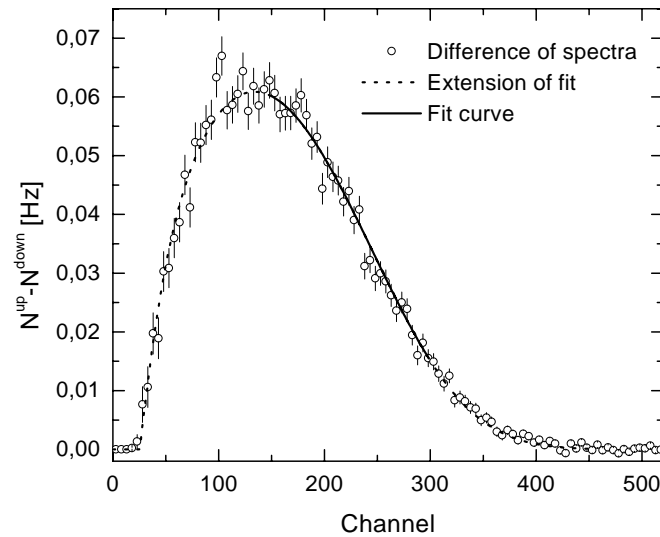


**Figure 3.9:** Difference of spectra for the two spin states in one detector with the corresponding fit and its extension.

where  $\beta$  is the electron velocity in units of the speed of light and  $F(E)'$  is the energy spectrum of neutron beta decay defined in Eq. (2.22). A fit to such a spectrum is shown in Fig. 3.9. The only free parameters are the gain and a normalization constant. The fit is performed only in the energy region later used in the data analysis but also the extensions of the fit describe the data well. The fixed parameters involve the ones used in the detector function like the widths and threshold parameters, that have been measured, but also physical parameters used in the Fermi function like weak magnetism, proton recoil, and radiative corrections, that have to be calculated. To check the reliability of this method the dependence of the gain obtained in the fit on the values of the fixed parameters was studied.

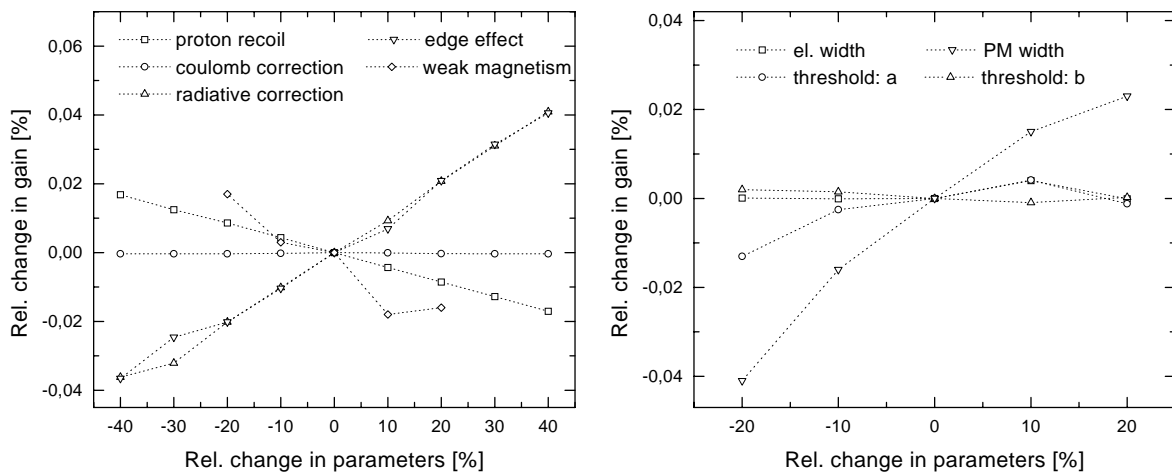


**Figure 3.10:** Dependence of the fit result for the gain on changes in fixed fit parameters. The dotted lines are shown to guide the eye. The deviations from smooth dependencies are statistical artefacts.

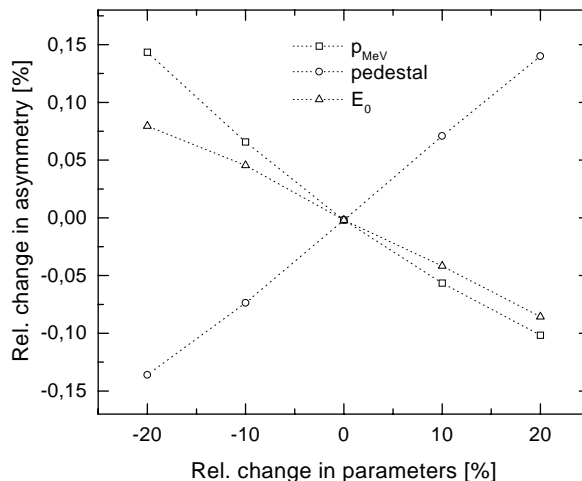


**Figure 3.11:** Dependence of the correlation coefficient on changes in fit parameters.

In the left part of Fig. 3.10 the dependence of the gain on the calculated parameters is shown. The theoretical corrections to neutron decay are all known with an uncertainty of several per cent. On this scale their influence on the gain is completely negligible. For the edge effect (Section 3.3.4) an estimated uncertainty of 40% changes the fit result for the gain by less than 0.05%, which is still negligible compared to the 1% uncertainty from the calibration. In the right part of Fig. 3.10 the dependence of the gain on the measured parameters in the detector function is shown. These parameters are known to an uncertainty of less than 20%, thus their influence on the determination of the gain is negligible as well. Thus this method of determining the gain is sufficiently insensitive to the fixed parameters.

However, the gain changes by about 1% on changes of 20% in  $p_{\text{MeV}}$ ,  $E_0$ , and the pedestal. Yet, this is not a specific problem of this approach to determine the gain since the same parameters enter in the fit of the asymmetry. In any case the dependence of  $A$  on errors in these parameters has to be examined. The measured uncertainties of about 10% in these quantities lead to an uncertainty of about 0.1% in  $A$  as can be seen from Fig. 3.11. The values of the gain determined from the fits to the difference are summarized in the center column of Table 3.2.

### Gain determined from the average over its spatial dependence

To measure the spatial dependence of the detector gain, we used a Sn source mounted on a swing [Ast97]. With this device we were able to scan the decay volume along the neutron beam and also in the vertical direction. In Fig. 3.12 the number of photoelectrons per MeV,  $p_{\text{MeV}}$ , is shown for the individual PMT's depending on the position of the source along the neutron beam. The dependence can be described as an exponential decay with an attenuation length<sup>3</sup> of about 14 cm for the PMT's of detector 1. For detector 2 there is an asymmetry showing that the coupling to PMT 2a was worse than that to the other PMT's. Some fraction

<sup>3</sup>These attenuation lengths are measured as a function of the source position in the decay volume. Since the magnetic field at the detectors is only about half as strong as in the decay volume the true attenuation lengths of the scintillator are larger by a factor of  $\sim 1.4$ .

	Fit to difference	Spatial average
$g_{\text{MeV}}$ of detector 1	452(2)	456(9)
$g_{\text{MeV}}$ of detector 2	431(2)	431(2)

**Table 3.2:** Values for the gains of the detectors obtained from fits to the difference of neutron decay spectra with the two spin flipper states and from mapping the spatial dependence directly. While the values agree, the strong spatial dependence of the gain in detector 1 leads to a large uncertainty in the spatial average.

of the light even seems to be reflected back to PMT 2b leading to longer attenuation lengths for these two PMT's of about 20 and 16 cm. Comparing these curves to the ones obtained in the last beam time [Mül96] shows that the scintillator used in this beam time (ZA236 by Zinsser) had a significantly shorter attenuation length than the one (BC404 by Bicron) used in the last measurement. In fact, contrary to our first suspicions, the decrease in the number of photoelectrons (from  $p_{\text{MeV}} \approx 90$  to  $p_{\text{MeV}} \approx 75$ ) obtained can be explained by this effect mostly, whereas changes in the light guide system had no measurable effect.

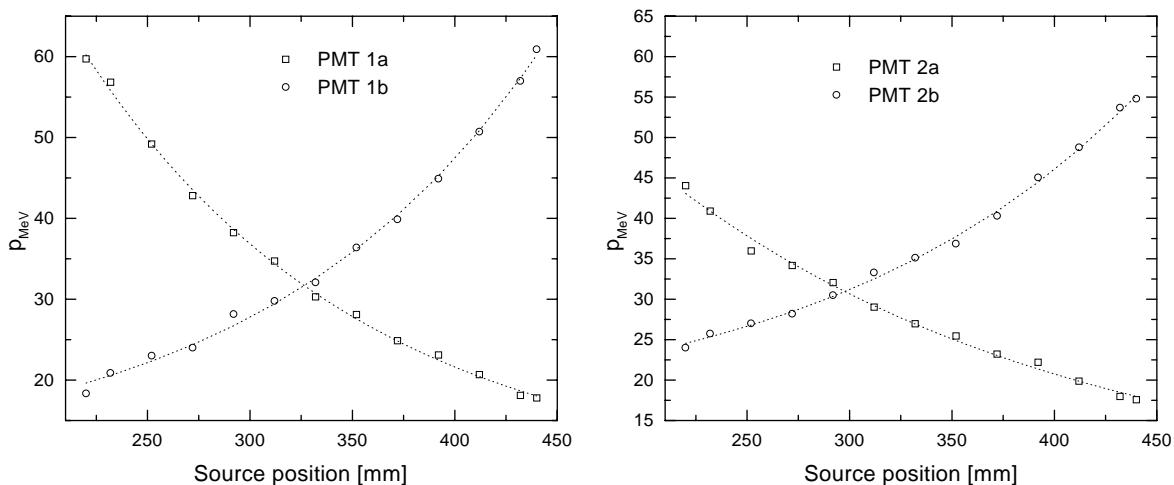


**Figure 3.12:** Dependence of the number of photoelectrons ( $p_{\text{MeV}}$ ) on the position of the calibration source along the neutron beam axis for the four PMT's.

This strong spatial dependence does not only decrease the overall light collection efficiency but it also makes the calibration of the detector rather difficult. The correction due to the averaging over the neutron beam as seen by the scintillator is large, the gain of  $g_{\text{MeV}} \approx 410$  obtained from the detector calibration is increased by about 10 % in the case of detector 1. In Fig. 3.13 the dependence of the gain  $g_{\text{MeV}}$  on the source position along the beam axis is shown for the detectors at three different heights. The difficulty is to correctly map the neutron beam. In direction of the neutron beam, this is facilitated by the baffles limiting the decay volume. In the vertical direction however, the scintillators are made larger than the height of the neutron beam to avoid an edge effect. Thus there is no easy geometric limitation. The center of the neutron beam was determined to be between the central and the upper curves in Fig. 3.13. Therefore, the correction for the spatial dependence was done by averaging all three and only the upper two curves. In the right column of Table 3.2 the average of both results is shown with the deviation as an estimate for the uncertainty.

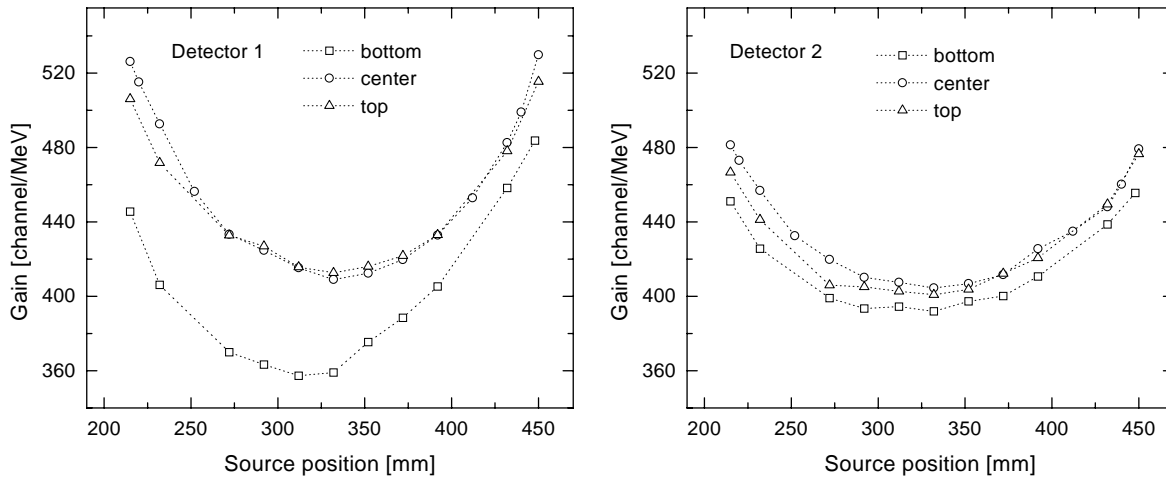


**Figure 3.13:** Dependence of the gain on the position of the source.

The results confirm independently the values obtained from the fit to the difference of neutron decay spectra. However, in detector 1 the spatial dependence leads to a large uncertainty. In the analysis the results from the fits to the difference spectra were used since there the averaging over the neutron beam is done exactly.

In summary the consequences for the determination of the asymmetry are the following: from the uncertainty in the detector linearity (see Table 3.1) the uncertainty of the gain is 1 % and the uncertainty of  $p_{\text{MeV}}$  is 10 %. The uncertainty in the gain leads to an uncertainty of the correlation coefficient of 0.2 % as can be seen in Fig. 3.14. The uncertainties in  $p_{\text{MeV}}$ ,  $E_0$ , and the pedestal result in an error of about 0.1% in  $A$  (Fig. 3.11). These uncertainties have to be compared to the total effect of the detector function on the determination of  $A$ . In the energy range used in the data analysis  $A$  is changed only by about 1 % [Bae96].

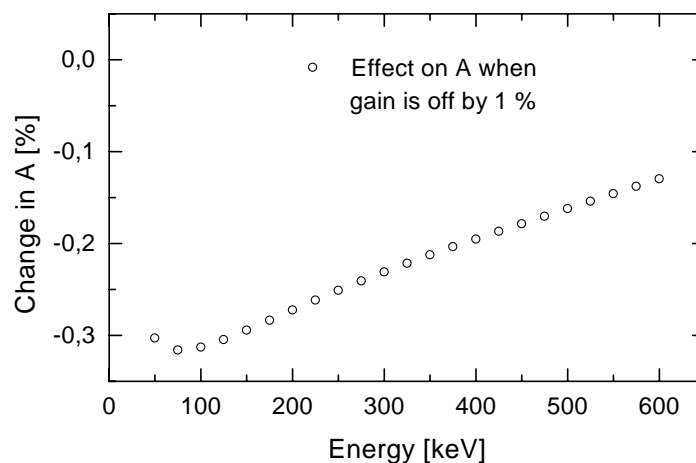


**Figure 3.14:** Change of  $A$  due to an error of 1% in the gain.

### 3.3.3 Detector drifts and rebinning

During the measurement period the temperature of the PMT's and the related electronics had to be controlled in order to stabilize the gain. At regular intervals between neutron decay measurements a Bi calibration source was used to determine the detector drifts [Ast97]. For each neutron decay measurement the average of the preceding and successive value for the gain was then used. If the gain had drifted by more than 1% the data were excluded from the analysis. This happened in only 0.8% of all cases. Otherwise the data were then summed together taking into account the detector drift in a rebinning procedure. The statistical error for each bin after summing has to be still just the square root of the counts, as if this had been one bin from the beginning.

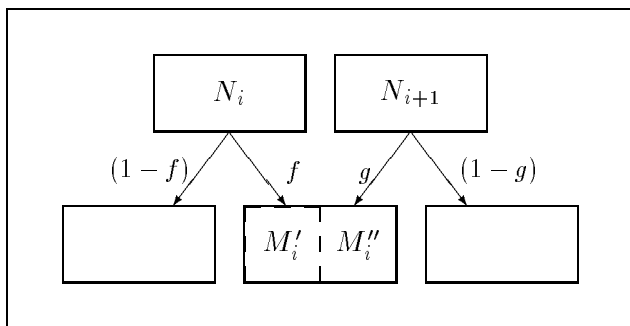


**Figure 3.15:** A schematic of the rebinning problem. Counts of two measured bins  $N_i$  and  $N_{i+1}$  have to be redistributed into one new bin  $M_i$ . The factors  $f$  and  $g$  are derived from the measured detector drifts.

Suppose that counts from two consecutive bins  $N_i$  and  $N_{i+1}$  have to be redistributed into a new bin  $M_i = fN_i + gN_{i+1} = M'_i + M''_i$  as illustrated in figure 3.15. The parameters  $f$  and  $g$  are calculated from the drift of the calibration line, with  $f + g \neq 1$  in general, since the width of the bins changes. One can not assume that the counts in the original bin are evenly distributed. Instead one has to take into account that the redistribution of counts in  $N_i$  follows a binomial distribution:

$$W(M'_i) = \binom{N_i}{M'_i} f^{M'_i} (1-f)^{N_i-M'_i}, \quad (3.17)$$

with an average of  $\overline{M'_i} = fN_i$  and an uncertainty of this average of  $\sigma_{M'_i}^2 = f(1-f)N_i$ . With this expression one correctly arrives at:

$$\Delta M_i^2 = f(1-f)N_i + f^2N_i + g(1-g)N_{i+1} + g^2N_{i+1} = fN_i + gN_{i+1} = \overline{M_i}. \quad (3.18)$$

Using this statistical uncertainty for each bin one obtains the correct values of the uncertainties of the parameters in the fits. However, if one rebins the counts according to the average  $\overline{M'_i} = fN_i$  the  $\chi^2$  determined in the fits is too small. Therefore in the rebinning procedure a Monte Carlo routine was used to really redistribute the counts according to the binomial distribution, Eq. (3.17).

In order to check this procedure the asymmetry was determined individually for data files between two calibration measurements without rebinning. The resulting distributions of deviations of the individual values from their average in units of their uncertainties are shown

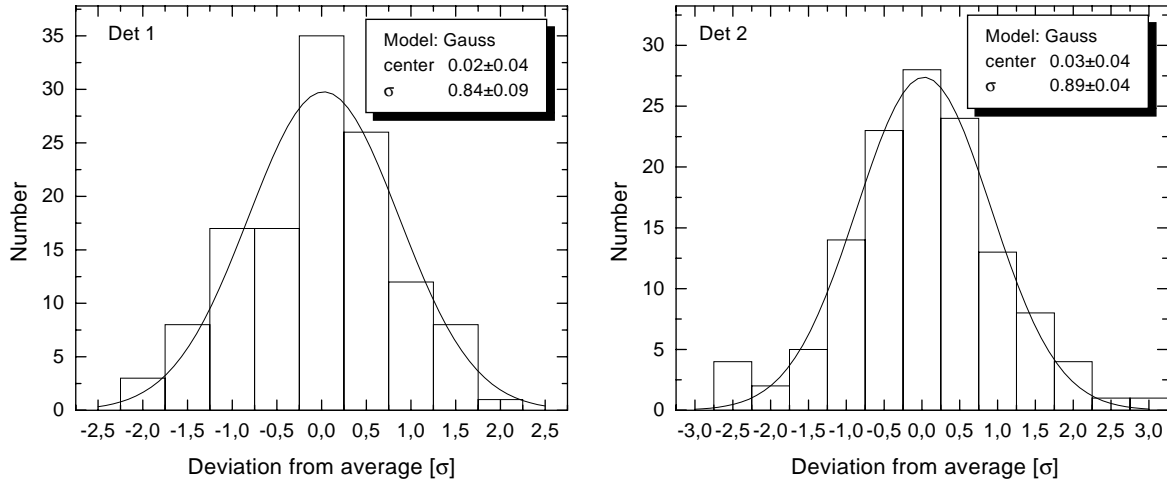


**Figure 3.16:** The distributions of deviations of  $A$  values from their average in units of their uncertainties. The data can be described by Gauss functions with  $\sigma \lesssim 1$  showing that the rebinning procedures works correctly.

in Fig. 3.16. The distributions for both detectors can be described with Gauss functions with  $\sigma_1 = 0.84$  and  $\sigma_2 = 0.89$ . And the average of the two distributions agreed well with the fit to the summed and rebinned data:

$$\begin{aligned} A_{1,\text{ave}}=0.11728(73) &\longleftrightarrow A_{1,\text{rebinned}}=0.11741(72) \\ A_{2,\text{ave}}=0.11651(72) &\longleftrightarrow A_{1,\text{rebinned}}=0.11633(72) \end{aligned}$$

### 3.3.4 Edge effect

The length of the decay volume is defined by aluminum baffles. The effective decay volume thus depends on the energy and the angle with respect to the magnetic field with which the electrons are emitted. Since electrons with a large angle, carrying a small asymmetry, are more likely to hit the baffles the effect will lead to an increased value of the correlation coefficient  $A$ . Also, since the gyration radius increases with energy, the effect will lead to a distortion of the energy dependence of the asymmetry. The probability for an electron to hit a baffle is given by [Rav95][Bae96]:

$$w(E) = \frac{2p}{eBL} \frac{1}{1 \pm \frac{1}{2}A\beta} \left[ \frac{\pi}{4} \pm \frac{A\beta}{3} \right], \quad (3.19)$$

where  $e, p$  are the electron charge and momentum,  $B$  is the magnetic field, and the signs depend on the hemisphere. This correction is included in the fit function (Appendix A). For the most energetic electrons  $A$  is increased only by about 0.35%. Averaged over the energy region used in the data analysis  $A$  has to be corrected by  $-0.24\%$  as is found from doing the analysis with and without the correction used in the fit function.

The only assumptions needed for this calculation are that all electrons with a center of motion closer to the baffles than their gyration radius really hit the baffles and that all electrons hitting the baffles are absorbed. The width of the baffles is with 3 cm wider than

the maximum pitch of 2.4 cm, thus the first assumption is realized. The only uncertainty remaining is due to electrons being backscattered rather than absorbed by the baffles. The backscatter probability from aluminum varies from 10 % to 80 % depending on the angle under which the electrons hit the surface [Ber63]. However, the backscattered electrons have a rather large probability to hit the baffle again since they lose some fraction of their energy. A Monte Carlo simulation taking both, the angular dependence and the energy loss, into account found only a negligible effect of 0.02 % due to electron backscattering [Glü98]. Thus, an uncertainty of 0.1 % in  $A$  is a conservative estimate for the uncertainty of this correction.

## 3.4 Backscattering

Backscattering is a well known problem in electron spectroscopy. When electrons are detected there is always the possibility for the electron to deposit only part of its energy in the detector before leaving it again. In the PERKEO spectrometer this effect is minimized for two reasons. The backscatter probability increases with the atomic number of the detector material. Thus the use of plastic scintillator leads to a small backscatter probability. The other advantage is that due to the magnetic field, backscattered electrons are either reflected back (by the magnetic mirror effect) to the same or guided to the opposite detector. Thus, by adding the energy deposited in all four PMT's for each event, we correctly determine the full energy of the electron even in case of backscattering. However, there are two systematic effects that will be discussed in the following. For backscattered events we have to determine which detector was hit first. Due to the limited time resolution there is an uncertainty introduced to the data analysis. The other effect is that a backscattered electron may be mistaken for an event in the detector hit second, if the first detector hit did not generate a trigger. The basic advantage of PERKEO is, as opposed to other neutron decay measurements, that due to the magnetic field we actually measure the events where an electron is backscattered from one detector to the other, allowing us to estimate the possible size of the effects. The probability for an electron to be backscattered from one detector to the other was measured to be  $N_{\text{back}}/N = 3.3\%$  from the number of events where both detectors had triggered to the total number of events.

### 3.4.1 Time resolution

Measuring the time of flight of electrons between the two detectors allows us to determine which detector was hit first. Any event triggering detector 1 gives a start signal to a TDC, a Time to Digital Converter. An event in detector 2 sends the corresponding stop signal, delayed by about 80 ns to insure a positive time difference. For backscattered events we thus obtain spectra of the time difference between the hits in the two detectors. In Fig. 3.17 the two peaks for the two detectors are clearly resolved. However, the cut made by the hardware was not set precisely at the minimum. In addition there are events that were not used in the data analysis at all (the invalid events).

In order to calculate the effect of events being missed in one detector ( $N_1$ ) on the asymmetry determined, a function  $cw(\phi)$  is introduced. This function gives the probability that an electron is backscattered in such a way that the measured time difference falls within the time range missed. The angle  $\phi$  is the angle of electron emission with respect to the neutron

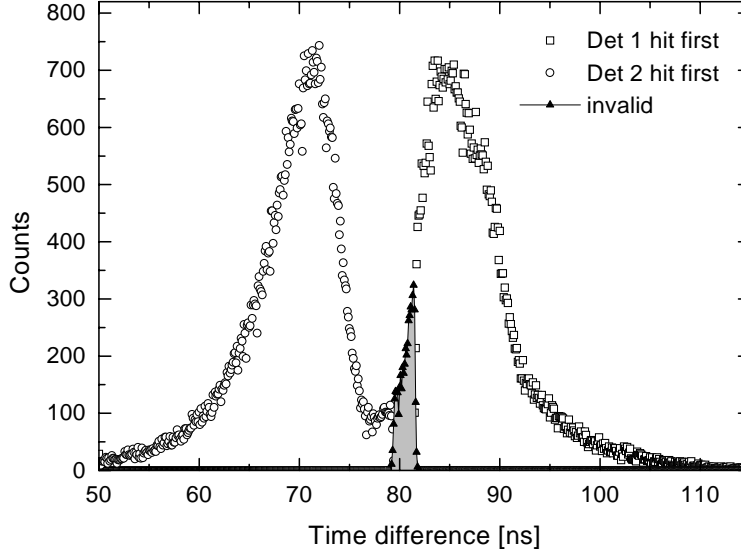


**Figure 3.17:** Time of flight spectrum between the two detectors. The invalid events are indicated in gray. They make up 0.11% of all events. Note, that only 3.3% of all events are backscattered and enter in this curve.

spin. The unknown angular dependence is separated from the measured fraction  $c$  of events in the time range by normalizing  $w(\phi)$  to unity over one hemisphere:

$$\int_0^{\pi/2} w(\phi) \sin(\phi) d\phi = 1. \quad (3.20)$$

The changes in the count rates for the two spin states are then:

$$\begin{aligned} N_1^\uparrow &\rightarrow \int_0^{\pi/2} N \{1 + A\beta \cos(\phi)\} [1 - cw(\phi)] \sin(\phi) d\phi \\ &= N \left\{ 1 + \frac{A\beta}{2} - c \int_0^{\pi/2} w(\phi) \sin(\phi) d\phi - cA\beta \underbrace{\int_0^{\pi/2} w(\phi) \cos(\phi) \sin(\phi) d\phi}_{c'} \right\} \\ &= N \left\{ 1 + \frac{A\beta}{2} - c(1 + A\beta c') \right\} \end{aligned} \quad (3.21)$$

$$N_1^\downarrow \rightarrow N \left\{ 1 - \frac{A\beta}{2} - c(1 - A\beta c') \right\}, \quad (3.22)$$

where  $c$  is the total fraction of events missed in the detector, averaged over both spin states. And the dependence of  $w(\phi)$  on the angle  $\phi$  is absorbed in  $c'$ , with  $0 < c' < 1$ . The effect on the experimental asymmetry is then:

$$\begin{aligned} A_{1,\text{exp}} &\rightarrow \frac{A\beta(1 - 2cc')}{2(1 - c)} \\ &\approx \frac{A\beta}{2} \{1 + c(1 - 2c')\}. \end{aligned} \quad (3.23)$$

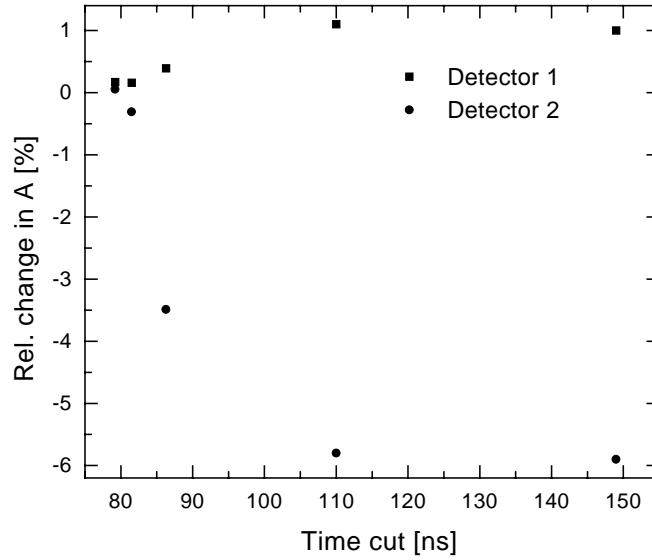


**Figure 3.18:** The relative change in the asymmetry obtained for the two detectors depending on the time cut chosen in the data analysis.

The most extreme assumption possible for the angular dependence would be a  $\delta$  function:  $w(\phi) \sin(\phi) = \delta(\phi - \phi_0)$  leading to  $c' = \cos(\phi_0)$ . Thus for  $\phi_0 = 0$  the asymmetry would be maximally decreased. This case corresponds to only electrons carrying the largest asymmetry being lost. In the opposite case,  $\phi_0 = \pi/2$ , the asymmetry would be increased. This situation corresponds to only electrons being lost that do not carry any asymmetry.

Similarly, the case where events are not missed in one detector, but instead events are added from the opposite detector can be calculated as well. This seems more appropriate for detector 2 since the time cut was not made exactly at the minimum. The effects on the count rates for the two spin states are then:

$$\begin{aligned}
 N_2^\uparrow &\rightarrow N \left\{ 1 + \frac{A\beta}{2} + d(1 - A\beta d') \right\} \\
 N_2^\downarrow &\rightarrow N \left\{ 1 - \frac{A\beta}{2} + d(1 + A\beta d') \right\} \\
 A_{2,\text{exp}} &\rightarrow \frac{A\beta}{2} \{ 1 - d(1 + 2d') \}
 \end{aligned} \tag{3.24}$$

The parameter  $d$  and  $d'$  are defined in the same way as  $c$  and  $c'$  before, however, the function  $w(\phi)$  may depend on the time range considered. The asymmetry can only become smaller in this case, as can be seen from Eq. (3.24). This is due to the fact that the count rate is large in one detector when it is small in the other one and vice versa.

The TDC spectra, shown in Fig. 3.17, are obtained by sorting the event mode data, where the TDC value for each individual event is stored. Due to a problem in the data acquisition, the TDC data are available only for two of the days used in the data analysis. For these days the data could be resorted according to a time cut set in the true minimum between the peaks. In the final analysis (Section 4.3.2) the resorted data were used. The effect of the time cuts not being set at the minimum on the other days was studied as well. In Fig. 3.18 the relative

change in the  $A$  values depending on the time cut is shown. For time cuts at  $t_C \geq 81.5$  ns the resulting asymmetry is decreased for the second detector and does not change as much for the first detector. This is expected since for cuts at larger times the conditions for the calculations above are fulfilled, namely that in detector 1 events are lost and in detector 2 events are added that belong to detector 1.

However, simulating the cut made by the hardware, adding all events with  $t \leq 79.2$  ns to detector 2, the asymmetry in detector 2 is not decreased but increased compared to the cut in the minimum ( $t_0 = 78.5$  ns):

$$\frac{\Delta A_2}{A_2} = 0.05\% .$$

This indicates that the counts in the time window between 78.5 and 79.2 ns still mostly belong to detector 2 which can be explained by the limited time resolution and the limited statistics. For detector 1 the cut made by the hardware leads to all events with  $t \geq 81.5$  ns being added to detector 1. This was found to increase the asymmetry by:

$$\frac{\Delta A_1}{A_1} = 0.16\% .$$

In the data analysis uncertainties of 0.15 % and 0.1 % are added to detector 1 and detector 2 respectively in order to cover this effect.

When all the backscattered events are attributed to only one of the detectors, the asymmetry in this detector is decreased by about 6 %, while the other one is increased by about 1 %. In this case the number of wrongly attributed events is known since the contribution from the region at the minimum, where the peaks are not well resolved, is small. Therefore, the numbers  $c$  and  $d$  from the Eqs. (3.23) and (3.24) can be determined using the constraint that the total energy of the event is in the region used for the data analysis. This way values of  $c'$  and  $d'$  can be calculated integrated over the time of flight between the detectors. The numbers obtained are in the range of 0.34 to 0.43. If the backscatter probability was independent of the angle of emission of the electrons a value of 0.5 would be expected. The fact that the measured values are smaller is explained by the increasing backscatter probability for decreasing angles of incidence.

This analysis was done averaged over all electron energies used in the data analysis. In principle an energy dependence is expected and would have to be considered when measuring the energy dependence of the asymmetry to determine the weak magnetism term.

### 3.4.2 Threshold effect in backscattered events

An electron backscattered from one detector to the other is mistaken for a single detector event in the second detector if the first detector did not trigger. The probability for a detector to trigger depending on the energy deposited is given by the trigger function  $T(C)$  that has been measured (Section 3.3.1). Knowing this function we can calculate the effect of this misassignment on the determination of the asymmetry. Spectra of the energy deposited in the first detector are created for all events where both detectors have triggered, using again the additional constraint that the total energy of the event is in the energy range used for the final data analysis. Then the spectra are corrected for the trigger efficiency by dividing

them by the trigger function. In Fig. 3.19 the measured and the corrected spectra are shown for both detectors. The difference of the corrected and the uncorrected spectra gives  $\Delta N$  the number of backscatter events missed in the detector hit first and incorrectly attributed to the detector hit second. In this way one obtains  $x_1 = 0.12\%$  ( $x_2 = 0.15\%$ ), the fraction of events missed by detector 1 (2) and attributed to detector 2 (1). The size of the effect on the determination of the asymmetry is calculated as in the last section. However, in the case considered now, events are lost to and added from the opposite detector at the same time. Therefore one obtains:

$$\begin{aligned} A_{1,\text{exp}} \rightarrow A'_{1,\text{exp}} &\approx A_{1,\text{exp}} \{1 + e(1 - 2e') - f(1 + 2f')\} \\ A_{2,\text{exp}} \rightarrow A'_{2,\text{exp}} &\approx A_{2,\text{exp}} \{1 - e(1 + 2e') + f(1 - 2f')\} \end{aligned}$$

Where  $e, e'$  ( $f, f'$ ) describe the events missed in detector one (two) as  $c, c'$  ( $d, d'$ ) in the preceding section, leading to  $e = x_1 = 0.12\%$  and  $f = x_2 = 0.15\%$ . Since  $e'$  and  $f'$  are independent of the time of flight it is appropriate to use the values measured at the end of the last section ranging from 0.34 to 0.43. As a realistic estimate, with a conservatively estimated uncertainty, we use  $e' = f' = 0.37 \pm 0.30$ . This leads to the following corrections to the results of the two detectors:

$$\frac{\Delta A_1}{A_1} = (0.26e - 1.74f) \pm 0.6\sqrt{e^2 + f^2} = 0.23(12)\% \quad (3.25)$$

$$\frac{\Delta A_2}{A_2} = (-1.74e + 0.26f) \pm 0.6\sqrt{e^2 + f^2} = 0.17(12)\% \quad (3.26)$$

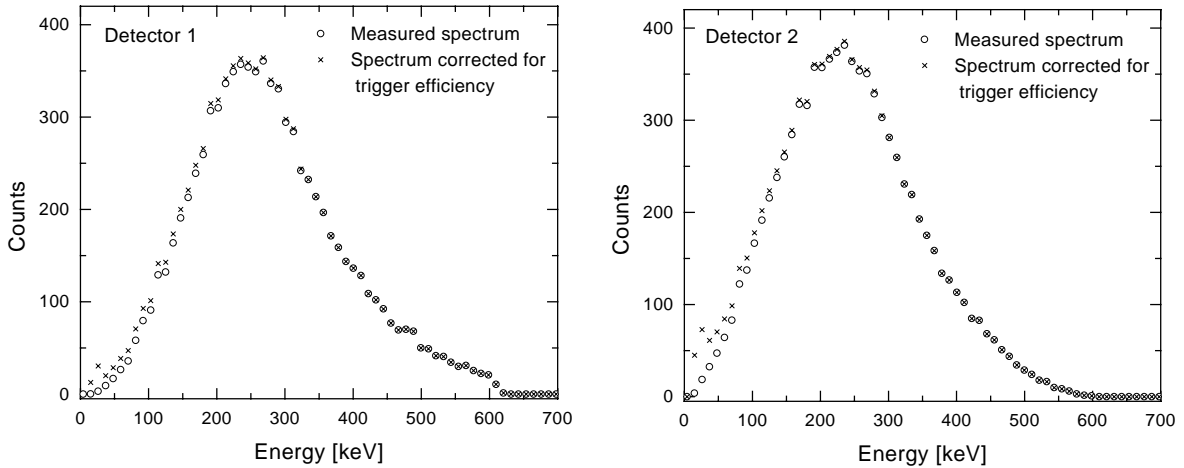


**Figure 3.19:** The limited trigger efficiency leads to a misassignment of events to the wrong detector in backscattering events. To determine the fraction of events missed in one detector the energy spectra for events where the detector was hit first are divided by the trigger function and then the difference is used. An extrapolation is required to low energies where the trigger efficiency goes to zero. Considering this, a fraction of  $x_1 = 0.12\%$  and  $x_2 = 0.15\%$  of all events is lost in the two detectors respectively and wrongly attributed to the opposite one. Without the extrapolation the respective fractions are  $x_1 = 0.10\%$  and  $x_2 = 0.12\%$ .

---

The asymmetries are washed out by the incorrect assignments to the hemispheres. Therefore, in the determination of the correlation coefficient the absolute values for both detectors have to be increased accordingly.



## Chapter 4

# The $A$ measurement

In this chapter the measurements of the last beam time leading to the determination of the correlation coefficient  $A$  are presented. The single largest correction to the final result is with (only) 1.1% the correction for the imperfect neutron beam polarization. Therefore the measurements and systematic checks performed to determine the degree of polarization are discussed first. The following section is dedicated to the measurements and analysis of background spectra. Only then the analysis of the electron emission asymmetry is shown and our final result is presented and its implications are discussed.

### 4.1 Polarization analysis

In measuring a distribution relative to the neutron spin the precision to which the neutron beam polarization is known enters directly into the uncertainty of our final result. The same holds true for the efficiency of the spin flipper. Thus it is crucial to achieve both, high polarizing and flipping efficiencies as well as precise measurements of these quantities.

The neutron beam is polarized using a supermirror polarizer built by O. Schärpf [Sch89]. A mirror for neutrons uses total reflection from a surface. The neutron optical density in vacuum is higher than in most materials (e.g. Nickel). Thus neutrons with an incident angle smaller than the critical angle are totally reflected. However, the critical angles achievable are small, of the order of 10 mrad for cold neutrons. A supermirror makes use of Bragg reflection to increase the critical angle. It consists of alternating layers of materials with a high and a low neutron optical density respectively (e.g. Nickel and Titanium). This leads to Bragg reflection due to constructive interference from all boundaries under a certain angle of reflection. By continuously varying the thickness of the layers the corresponding Bragg peaks can be made to overlap, leading to a reflection probability close to 100% for angles up to several times the critical angle of one layer (Fig. 4.1). Finally, a supermirror polarizer is made of supermirrors where one of the materials used is magnetic, such that for one neutron spin state the optical density in the magnetic layers is the same as in the nonmagnetic layers. This spin state thus passes through these layers undisturbed but is absorbed in bottom layers containing gadolinium. For the other spin state there is a difference in the optical densities of the magnetic and the nonmagnetic layers and it is thus reflected as in an ordinary supermirror. The optical density in the nonmagnetic layers has to be as close to zero as possible in order

to insure that all neutrons actually enter the multilayer. In practice, neutrons with very long wavelengths or incident under very small angles are reflected with either spin state. Therefore, the degree of polarization obtained with a supermirror type polarizer depends on the divergence of the beam and on the wavelengths of the neutrons.

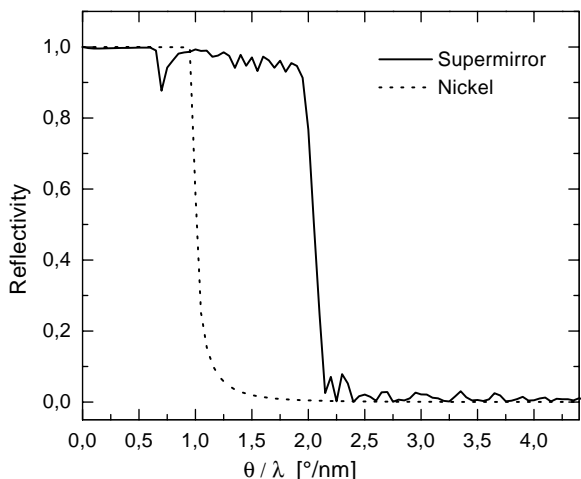


**Figure 4.1:** Calculated reflectivity curves for a Ni mirror and a supermirror. The supermirror has 77 layers. The critical angle obtained is twice the critical angle of the single Ni layer [Fie98].

As a spin flipper we use a current sheet [Abr62]. This is a rather simple device, consisting of a plane of wires all carrying a current in the same direction. Thus when the current is on, a magnetic field is produced that changes its direction very abruptly in the wire plane. The neutron spin follows the slowly changing magnetic field when nearing the spin flipper but cannot follow the abrupt change of the magnetic field direction inside the current sheet. This way effectively the magnetic field is flipped relative to the neutron spin. The condition for this transition to occur non adiabatically is that the Larmor precession frequency is smaller than the frequency with which the external field rotates in the frame of the moving neutron. For a cold neutron beam this condition can be fulfilled with reasonable magnetic fields, leading to typical values for the flipper efficiency of over 99%.

In the following section the mathematical formalism is shortly presented. Then a new device, the wavelength cutter, is described that was introduced in this beam time to facilitate the polarization measurement. Two ways of analysing the neutron beam polarization are discussed, one (Section 4.1.3) used in the beam time and the other one (Section 4.1.4) done later as a confirmation.

#### 4.1.1 Mathematical description

The polarization of a beam of spin 1/2 particles in an external magnetic field can be described using a classical two component vector. The actions of the spin manipulating devices can then be expressed by  $2 \times 2$  matrices. An unpolarized neutron beam is described by:

The polarizer must be kept in an external magnetic field to keep the magnetic layers uniformly magnetized. To polarize all the neutrons in a beam, a stack of glass substrates, each containing such multilayers on both sides, is used. Therefore, besides the neutrons with the ‘wrong’ spin state, there is always an additional loss of neutrons hitting the substrates from the front side. The transmission is typically of the order of 30%. Furthermore the stack of glass plates has to be curved to insure that all the neutrons are reflected from the multilayers at least once. In a collimated cold neutron beam an average polarization of around 99% can be obtained.

$$n = \begin{pmatrix} n^\uparrow \\ n^\downarrow \end{pmatrix} = n_0 \begin{pmatrix} 1 \\ 1 \end{pmatrix}. \quad (4.1)$$

A spin flipper is represented by a matrix with its large components in the off diagonal elements:

$$S = \begin{pmatrix} 1-f & f \\ f & 1-f \end{pmatrix}, \quad (4.2)$$

where  $f$  is the spin flip efficiency<sup>1</sup>. When the spin flipper is off:  $f = 0$ . The polarizer is represented by:

$$P = \begin{pmatrix} 1+p & B \\ B & 1-p \end{pmatrix}. \quad (4.3)$$

The off diagonal elements  $B$  describe a depolarization of the neutron beam inside the polarizer. In our measurement no such depolarization was found and we use  $B = 0$ . The polarizing efficiency of the polarizer is given by  $p$ . In the following  $p$  denotes the polarizing efficiency of the first polarizer, i.e. the polarization of the neutron beam, and  $p_A$  denotes the analysing efficiency of an analyzer. Finally, the neutron detection is independent of the neutron spin and the detector is thus described by:

$$D = \begin{pmatrix} 1 & 1 \end{pmatrix}. \quad (4.4)$$

Now the neutron count rate in a detector after an arbitrary combination of devices can be calculated by multiplication of the corresponding matrices. E.g. to determine the efficiency of one spin flipper one has to install a second spin flipper and an analyzer. The rate with both spin flippers on is then given by:

$$N_{11} = D \cdot P_A \cdot S_2 \cdot S_1 \cdot P \cdot n = 2(1 + pp_A(1 - 2f_1 - 2f_2 + 4f_1f_2)). \quad (4.5)$$

The spin flip efficiencies of both flippers can be obtained from measurements with the four possible combinations of flipper states:

$$f_1 = \frac{1}{2} \left( 1 + \frac{N_{11} - N_{10}}{N_{00} - N_{01}} \right) \quad (4.6)$$

$$f_2 = \frac{1}{2} \left( 1 + \frac{N_{11} - N_{01}}{N_{00} - N_{10}} \right). \quad (4.7)$$

The first (second) index on  $N$  refers to the first (second) spin flipper, with 1 (0) referring to the spin flipper being on (off).

---

<sup>1</sup>Serebrov [Ser95] uses  $1 - \epsilon$  for the spin flip efficiency and  $f = 1 - 2\epsilon$  for the flipper efficiency which corresponds to  $2f - 1$  in our notation.

### 4.1.2 The wavelength cutter

The polarizing efficiency of a supermirror polarizer drops for long wavelengths since for these neutrons the ‘wrong’ spin state also has a finite reflection probability. At the same time the neutron beam intensity is very low for such long wavelengths. This makes a precise determination of the degree of polarization difficult.

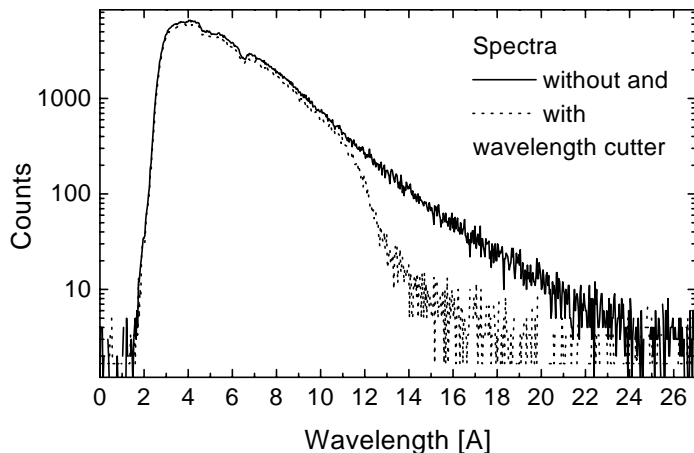


**Figure 4.2:** Wavelength spectrum measured with and without the wavelength cutter. The minima in the spectra correspond to wavelengths selected by other experiments upstream from PF1.

the coherent neutron scattering length. Thus by adjusting the angle of the device with respect to the neutron beam a maximum cut off wavelength can be chosen that is still transmitted by the device. All neutrons with longer wavelengths are reflected and thus removed from the beam. In Fig. 4.2 the neutron wavelength spectrum is shown measured with and without the cutter inserted. The chosen cut off wavelength is visible as well as a total loss of intensity of about 9% for wavelengths below 13 Å due to absorption and scattering in the glass substrates.

### 4.1.3 Supermirror polarization analysis

To determine the neutron beam polarization in the spectrometer we removed the last part of the beam tube downstream from the spectrometer and installed another spin flipper and a polarization analysing device built by Serebrov *et al.* [Ser95] instead. This device contains a chopper, two supermirror polarizers, and two more spin flippers in between. A schematic of the setup is shown in Fig. 4.3. There are always two spin flippers grouped together to allow measuring their flipping efficiencies as has been demonstrated above, Eq. (4.6). The chopper is necessary to determine the wavelength dependencies of the degree of polarization and of the flipper efficiency. The four spin flipper allow to do 16 different measurements corresponding to all possible combinations of flipper states. On the other hand, only 7 unknowns, the efficiencies of the flippers and polarizers, need to be measured. Thus, the problem is overdetermined allowing to do systematic consistency checks.

To avoid this problem a wavelength cutter was used in this beam time, effectively removing the neutrons with a wavelength above about 13 Å. This device [Høg99], consists of a stack of glass substrates covered with ( $m = 3$ ) supermirrors. The parameter  $m$  indicates that in these supermirrors the critical angle of total reflection achieved is three times the one from the surface of a Ni layer. The critical angle depends on the wavelength as:

$$\theta_{\text{crit}} \approx \sqrt{\frac{Nb_c}{\pi}} \lambda, \quad (4.8)$$

where  $N$  refers to the number density of the material and  $b_c$  refers to

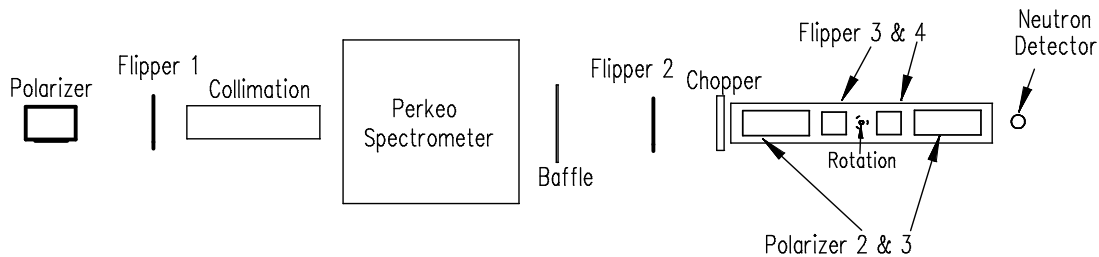


**Figure 4.3:** Schematic view of the setup for the polarization measurement.

The advantage of having two analyzers is, assuming there is no depolarization in the analysing device, that the two polarizers in series work as one ideal analyzer. The probability for a neutron with the ‘wrong’ spin state to pass through both closed analyzers is negligible:

$$P_{A2} \cdot P_{A1} = \begin{pmatrix} (1 + p_{A2})(1 + p_{A1}) & 0 \\ 0 & (1 - p_{A2})(1 - p_{A1}) \end{pmatrix} \approx \begin{pmatrix} (1 + p_{A2})(1 + p_{A1}) & 0 \\ 0 & 0 \end{pmatrix}.$$

In this case the polarization of the neutron beam can be measured, just using the first spin flipper:

$$p = \frac{\frac{N_0}{N_1} - 1}{1 + \frac{N_0}{N_1}(2f_1 - 1)}. \quad (4.9)$$

Here  $N_1$ ,  $N_0$  refer to measurements with the first spin flipper on and off respectively. This result is a consequence of the fact that with two polarizers only the product of their efficiencies is measured. If the analyzer is perfect this is sufficient. In practice one can not use this approximation. The two additional spin flippers in the analysing device also allow to measure the analysing efficiencies of the two analyzers.

A further feature of the used device is that it can be rotated around its axes (see Fig. 4.3) exchanging the positions of the two analyzers and spin flippers inside. The difference of the degrees of polarization obtained for the direct and reverse position of the device gives an estimate of the depolarization inside. This way a depolarization of the neutrons by more than 0.15% could be excluded in our measurement [Nes98]. However, this is not a general property of the device but may depend on the size, position, and collimation of the beam.

The possibility to rotate the device around its axes allows also to measure transmission curves for the different flipper states depending on the inclination angle. This was very useful to check systematic effects in the device due to changes in the neutron beam divergence caused by reflection from the curved supermirrors and imperfect optical adjustment of the components. If the first analyzer is ‘closed’ for the neutron beam, the acceptance of the device is limited only to neutrons with glancing angles of incidence. On the other hand, if the first analyzer is ‘open’ the acceptance is rather large even if the second analyzer is ‘closed’, since the angles are mixed in the first analyzer. Thus the widths of the peaks in the transmission curves depends on the setting of the spin flippers. The measured transmission curves were used as

input in a Monte Carlo simulation of the device, in order to extract the sensitivity of the polarization measurement to changes of the angular distribution of the beam. It was found that during the measurement the inclination angle has to be chosen in a regime where all the transmission curves have their maxima, in which case the systematic error due to a change of angular distribution in the beam was estimated to be about 0.15 % [Nes98].

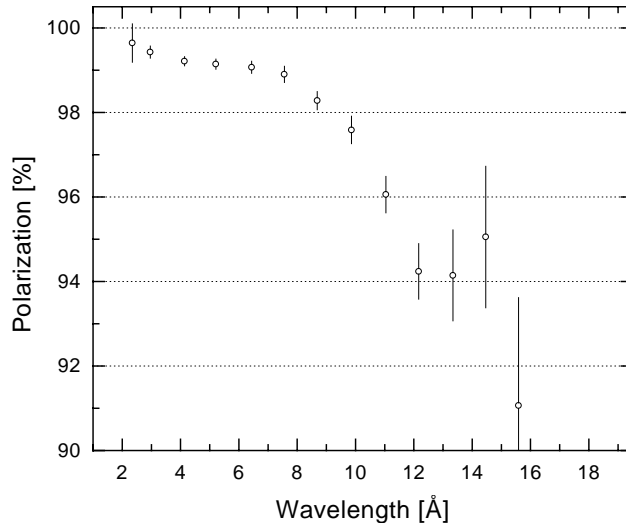


**Figure 4.4:** The measured wavelength dependence of the neutron beam polarization.

The acceptance of the device was smaller than the beam cross section. Therefore the beam had to be scanned. The beam may be restricted by just one baffle (in each dimension) and it has to be made sure that it will get to the detector without any further losses that would otherwise represent a cut in the divergence since the degree of polarization itself depends on the divergence. This requirement was facilitated by the narrow collimation of the beam. We measured the polarization of the neutron beam at three different horizontal positions. Due to the angular dependence of the polarizing efficiency of supermirrors a dependency on the horizontal position is expected since the polarizer was positioned vertically in the beam. The results for the different positions are summarized in Table 4.1.

Position	$p$	statistical	systematic
1	99.10%	$\pm 0.20\%$	$\pm 0.15\%$
2	99.10%	$\pm 0.10\%$	$\pm 0.15\%$
3	98.20%	$\pm 0.15\%$	$\pm 0.15\%$

**Table 4.1:** The measured values for the polarization at different horizontal positions across the beam.

In the vertical direction no dependence of the polarization on the position is expected. To check this, at each horizontal position the beam was scanned also in the vertical and spin flip ratios were measured. These are the ratios of rates measured with flipper on and off:

$$\frac{N_0}{N_1} = \frac{1 + pp_A}{1 + pp_A(1 - 2f)}. \quad (4.10)$$

The spin flip ratios agreed to within 0.25% at each position showing that indeed the degree of polarization is independent of the vertical position at this level.

In Fig. 4.4 the wavelength dependence of the neutron beam polarization as measured at one point in the beam is shown. The decrease for long wavelengths that motivated the use of the wavelength cutter is clearly visible. After weighting the result with the wavelength spectra measured at different points, the final result for the polarization is  $p = 98.9(3)\%$ . Similarly, the final result for the spin flip efficiency is  $f = 99.4(1)\%$  [Nes98].

#### 4.1.4 Polarized $^3\text{He}$ spin filter

A different method to determine the neutron beam polarization is the use of opaque spin filters. These devices remove one spin component from a neutron beam with very high efficiency. One possible realization is a target of polarized hydrogen [Zim95], making use of the strongly spin dependent scattering cross section. Another method, already further developed [Hei95], uses polarized  $^3\text{He}$ . There the absorption cross section is strongly spin dependent. It can be written as:

$$\sigma_{\text{abs}} = \sigma_0 \pm p_N \sigma_p. \quad (4.11)$$

Where  $p_N$  refers to the nuclear polarization and the sign depends on the state of the neutron spin relative to the nuclear polarization. The total absorption cross section,  $\sigma_0 = 5327(10)$  b at  $v = 2200 \frac{\text{m}}{\text{s}}$  [Als64], is large and solely due to processes with neutron and nuclear spin antiparallel to each other:  $\sigma_p = -1.013(42)\sigma_0$  [Pas66]<sup>2</sup>. Thus a neutron beam is very effectively polarized when passing through a cell with polarized  $^3\text{He}$ . However, since the absorption cross section scales with the velocity as  $1/v$  the efficiency is strongly dependent on the wavelength. To obtain high efficiencies for the short wavelengths the cell has to be made thick and the gas pressure high. On the other hand the transmitted intensity then is decreased leading to limited statistics for the longer wavelengths. In practice to analyze the whole wavelength spectrum of a cold neutron beam one needs at least three cells at different pressures.

During the beamtime this method had not yet been available. Later an experiment was performed comparing the two spin filters with the supermirror analysing device [Zim99a], and in the beginning of 1999 we did another experiment, comparing just the  $^3\text{He}$  spin filter with the supermirror device using a beam collimated more similarly to the one from our beam time [Zim99b].

An initially unpolarized neutron beam will acquire a degree of polarization  $p_A(d)$  after passing a distance  $d$  through  $^3\text{He}$  that is given by:

$$p_A(d) = \tanh(\sigma_p p_N N d), \quad (4.12)$$

where  $N$  refers to the number density of the gas. An advantage of this method is that if the opacity  $x = \sigma_p p_N N d$  is made sufficiently large ( $x \gtrsim 3.5$ ) the analysing efficiency  $p_A$  is not

<sup>2</sup>The small contribution from scattering is neglected.

sensitive to the opacity:

$$\frac{\delta p_A}{p_A} = \frac{2x}{\sinh(2x)} \cdot \frac{\delta x}{x}. \quad (4.13)$$

When measuring the spin flip ratio with a supermirror analyzer, the low rate is always obtained with the spin flipper on. Thus the measurement is rather sensitive to the efficiency of the spin flipper. Another advantage of the  $^3\text{He}$  method is that the direction of the nuclear polarization is made such that the polarized neutron beam is blocked when the spin flipper is off. In this case the spin flip ratio  $R$  is rather insensitive to the spin flip efficiency:

$$R = \frac{N_1}{N_0} = \frac{1 + (2f - 1)p_{AP}}{1 - p_{AP}}. \quad (4.14)$$

From this spin flip ratio the polarization of the neutron beam can be derived in an excellent approximation, without having to know the flipper efficiency precisely (as long as  $f \approx 99\%$ ):

$$\frac{R - 1}{R + 1} \approx p_{AP} \{1 + (f - 1) \cdot (1 - p_{AP}f)\} \approx p_{AP}. \quad (4.15)$$

Thus the problem of measuring the polarization is reduced to insuring that the analysing efficiency of the gas cell is sufficiently high,  $p_A \geq 99.9\%$ . For a given gas pressure, cell

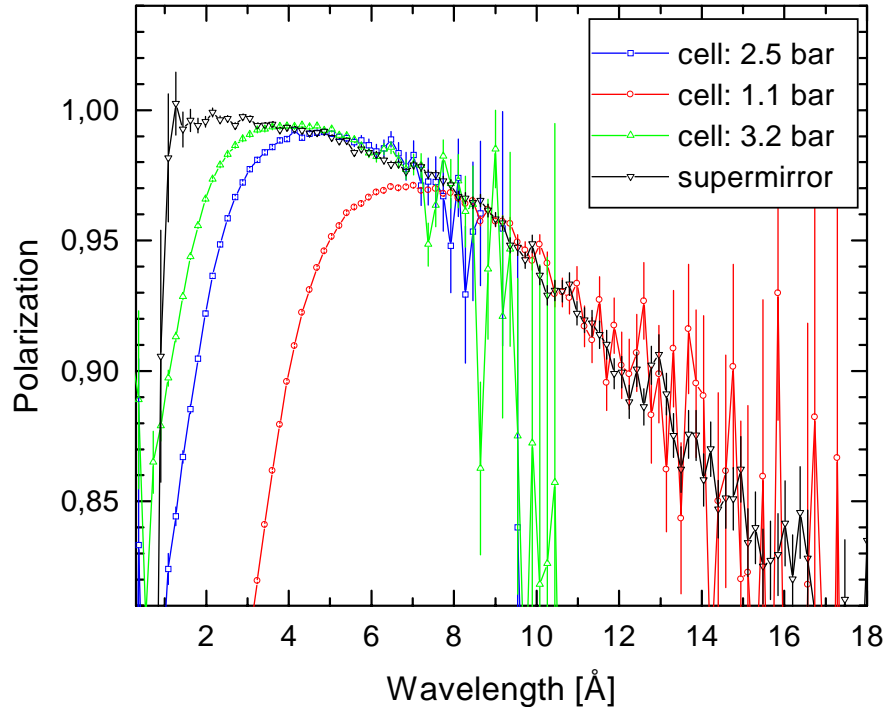


**Figure 4.5:** The polarization as measured with the three different  $^3\text{He}$  cells is shown together with the result from the measurement with the supermirror analyzer. The different sensitive regions for the gas cells with the given pressures is visible. For all gas cells the length was 94 mm and the polarization in the  $^3\text{He}$  was 53 %. The fall off at small wavelengths is due to the limited analysing power at small wavelengths whereas at high wavelengths the statistical uncertainty becomes large.

Wavelength range	$^3\text{He}$	Supermirror analyzer
3.2 - 13.0 Å	98.26(2)%	98.14(2)%

**Table 4.2:** The polarization averaged over the accessible range of the neutron spectrum measured with the supermirror and the  $^3\text{He}$  spin filter. Only the statistical uncertainties are given.

thickness and nuclear polarization this corresponds to a minimum neutron wavelength due to the  $1/v$  dependence of the absorption cross section. We used three cells with different pressures to cover most of the neutron wavelength spectrum. The measured polarization for the three cells versus the neutron wavelength is shown in Fig. 4.5. The polarization measured with the supermirror device is also shown in the same plot. For a correct comparison these curves still have to be weighted with the neutron wavelength spectrum. The results for the average neutron beam polarization are shown in Table 4.2. Both methods agree with the spin filter method yielding a slightly higher result for the polarization by 0.12(3)%. However, this deviation is covered by the systematic uncertainty of our measurement.

#### 4.1.5 Spin filter versus supermirror analyzer

To summarize the two preceding sections the two presented methods for polarizing a neutron beam are compared in Table 4.3.

	Supermirror device	$^3\text{He}$ spin filter
Time dependence	+	-
Transmission $\times$ polarization	+	-
Size	-	+
Analysing size/time	-	+
Homogeneity requirement	+	-
Systematic limitation	$\approx 0.2\%$ [Ser95]	$< 0.1\%$ [Hei95]

**Table 4.3:** A comparison between the supermirror analyzer and a  $^3\text{He}$  spin filter.

The disadvantages of the  $^3\text{He}$  spin filter are the trade off between high transmission and high polarization efficiency and the time dependence due to the relaxation of the nuclear polarization in the gas. In statistically limited experiments, requiring long measuring times and high transmission, the use of  $^3\text{He}$  to polarize the neutron beam is thus not feasible. The advantages of the new method lie in the polarization analysis. There the required measuring times are small compared to the relaxation time. The scanning of the beam is no longer required, since the acceptance of one cell can be made large enough to measure a beam like the one we used at once. However, in this case the rate may lead to a large dead time correction, thus still making a scan necessary. Nevertheless, the systematic effects are much smaller since the difficult divergence, alignment, and possible depolarization effects in supermirrors are avoided. One difficulty with using the  $^3\text{He}$  spin filter (especially close to the PERKEO spectrometer) is the requirement that the average relative magnetic field gradient in the gas cell has to be of the order of  $\frac{dB/dx}{B} \leq 10^{-3} \text{ cm}^{-1}$  to obtain sufficiently long relaxation times.

### 4.1.6 The polarization monitor

Another new feature in this beam time was the possibility to monitor the polarization of the neutron beam. A hole was left open in the beam stop that could be controlled by a shutter and an analyzer was installed (see Fig. 3.1). With this arrangement spin flip ratios were measured at regular intervals during the beam time.

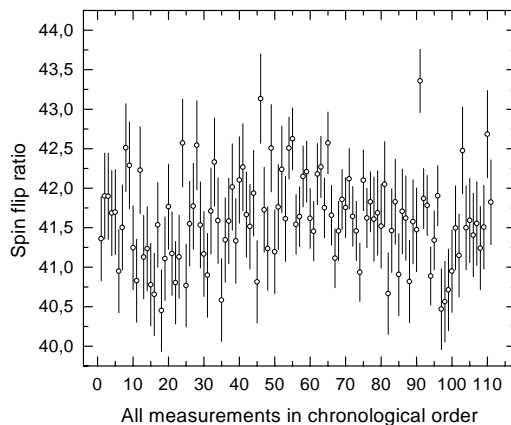


**Figure 4.6:** The relative variation of spin flip ratios measured with the monitor during the beam time.

The measured flipping ratios are shown in Fig. 4.6. The average was found to be  $R = 41.6$  leading to an analyzing efficiency of  $p_A = 97.5\%$  using the measured values of  $f = 99.4\%$  and  $p = 98.9\%$ . The reason that the flipping ratio was not higher is probably due to the analyzer position not being optimized and the beam exit window containing magnetic parts. In any case it was sufficient to check the stability of the degree of polarization. A histogram of the relative deviations from the average normalized to the statistical uncertainties can be described by a gaussian distribution with  $\sigma = 1.07$ . Therefore the degree of polarization remained constant to within 0.05%.

## 4.2 Background

The background in the spectrometer can be divided into a beam independent part and a contribution induced by the neutron beam. The beam independent part is measured with the beam intercepted by shutter up and subtracted from the raw data. This correction is done in the first step of the data analysis. The beam dependent part can not be measured and therefore has to be suppressed as much as possible. This is mainly achieved by designing the spectrometer and beam tubes large enough to avoid any possibility for the neutron beam to hit any material other than the beam stop and the baffles. In this beam time additional efforts were made to suppress the beam related background further (Section 3.1.3). As will be shown below, the correction for beam related background to the final result has been decreased by a factor of 3 in comparison to the previous beam time.

### 4.2.1 Beam independent background

The spectra taken in one of the detectors for both spin states are shown in Fig. 4.7. The asymmetry is clearly visible already in the raw data. Together with the neutron decay data a background spectrum is shown, measured with the neutron beam intercepted by our first beam shutter (shutter up, see Fig. 3.1) shortly after the polarizer. In a first step of data analysis this background spectrum is subtracted from the raw data. This is a correction of about 10% to the count rate in the energy region later used in the data analysis. The correction is assumed to be exact, canceling environmental background and background introduced by the polarizer. Environmental background in our case refers to all background not related to the neutron beam, i.e. background due to the reactor, due to natural radioactivity, background induced by cosmic rays and also some background due to imperfectly shielded calibration sources.

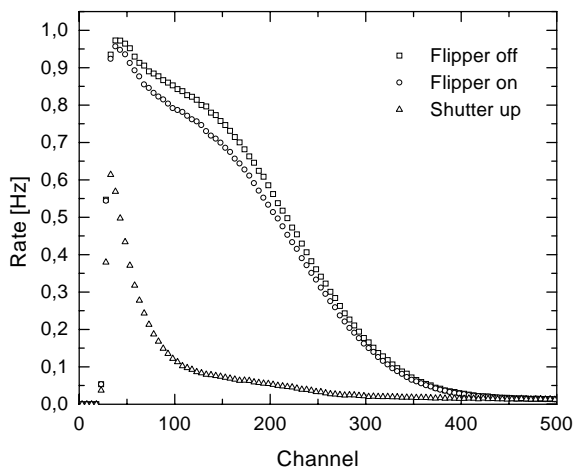


**Figure 4.7:** Raw data taken in detector 1 for both states of the spin flipper and also with the neutron beam intercepted by the first shutter. The background spectrum measured with shutter up closed is subtracted from the raw data in the first step of the data analysis.

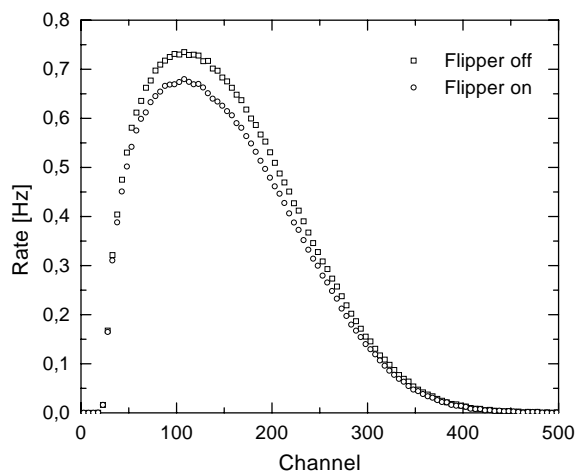


**Figure 4.8:** The raw spectra measured in detector 1 after subtraction of environmental background (shutter up closed). The shapes already look like typically allowed beta spectra and the asymmetry between the two spin states is clearly visible.

A possible variation of the background spectrum should be slow and is taken into account by measuring the background at regular intervals. Another possible systematic effect is the background produced by stopping the beam in the shutter. If this contribution to the background spectrum was large the correction could be too large also. However, the additional background introduced by shutter up is negligible, as was shown in a detailed estimate in [Mül96]. The estimate uses the low probability for secondary radiation to be emitted after neutron capture on  ${}^6\text{Li}$  and the small solid angle extended by the detectors as seen from the position of shutter up. The raw data after subtracting the background are shown in Fig. 4.8. The remaining count rate above the endpoint of the beta spectra indicates that the background that still has to be taken into account is very small, as will be discussed in the following section. The neutron decay rate measured was about 300 Hz in accordance with the estimate in Eq. (3.3).

### 4.2.2 Beam dependent background

The determination of the beam related background is based on some assumptions since it can not be measured directly. The most straightforward way is to determine the counts above the neutron beta decay endpoint and to extrapolate this background to lower energies. To do this one has to know the shape of the background spectrum. Estimates for the shape are obtained by measuring spectra from different sources that are compared in Fig. 4.9. The spectra are normalized to the count rate above the endpoint in the beta spectrum. In the region used for the data analysis (channel 150 - 300) all the spectra are structureless and their shapes agree well. This is expected since the background is due to multiple scattered gamma rays from neutron absorption and to electrons produced inside the spectrometer by photo and Compton effect.

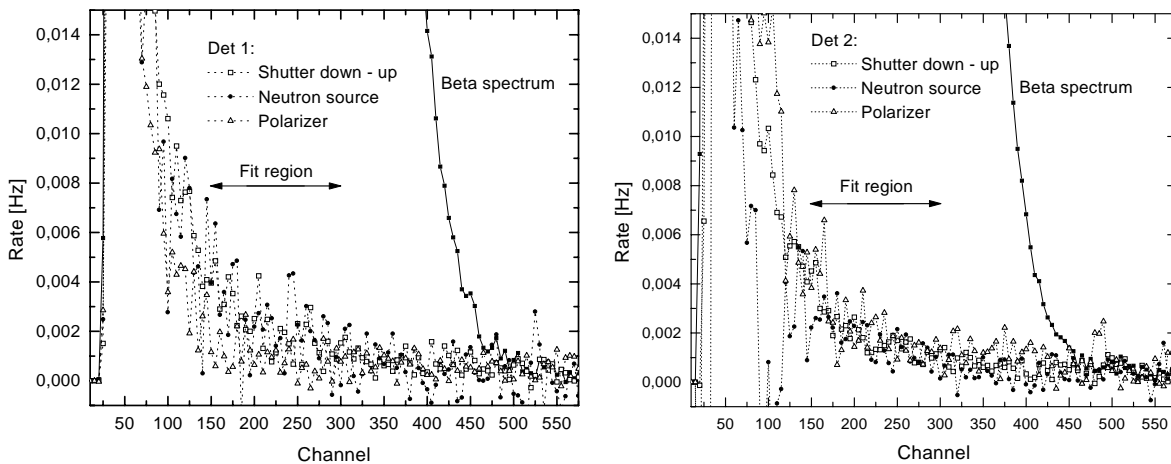


**Figure 4.9:** The spectra from a neutron source, a  $\gamma$  source (the polarizer), and shutter down are compared with the beta spectrum. The background spectra are scaled to the counts remaining in the beta spectrum above the endpoint. The maximum rate for the beta spectra is about 0.7 Hz as can be seen from fig. 4.8.

The difference of spectra from shutter down and shutter up scaled to the rate above the endpoint is used as the estimate for the beam related background in the data analysis. This difference should be a good approximation to the true spectrum since it is produced by the beam being stopped in the  ${}^6\text{Li}$  of the shutter and the collimation system, while the true spectrum is produced by the beam being stopped in the  ${}^6\text{Li}$  of the collimation system and the beam stop. Using this difference also has the advantage that these spectra were always measured at regular intervals (the measurement cycle is described in [Ast97]) during the beam time, thus taking into account possible fluctuations.

During the beam time a piece of  ${}^6\text{LiF}$  had fallen off from one of the baffles, leading to the neutron beam hitting the stainless steel support. This was discovered when the background situation was checked with a Ge detector [Pes98]. By taking the difference of spectra before and after this was fixed, the contribution of this activation was extracted and is shown in Fig. 4.10. Again the shape of the spectrum is structureless and agrees with the ones in Fig. 4.9. Also the intensity from this source alone is about the same (not scaled) as from the total beam related background. Thus, besides the expected background from the beam stop

and the collimation, there is no room left for another contribution from the beam hitting any material unplanned.

Two other methods to determine the beam related background are discussed in [Bae96]. Both make use of the double differences of spectra as discussed before (Section 3.3.2). The difference between neutron decay spectra and background spectra (shutter up closed) are taken, with the magnetic field on ( $N_B$ ,  $B_B$ ) and off ( $N_0$ ,  $B_0$ ):

$$\begin{aligned}\Delta_4 &= N_B - B_B - (N_0 - B_0) \\ &= \Delta_{2,B} - \Delta_{2,0}.\end{aligned}$$

In this beam time the remaining counts above the endpoint were consistent with zero in  $\Delta_4$ .  $\Delta_{2,B}$  is just the neutron decay spectrum corrected for the subtractable, not beam related background as already discussed in Section 4.2.1. Using  $e_n$  and  $\gamma_n$  for the contributions from electrons and  $\gamma$  rays to the spectrum with the neutron beam on, and  $\gamma_B$  for the background contribution without neutron beam, one obtains:

$$\Delta_{2,B} = e_n + \gamma_n - \gamma_B = e_n + \gamma_{\text{beam}}. \quad (4.16)$$

Similarly for the measurements with magnetic field off one obtains:

$$\Delta_{2,0} = e_{n,0} + \gamma_{n,0} - \gamma_{B,0} = x \cdot e_n + \gamma_{\text{beam},0}. \quad (4.17)$$

The goal is to determine the remaining beam related background  $\gamma_{\text{beam}}$  using the measurements without magnetic field ( $\Delta_{2,0}$ ). Without the magnetic field a fraction  $x$  of electrons

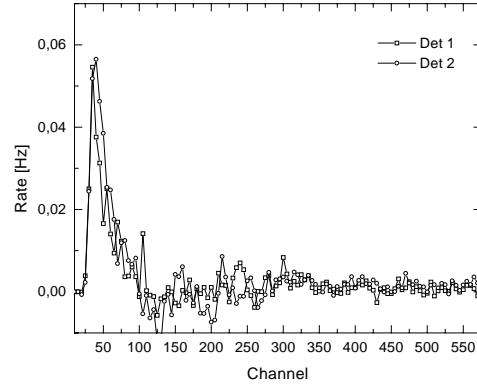


**Figure 4.10:** The background produced by a broken baffle. The neutron beam is hitting a stainless steel support.

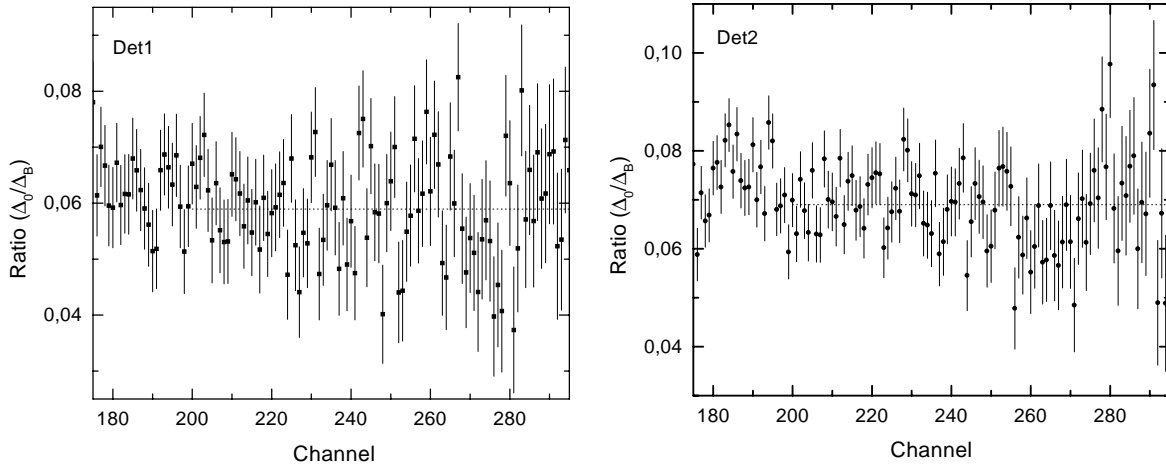


**Figure 4.11:** The ratio of differences of spectra with the magnetic field off and on is shown. The fraction of electrons from the neutron beam reaching the detector without magnetic field is determined from the ratio in the region where the beta spectrum is large compared to the background.

from neutron decay still reaches the detector. Also one has to distinguish  $\gamma_{\text{beam}}$  from  $\gamma_{\text{beam},0}$ . When the magnetic field is on the gamma background is smaller than when the field is off ( $\gamma_{\text{beam}} < \gamma_{\text{beam},0}$ ), since the magnetic field effectively shields the detectors from most electrons produced in the spectrometer. The relative increase in background for the two detectors can be determined from the difference of measurements with shutter up closed and the magnetic field on,  $B_B$ , and off,  $B_0$ , integrated over the whole spectrum:

$$f_1 = \frac{B_0 - B_B}{B_B} = 0.73 \quad \text{and} \quad f_2 = 0.48. \quad (4.18)$$

The shielding of detector 1 is better than that of detector 2 since the device containing the calibration sources was installed on the side of detector 2. Assuming that these factors are independent of the source of the gamma background they can also be used to estimate the difference between  $\gamma_{\text{beam}}$  and  $\gamma_{\text{beam},0}$ . The fraction  $x$  is determined by forming the ratio :

$$\frac{\Delta_{2,0}}{\Delta_{2,B}} \approx x + (1 + f) \frac{\gamma_{\text{beam}}}{e_n}. \quad (4.19)$$

The approximation is valid in the region where the spectrum is dominated by the beta spectrum of the decay, and  $\gamma_{\text{beam}}/e_n \approx 0.5\%$ . The ratios for the two detectors are shown in Fig. 4.11. The values of  $x$  obtained for the two detectors are  $x_1 = 5.0(9)\%$  and  $x_2 = 6.2(9)\%$ , where the uncertainties are a combination of the statistical uncertainty of the ratio and a systematic uncertainty of the order of the correction  $(1 + f) \frac{\gamma_{\text{beam}}}{e_n}$ . Now the second estimate for the beam related background  $\gamma_{\text{beam}}$  is obtained by the following combination of spectra:

$$\frac{1}{1 + f} (\Delta_{2,0} - x \cdot \Delta_{2,B}) = \frac{1}{1 + f} (\gamma_{\text{beam},0} - x \cdot \gamma_{\text{beam}}) \approx \gamma_{\text{beam}}. \quad (4.20)$$

The resulting background spectra are shown in Fig. 4.12 together with the spectra obtained from the first method. The agreement in detector 1 is excellent. However, in detector 2

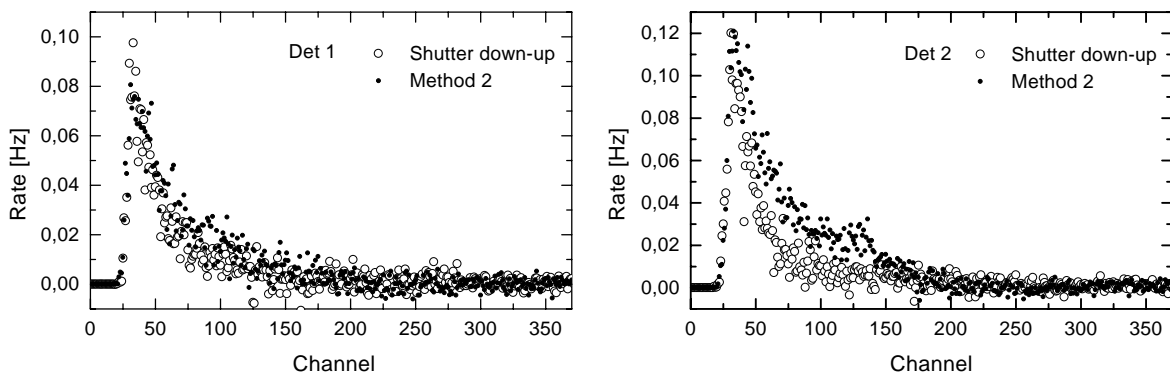


**Figure 4.12:** The estimates for the beam related background spectra obtained for the two detectors by two methods is compared. The first method scales a measured background spectrum to the count rate above the endpoint of the beta spectrum, thus relying on the assumption that the measured spectrum has the same shape as the beam related background. The second method uses measurements with magnetic field on and off to separate the  $\gamma$  background.

there is a deviation below channel 150. The second method is not as reliable as the first one due to the rather large uncertainty in  $x$ . Also the measurements without the magnetic field were done only once during the beam time. However, the systematics are different in the two methods and thus it represents an independent confirmation of the first method.

The third method described in [Bae96] can not be used since it relies on a relative scaling of the double and single differences  $\Delta_4$  and  $\Delta_{2,B}$  of spectra measured with shutter down closed. In this beam time the background was that small that the statistical uncertainty in this method became too large.

### 4.2.3 The effect on the asymmetry

When determining the experimental asymmetry, the background contribution cancels in the nominator but enters in the denominator:

$$A_{\text{exp},B} = \frac{N^\uparrow - N^\downarrow}{N^\uparrow + N^\downarrow + 2B} \approx A_{\text{exp}} \left(1 - \frac{2B}{N}\right). \quad (4.21)$$

Thus the size of the correction to  $A$  is of the order of the background to signal ratio for each spin state. Although the correction is done energy dependent by subtracting the spectra, the integrated background rate gives an estimate of the size of the effect. In Fig. 4.13 the integrated background rates are shown for the two methods. Both methods of determining the background agree roughly. In the region used in the final analysis (channel 150 to 300) the integrated background rate is about 0.30(15) Hz, with the relative uncertainty of 50% being a conservative estimate covering the deviation between the different models. The integrated neutron decay rate averaged over both spin states is about 60 Hz in the same region. Thus the size of the correction is only of the order of 0.50(25)% as opposed to 1.55(45)% in the last measurement [Bae96].

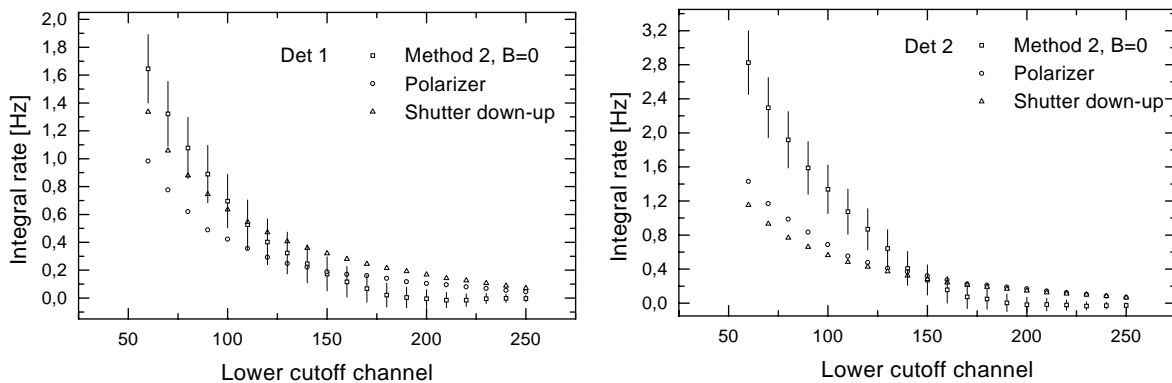


**Figure 4.13:** The integrated count rates for different background models in both detectors. The lower integration boundary is varied while the upper one is kept at fixed at channel 300.

### 4.3 Determination of the correlation coefficient $A$

In this section the final result of the analysis is presented. First the  $\beta$ -spectra are shown as an indication of how well the determined detector function allows us to describe the data. This also demonstrates the quality of the background subtraction. Then the experimental asymmetries and the fits to the data are presented. The difference between the two detectors is discussed and systematic checks like varying the region used for the fits and fitting different parts (days) of the data separately are shown. Finally, all the corrections and uncertainties entering the analysis are summarized.

#### 4.3.1 Beta spectra

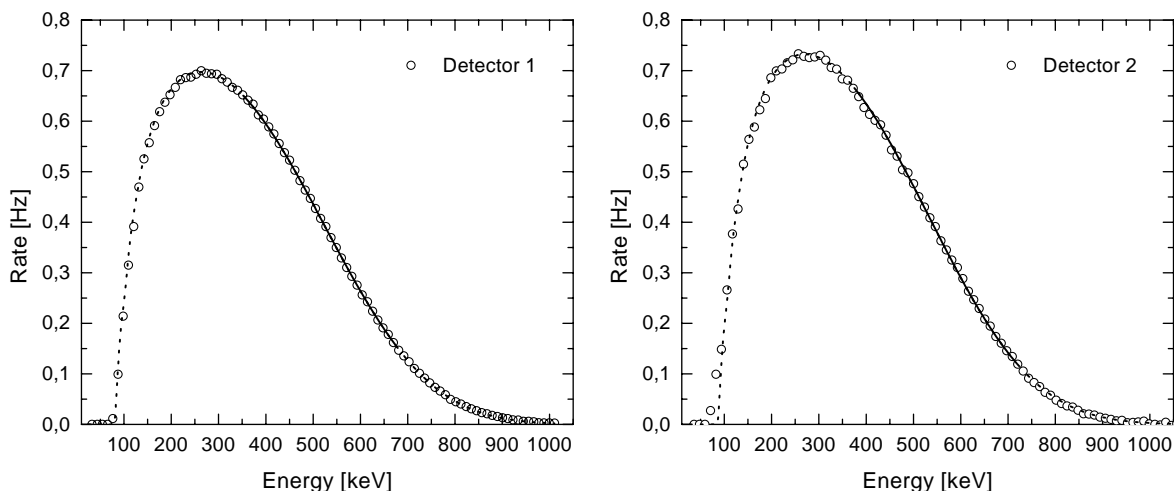


**Figure 4.14:** The beta spectra for the two detectors and the corresponding fits. The fit region is indicated by the solid line. The fact that even the extensions of the fits describe the data well demonstrates the quality of detector function and background subtraction.

A fit to the unpolarized beta spectrum is a test of both, the correctness of the detector function and the subtracted background. Since we do not measure without the polarizer<sup>3</sup> we obtain unpolarized spectra by adding the data taken for both states of the spin flipper. Using the notation from Section 4.1.1, the neutron beam is described by:

$$n_{\text{off}} = \begin{pmatrix} 1 + p \\ 1 - p \end{pmatrix} \quad \text{and} \quad n_{\text{on}} = \begin{pmatrix} 1 - p(2f - 1) \\ 1 + p(2f - 1) \end{pmatrix},$$

when the flipper is turned off and on respectively. This leads to the following spectra in the detectors:

$$N_{\text{off}} = 2F(E)' \left\{ 1 \pm \frac{1}{2} A \beta p \right\} \quad (4.22)$$

$$N_{\text{on}} = 2F(E)' \left\{ 1 \mp \frac{1}{2} A \beta p (2f - 1) \right\} \quad (4.23)$$

<sup>3</sup>Taking out the polarizer would change the beam direction thus requiring also a new alignment of the whole setup.

where the upper (lower) sign refers to detector 1 (2). Thus the polarizing and flipping efficiencies lead to a deviation from the true unpolarized beta spectrum  $F(E)'$  according to:

$$N_{\text{off}} + N_{\text{on}} = 4F(E)'(1 \pm \frac{1}{2}A\beta p(1-f)) \approx 4F(E)'. \quad (4.24)$$

The two signs refer to the two detectors and the approximation is good since:

$$\frac{1}{2}A\beta p(1-f) \leq 3 \cdot 10^{-4}.$$

The data are corrected for background and in the fit the theoretical function  $F(E)'$  is convoluted with the detector function. The result is shown in Fig. 4.14. The agreement is excellent, even the extensions of the fits describe the data well to low energies.

### 4.3.2 Experimental Asymmetry

The final result for the correlation coefficient  $A$  is obtained from a fit to the experimental asymmetry:

$$A_{\text{exp}} = \frac{N^{\uparrow} - N^{\downarrow}}{N^{\uparrow} + N^{\downarrow}} \approx \frac{F(E)' \cdot 1/2A_{\text{raw}}\beta p f}{F(E)'}. \quad (4.25)$$

Here the correlation coefficient has been denoted  $A_{\text{raw}}$  since there are still corrections that will be applied in the following section to obtain the final value for  $A$ . The same approximation as above, Eq. (4.24), has been used in the denominator. In the final result this correction is negligible since it has opposite signs for the two detectors and thus only enters quadratically when the two detectors are averaged. For the individual detectors a difference on the order of  $3 \cdot 10^{-4}$  can be attributed to this correction. In Eq. (4.25) the Fermi spectrum  $F(E)'$  is not cancelled, since in the fit nominator and denominator have to be convoluted separately with the detector function. The complete detector function used in the fitting routine is given in appendix A. The results are shown in Fig. 4.15, yielding:

$\begin{aligned} A_{\text{raw},1} &= 0.11741(72) \\ A_{\text{raw},2} &= 0.11633(72) \end{aligned}$
--

The energy region used in the fits (channels 150 - 300) was chosen to minimize the uncertainty in the background correction. As a further systematic check, the fit region was varied. The dependence of the resulting value for  $A_{\text{raw}}$  on the lower cutoff channel is shown in Fig. 4.16. The variation of the  $A_{\text{raw}}$  values found can be explained by statistics.

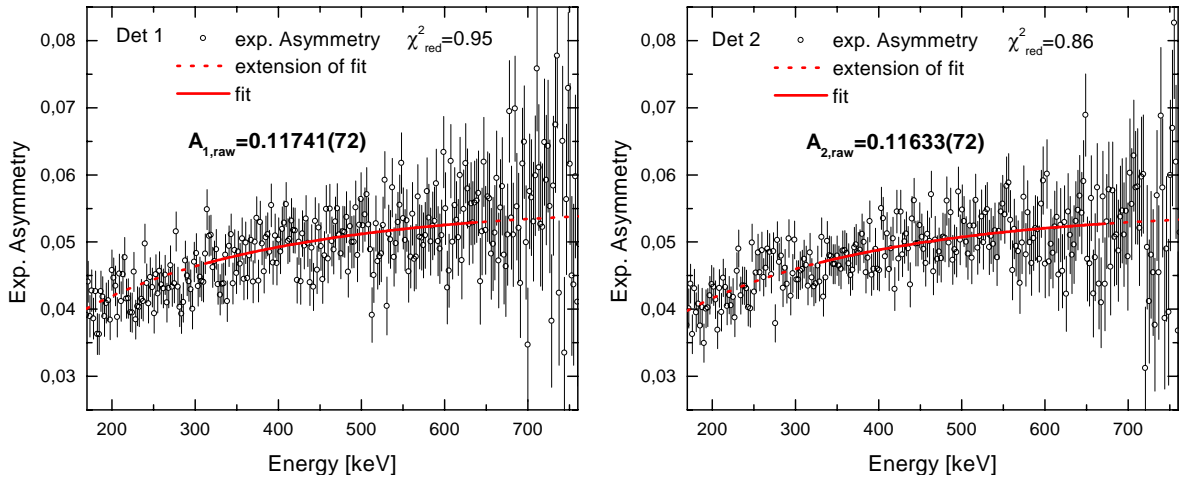


**Figure 4.15:** The fits to the experimental asymmetries determined in both detectors. The fits describe the data well even in their extensions.

In Fig. 4.17 the resulting values of  $A_{raw}$  from different days of the beam time are shown. The first two days shown were not used in the final analysis. The first day was excluded since the background situation was not yet at its optimum (this was before the broken baffle was fixed, Section 4.2.2). The next day was excluded since the spin flipper failed sometime during the measurement. For the rest of the beam time it was monitored. The averages of the individual days lead to  $A_{raw,1} = 0.11733(72)$  and  $A_{raw,2} = 0.11638(71)$ , in agreement with the fits to the summed data. The small deviation can be explained by the background subtraction working slightly different for the individual days. The scatter of the daily values leads to  $\chi^2_{red} = 0.20$  and  $\chi^2_{red} = 1.25$  for the averages of the two detectors. The statistical probability to obtain  $\chi^2_{red} = 1.25$  for six degrees of freedom is about 30%. Between April 26 and April 28 the measurement was interrupted due to a reactor shutdown.

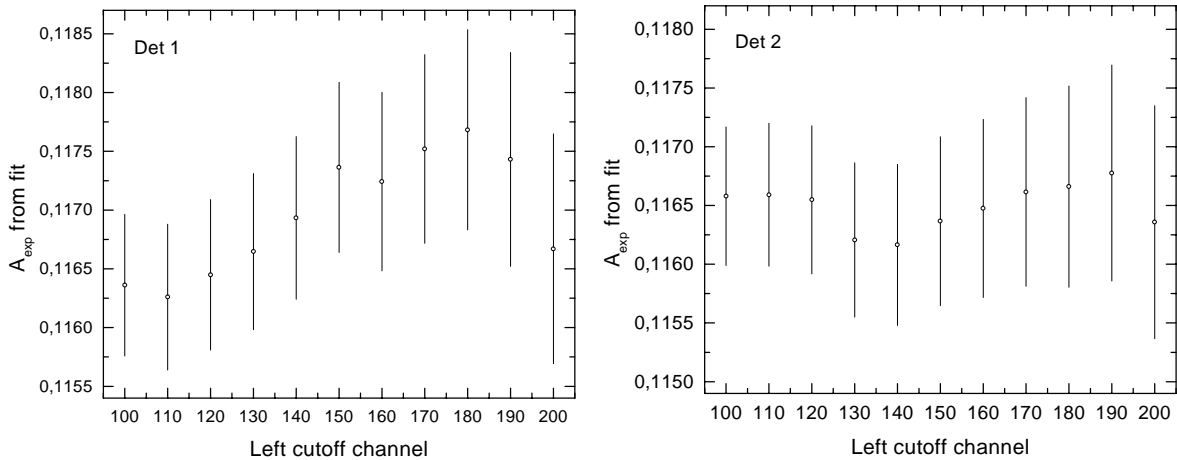


**Figure 4.16:** The values obtained for the raw correlation coefficient from the fits to the experimental asymmetries in different fit regions. The upper boundary is kept fixed at channel 300 while the lower cutoff is varied.

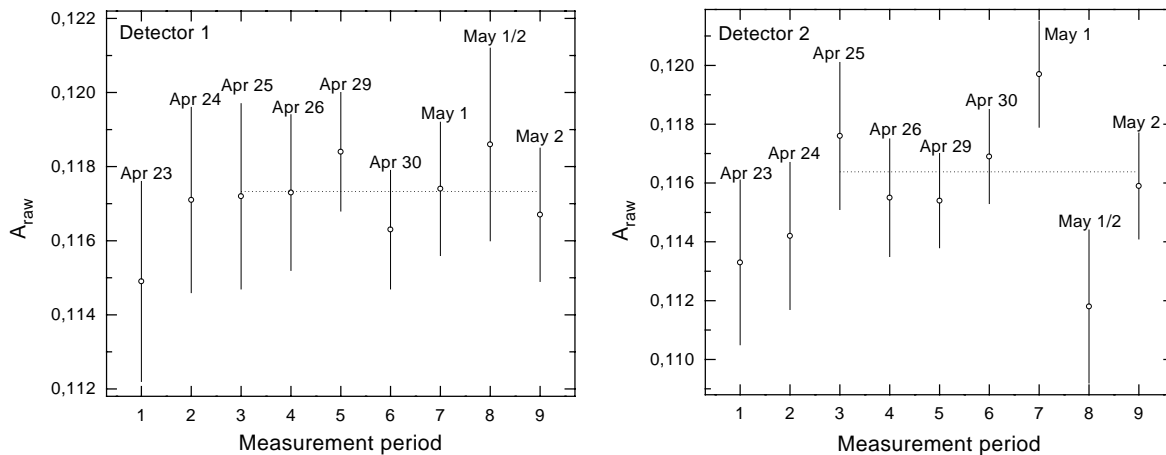


**Figure 4.17:** The values of the raw correlation coefficients obtained from the fits to different measurement periods corresponding to the given dates. Fits to the days used in the final analysis are shown as dotted lines.

### 4.3.3 Summary of systematic effects

In this section the systematic effects discussed so far are summarized and the corresponding corrections are applied. First, the corrections for the assignment to wrong hemispheres in the case of backscattering events, as discussed in Sections 3.4.1 and 3.4.2, are summarized in Table 4.4. After applying these corrections the raw asymmetries are:

$$A_{\text{raw},1} = 0.11768(76)$$

and

$$A_{\text{raw},2} = 0.11653(74),$$

leading to the average:

$$A_{\text{raw}} = 0.11709(53)$$

Effect	Detector 1	Detector 2
Time resolution	$(0 \pm 0.15)\%$	$(0 \pm 0.10)\%$
Threshold	$(0.23 \pm 0.12)\%$	$(0.17 \pm 0.12)\%$
<b>Sum</b>	<b><math>(0.23 \pm 0.19)\%</math></b>	<b><math>(0.17 \pm 0.16)\%</math></b>

**Table 4.4:** Corrections to the raw asymmetries in both detectors taking into account the misassignment of events to the wrong hemispheres due to backscattering (Sections 3.4.1 and 3.4.2).

The two raw asymmetries differ by almost one percent:

$$\delta = \frac{A_{\text{raw},1} - A_{\text{raw},2}}{\overline{A_{\text{raw}}}} = (0.98 \pm 0.91)\%. \quad (4.26)$$

While the difference is covered by the statistical uncertainty, there are also known effects that have to be taken into account when evaluating this difference. All the effects leading to different results in the two detectors are listed in Table 4.5. The last item is the variation in the neutron flux. The neutron flux was monitored using a detector close to the entrance in our beam tube, counting scattered neutrons. Over the beam time the variations in the flux were

not completely averaged out but led to a slightly different integral neutron flux for the two spin states. The effect was estimated in [Ast97] to yield a difference of 0.58% between the two detectors. The sum of the systematic effects increases the difference between the detectors but also adds a rather large systematic uncertainty. Altogether, the difference between the detectors is with  $1.5 \pm 1.1\%$  still tolerable. All the effects listed in Table 4.5 cancel to first order when the average of the two detectors is taken.

effect	$\delta$
Magnetic mirror	$\pm 0.6\%$
Long. Stern Gerlach	$-0.06\%$
Fit function	$\pm 0.03\%$
Neutron flux variation	$+0.58\%$
<b>Sum</b>	$\approx (\mathbf{0.52} \pm \mathbf{0.60})\%$

**Table 4.5:** Effects leading to a difference between the two detectors.

The corrections that have to be applied to the average raw asymmetry are summarized in Table 4.6. The corrections in parentheses are already included in the fit function and therefore already have been applied in the determination of  $A_{\text{raw}}$ .

Effect	Correction	Uncertainty
Polarization analysis		
polarization	1.1%	0.3%
flipper efficiency	0.3%	0.1%
Data set		
statistics		0.45%
background	(0.5%)	0.25%
Detector function		
linearity		0.2%
width & $E_0$ & pedestal		0.1%
drift		0.06%
edge effect	(-0.24%)	0.1%
Hemispheres		
mirror effect	0.09%	0.02%
Theory		
rad. corrections	0.09%	0.05%
<b>Sum</b>	<b>1.58%</b>	<b>0.66%</b>

**Table 4.6:** All the corrections and uncertainties entering the determination of  $A$ . The corrections shown in parentheses are already included in the fit function and thus do not enter in the sum of corrections that still have to be applied to  $A_{\text{raw}}$ .

In the sum only the remaining corrections are added. Applying this final correction of  $1.58\% \pm 0.66\%$  we obtain:

$$A = -0.11894(78) \quad \text{and} \quad \lambda = -1.2740(21),$$

using the standard model relation between  $A$  and  $\lambda$ , given in Eq.(2.27).

## 4.4 Comparison with other experiments

This result is the most precise determination of the angular correlation coefficient  $A$  so far. The value measured in the previous beamtime :  $A = -0.1189(12)$  [Abe97] was confirmed with improved accuracy. The results of existing measurements with an uncertainty of less than 2% in  $A$  are shown in Fig. 4.18. The earlier experiments all agree within their uncertainties. However, the two measurements with the PERKEO II spectrometer yield larger asymmetries. The deviation of the result described here from the weighted average of the three earlier experiments:  $A_{1-3} = -0.11465(90)$  is  $3.6\sigma$ . However, the PERKEO II spectrometer requires the smallest systematic corrections. In the original PERKEO experiment the magnetic field was aligned with the neutron beam leading to a large decay volume. However, this design led to a large magnetic mirror effect requiring a correction of 13% to the final result. The experiment in Erozolimskii's group measured electrons and protons in coincidence to suppress the back-

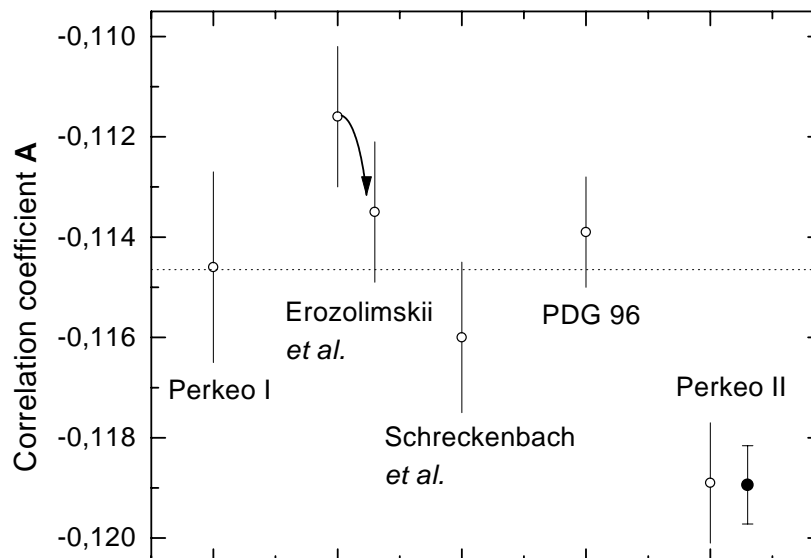


**Figure 4.18:** A comparison of precision measurements of  $A$ . The references are [Bop86] for the PERKEO I measurement, [Ero91] for the original value published by Erozolimskii *et al.*, that was corrected in [Yer97] to the value indicated by the arrow, and [Sch95] and [Lia97] for the Munich experiment in the group of Schreckenbach. The value of the particle data group in 1996 [PDG96] is an average not yet using the corrected value of Erozolimskii *et al.*, whereas the dashed line gives the weighted average of the earlier three experiments including the correction. The values indicated with PERKEO II are the results of the previous measurement [Bae96][Abe97] and the one described here.

ground. However, it suffered from a low and time dependent degree of polarization, making a correction of 21% to the final result necessary. The experiment in Schreckenbach's group used a combination of drift chambers and plastic scintillators. The plastic scintillators are used to give the start signal for the drift chambers and also to determine the electron energy. The background is suppressed by reconstructing the particle tracks in the drift chambers and requiring that they belong to electrons emitted in the decay volume. Here, one difficulty was the determination of the angle between electron and magnetic field, which was complicated by scattering in the gas. In the analysis an unexplained deviation from the expected cosine distribution was found. The authors claim that this is an artefact of the simulation and that the average angle is more robust and has small error bars. Also, as in the experiment in Erokolimskii's group, the backscattering of electrons leads to difficulties in the detector calibration and the determination of the energy dependence of  $A$ .

The major improvement in the PERKEO II over the PERKEO I experiment was to place the magnetic field perpendicular to the neutron beam. This way the correction for the magnetic mirror effect has been decreased by about two orders of magnitude and since this arrangement allows for a larger distance between the scintillators and the neutron beam, the background was also improved. With the further improvement in the background suppression achieved in this beam time, the largest remaining correction is the one of 1.1% for the polarizing efficiency. Thus the largest correction is an order of magnitude smaller than in the other experiments and is of the same order as the uncertainty.

## 4.5 Implications of the result

In combination with other results and assuming different models, the measurement of  $A$  can be used for different analyses. In the following section, the deduction of the coupling constants of the weak interaction is presented, where  $C_V$  is used for a unitarity test of the CKM matrix and  $C_A$  is used to check the Goldberger Treiman relation. At last a new limit on the mass of a hypothetical right handed W boson derived from neutron decay data is given.

### 4.5.1 Unitarity of the CKM matrix

In measuring  $A$  we determined  $\lambda$ , the ratio of axial to polar vector coupling constants. To obtain the individual coupling constants we have to use also the neutron lifetime. All the neutron lifetime measurements agree, leading to a weighted world average of  $\tau = 885.8(9)$  s [Abe98]. With this value for the neutron lifetime and our value for  $\lambda$  we obtain the effective individual coupling constants by using Eqs. (2.27) and (2.24):

$$C'_V = 1.1464(17) \times 10^{-5} \frac{(\hbar c)^3}{\text{GeV}^2} \quad (4.27)$$

$$C'_A = -1.4604(8) \times 10^{-5} \frac{(\hbar c)^3}{\text{GeV}^2}. \quad (4.28)$$

According to the conserved vector current hypothesis (CVC) the value of  $C_V$  is not changed by QCD effects in the nuclear medium. However, the value of  $C_A$  does depend on the medium

and therefore has to be measured. In principle, it can also be calculated by lattice gauge calculations. There the systematic uncertainties are estimated to be as large as 7 to 20 % [Don95]. On this level agreement with the measured value is found [Liu94]. Neutron decay thus offers the only possibility to determine  $C_A$  precisely.

The value of  $C_V$  can be used to determine the  $V_{ud}$  matrix element of the CKM matrix. In order to determine  $V_{ud}$  the inner radiative corrections  $\Delta_R^V$  have to be applied to the effective coupling constant  $C'_V$  (Section 2.5):

$$C_V'^2 = C_V^2(1 + \Delta_R^V) \quad \text{with} \quad \Delta_R^V = 2.40(8)\%. \quad (4.29)$$

Thus for the bare coupling we obtain  $C_V = 1.1329(16) \times 10^{-5} (\hbar c)^3 / \text{GeV}^2$  from which the  $V_{ud}$  matrix element is derived using the Fermi coupling constant  $G_F$  measured in muon decay:

$$V_{ud} = \frac{C_V}{G_F} = 0.9713(14) \quad \text{with} \quad G_F = 1.16639(1) \cdot 10^{-5} (\hbar c)^3 / \text{GeV}^2. \quad (4.30)$$

The traditional way to determine  $V_{ud}$  is to use nuclear beta decay where ( $J^\pi=0^+ \rightarrow 0^+$ ) transitions can proceed solely via Fermi transitions involving only the vector coupling constant.

$$Ft_{0^+ \rightarrow 0^+} = ft(1 + \delta_R)(1 - \delta_C) = \frac{K}{2C_V'^2}. \quad (4.31)$$

Here  $K$  is a combination of constants defined in Eq. (2.24),  $\delta_R$  contains radiative corrections accounting for the electromagnetic interaction between the charged particles involved in the decay, and  $\delta_C$  is a correction for isospin symmetry breaking, i.e. the interaction of the proton with the electromagnetic field of the nucleus. For these corrections one has to rely on calculations. In order to determine the  $ft$  value one has to measure the lifetimes, the endpoint energies, and the branching ratios of the decays. The corrected  $Ft_{0^+ \rightarrow 0^+}$  values of all decays should agree. This is a test of CVC, requiring that indeed  $C'_V$  is independent of the nuclear medium. However, this test relies on the reliability of the theoretical corrections. As for the values of the correction  $\delta_C$  inconsistent data have been published. The difficulty is that the nuclear wave functions, required to calculate  $\delta_C$ , strongly depend on the nuclear model used. Results of explicit calculations of the corrections are given for example by Towner and Hardy [Tow98]. There agreement is found between all transitions in support of the CVC hypothesis. Another approach, used by Wilkinson [Wil95], is to determine  $Ft$  values without including the correction  $\delta_C$  and then to extrapolate the values obtained from different decays to  $Z = 0$  where  $\delta_C = 0$ . This, however, assumes that  $\delta_C$  is a smooth function of  $Z$  that can be approximated with a second order polynomial expression. This assumption does not seem to be supported by the results from Towner and Hardy [Tow98]. A detailed discussion may be found in [Abe98].

From the  $Ft_{0^+ \rightarrow 0^+}$  values the effective coupling constant  $C'_V$  is obtained, Eq. (4.31). In order to obtain the nuclear  $V_{ud}$  values the same inner radiative correction  $\Delta_R^V$  as in neutron decay has to be applied. Two different evaluations came to similar results:

$$\begin{aligned} V_{ud}^{\text{TH}} &= 0.9740(5) && [\text{Tow98}] \\ V_{ud}^{\text{PDG}} &= 0.9740(10) && [\text{PDG98}] \end{aligned}$$

The first value  $V_{ud}^{\text{TH}}$  uses an average of two different evaluations of the  $\delta_C$  correction given in [Tow77] and [Orm95]. The second value, published by the particle data group, in addition

accounts for the Saito-Thomas correction [Sai95] leading to the larger uncertainty. The Saito-Thomas correction includes the effect of quark meson coupling inside the nucleons. However, it was calculated for an infinite nuclear medium rather than for finite nuclei and is still controversially discussed [Tow98].

While the experimental uncertainty in the determination of  $V_{ud}$  from neutron decay is (still) larger than from its determination from nuclear data, the advantage of neutron decay measurements is that the correction  $\delta_C$  and also a possible Saito-Thomas correction both vanish. The CKM matrix is a basis transformation and thus has to be unitary in order to conserve probability. The sum of the squared matrix elements in each row (and column) therefore has to yield one. This can be tested most precisely in the first row, with  $V_{ud}$  being the most important contribution:

$$|V_{ud}|^2 + |V_{us}|^2 + |V_{ub}|^2 = 1. \quad (4.32)$$

$V_{us}$  is determined most precisely from Kaon beta decay :

$$|V_{us}| = 0.2196(23) \quad [\text{PDG98}]. \quad (4.33)$$

The  $V_{ub}$  element is determined from semileptonic decays of  $B$  mesons:

$$|V_{ub}| = 0.0032(8) \quad [\text{PDG98}]. \quad (4.34)$$

Now the test of the unitarity condition can be done by comparing the  $V_{ud}$  values obtained from neutron and nuclear decay data to the  $V_{ud}$  value predicted by the unitarity condition

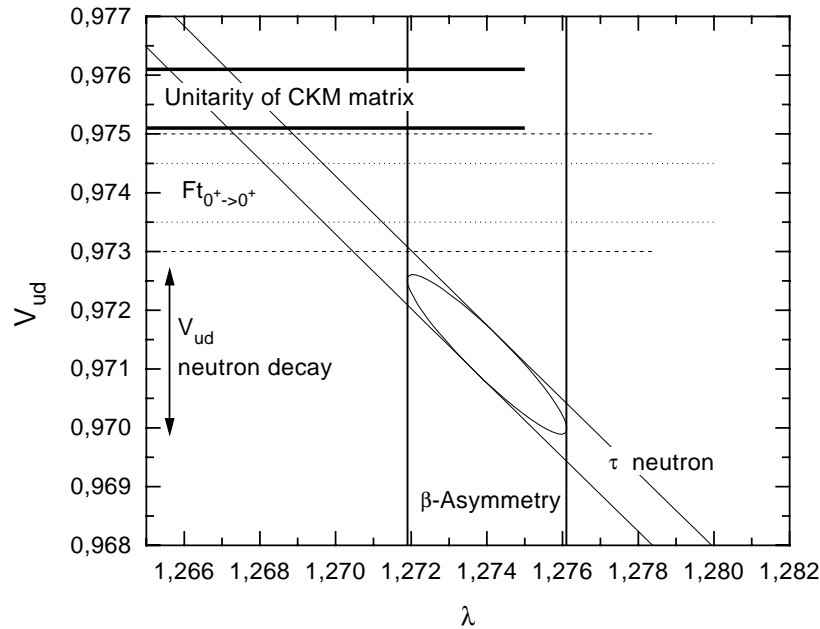


**Figure 4.19:** Comparison of  $V_{ud}$  values. The top one corresponds to the expected value of  $V_{ud}$  from the heavy quark matrix elements under the unitarity assumption. The two curves indicated with  $Ft_{0+ \rightarrow 0+}$  correspond to the two evaluations of nuclear beta decays discussed. The  $V_{ud}$  value derived from neutron decay is indicated by the arrows.

using the given values for  $V_{us}$  and  $V_{ub}$ . The results are:

$$\begin{aligned} 1 - |V_{ud}|^2 - |V_{us}|^2 - |V_{ub}|^2 &= 0.0083(29) && \text{from neutron decay} \\ 1 - |V_{ud}|^2 - |V_{us}|^2 - |V_{ub}|^2 &= 0.0031(14) && \text{from nuclear decay [Tow98]} \\ 1 - |V_{ud}|^2 - |V_{us}|^2 - |V_{ub}|^2 &= 0.0031(21) && \text{from nuclear decay [PDG98]} \end{aligned}$$

Thus in all cases the sums of the matrix elements squared is smaller than one. The violation of the unitarity condition is largest (about  $3\sigma$ ) using the  $A$  measurement of this thesis. However, only by inflating the uncertainty due to the Saito-Thomas correction it is kept below  $2\sigma$  in the analysis of the particle data group. These results are visualised in Figure 4.19, showing the contributions from the measurements of the correlation coefficient  $A$  and the lifetime  $\tau$  to the determination of  $V_{ud}$  in neutron decay. Explanations, besides experimental and/or theoretical errors, require physics beyond the standard model. One possibility is a fourth quark generation, which would lead to the CKM matrix having to be extended to a  $4 \times 4$  matrix. The mass limit for a quark of the fourth generation from collider experiments is  $m \geq 85 \text{ GeV}$  [Abe92]. Another possibility is a left-right symmetric extension of the standard model. In such a framework the value of  $V_{ud}$  would be calculated differently. The deviation  $\Delta$  from the unitarity condition leads to the prediction  $\zeta = 1/2\Delta$  for the mixing angle  $\zeta$  in such a model [Tow95], where  $\Delta = 0.0083(29)$  would be the appropriate value from neutron decay data. This is well within the limits on left-right symmetric models that will be discussed in Section 4.5.3.

Another independent way to determine  $V_{ud}$  is to use pion beta decay:

$$\pi^+ \longrightarrow \pi^0 + e^+ + \nu_e .$$

With the value of  $V_{ud}$  obtained there, the sum of the squared matrix elements is again smaller than one:

$$1 - |V_{ud}|^2 - |V_{us}|^2 - |V_{ub}|^2 = 0.0167(311) \quad [\text{Tow98}] .$$

However, it is in agreement with the unitarity condition within the comparatively large uncertainty. The uncertainty is mainly due to the difficulty of measuring the small branching ratio of this decay mode:

$$\text{BR} = (1.025 \pm 0.034) \times 10^{-8} \quad [\text{McF85}] .$$

A new measurement aiming at reducing the uncertainty in this branching ratio by a factor of eight is planned at the Paul Scherrer institute.

### 4.5.2 Goldberger Treiman relation

As discussed in Section 2.3 the Goldberger Treiman relation connects the pion decay constant  $f_\pi$  and the pion nucleon coupling constant  $g_{\pi NN}$  to  $C_A$  and the nucleon masses:

$$f_\pi g_{\pi NN} \approx C_A \frac{m_n + m_p}{2} . \quad (4.35)$$

Recent evaluations of the pion nucleon coupling constant, as given in Table 4.7, are not consistent. Using our value for  $\lambda = 1.2743(21)$  and:

$$\begin{aligned}\frac{m_n + m_p}{2} &= 938.92\text{MeV} \\ \sqrt{2}f_\pi &= 130.70(10)(36)\text{MeV}\end{aligned}$$

as given in [PDG98], the Goldberger Treiman relation leads to  $g_{\pi NN} = 12.95(5)$  thus showing a preference for the smaller values of  $g_{\pi NN}$  in Table 4.7. However, the given range of values for the pion nucleon coupling constant leads to:

$$\Delta = 1 - \frac{C_A(m_n + m_p)}{2f_\pi g_{\pi NN}} = 0.4\% \text{ to } 4.1\%. \quad (4.36)$$

The correction  $\Delta$  to the Goldberger Treiman relation is a measure of the chiral symmetry breaking in the strong interaction [Pag75]. Yet, the possible range implied by the different values for  $g_{\pi NN}$ , is too large to discriminate between different theoretical predictions.

$g_{\pi NN}$	source
13.36(8)	1999, [Eri99]
13.51(12)	1998, [Rah98]
13.14(4)	1998, [Arn99]
13.04(2)	1997, [new97a]
13.00(7)	1997, [new97b]

**Table 4.7:** Recently published values for the pion nucleon coupling constant.

### 4.5.3 Right handed currents

In the standard model parity violation is introduced by placing the lefthanded particles in doublets subjecting them to SU(2) gauge transformations. The right handed particles are singlets under this transformation and therefore do not participate in the weak interaction. From a fundamental theory one would expect an explanation of the origin of parity violation. In left right symmetric models the fundamental theory is parity invariant, and parity violation is a consequence of spontaneous symmetry breaking. In so-called manifest left right symmetric models the left and right handed weak coupling constants are the same, as are the left and right handed CKM matrices. The parity violation is then a consequence of the  $W$  bosons mediating the right handed interaction being much heavier than the ones responsible for the left handed interaction.

In this model the weak interaction eigenstates  $W_L$  and  $W_R$  of the  $W$  bosons are a linear combination of the mass eigenstates :

$$W_L = W_1 \cos(\zeta) - W_2 \sin(\zeta) \quad (4.37)$$

$$W_R = W_1 \sin(\zeta) + W_2 \cos(\zeta) \quad (4.38)$$

There are three free parameters:  $\lambda = C_A/C_V$ , the ratio of coupling constants that may be different from the one in the standard model,  $\zeta$ , the mixing angle, and  $\delta = m_1^2/m_2^2$  the squared

ratio of the  $W$  boson masses. From a measurement of  $A$  one can no longer deduce  $\lambda$  since  $A$  now depends on the other parameters as well. In our analysis we use our value for  $A$ ,  $B = 0.9824(40)$ ,  $\tau_{\text{neutron}} = 885.8(9)$  s and  $Ft_{0^+ \rightarrow 0^+} = 3074.8 \pm 2.2$  s (all values derived as world averages in [Abe98]). The resulting exclusion plots in the  $\delta - \zeta$  plane are shown in Fig. 4.20. The standard model ( $\delta = 0, \zeta = 0$ ) lies within the allowed region at 90% confidence level. In the beginning of 1996 the standard model was still excluded with over  $2\sigma$ .

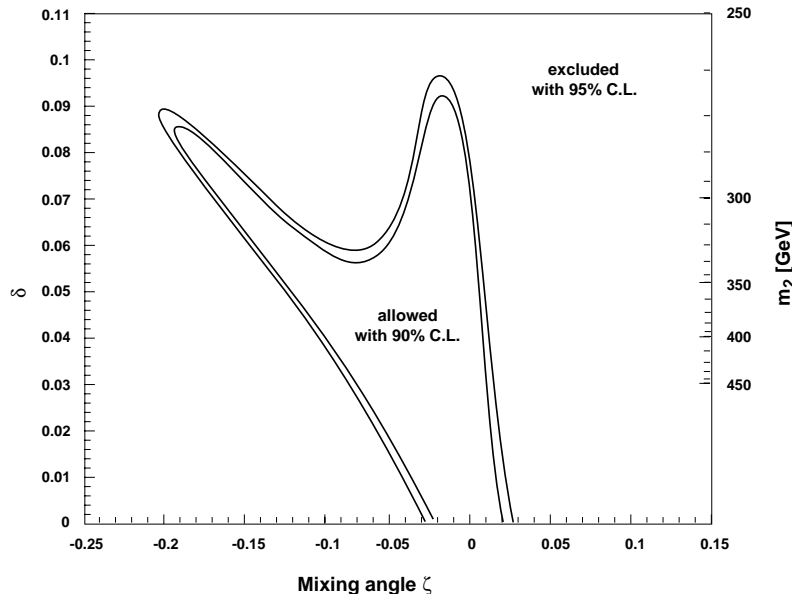


**Figure 4.20:** Exclusion curves in the  $\delta - \zeta$  plane of a manifest left right symmetric model. The contours give the allowed regions with 90% and 95% confidence level. The standard model point  $\delta = 0$  and  $\zeta = 0$  lies within the allowed region.

The improved uncertainty in the  $A$  measurement is reflected in the limits for the mixing angle  $\zeta$ , which is between  $-0.19$  and  $0.01$  (at 90% confidence level). The  $\beta$ -asymmetry is not particularly sensitive to the mass of the  $W_2$  - there the lower limit of  $265$  GeV (at 90% C.L.) is the same as found in [Bae96] in spite of the recent  $B$  measurement [Ser98]. In this respect a measurement of the neutrino asymmetry is more interesting.

However, other approaches yield more stringent limits on the mass of the  $W_2$ . The limits from collider experiments, where a new charged  $W'$  boson is searched, yield lower limits for the mass of  $m_{W'} \geq 652$  GeV [Abe95] and  $m_{W'} \geq 720$  GeV [Aba96], both at 95% C.L. This result, however, is valid for  $\zeta = 0$  only. If the neutrino is a Majorana particle, a right handed interaction would lead to neutrinoless double beta decay. Since this is not observed, limits on the left right symmetric model can be derived. Namely for a mass of the right handed neutrino  $m_{\nu_R} \leq 1$  TeV the lower limit for the mass of  $W_2$  is  $m_{W_2} \geq 1.1$  TeV for any mixing angle [Hir96].



# Chapter 5

## Preparations for the $B$ measurement

### 5.1 The measurement principle

The next goal for the Perkeo experiment is to measure the neutrino asymmetry in neutron decay. Therefore we have to detect the recoiling protons in coincidence with the electrons. Using the Perkeo spectrometer there are two possibilities. Either we detect the protons in the same or in the opposite hemisphere as the electrons. Detecting them in the same hemisphere is the more systematically clean choice. When the electron and the proton are emitted in the same hemisphere, the neutrino must have been emitted in the opposite hemisphere to conserve momentum independent of the electron energy. In order to illustrate this point, we define two experimental asymmetries corresponding to the two configurations as:

$$\alpha_1 = \frac{N^{\downarrow\downarrow} - N^{\uparrow\uparrow}}{N^{\downarrow\downarrow} + N^{\uparrow\uparrow}} \quad (5.1)$$

$$\alpha_2 = \frac{N^{\uparrow\downarrow} - N^{\downarrow\uparrow}}{N^{\uparrow\downarrow} + N^{\downarrow\uparrow}} \quad (5.2)$$

Where the arrows indicate the direction of electron and proton emission with respect to the neutron spin.

In Fig. 5.1 the two asymmetries are shown as a function of electron energy. Indeed the experimental asymmetry  $\alpha_1$ , detecting electron and proton in the same hemisphere, has the smaller dependence on the electron energy. The sensitivity to  $B$  is higher in this case as well [Rei91][Glü95]. Using this scheme gives a specific advantage to the Perkeo spectrometer as opposed to other experiments, allowing for a systematically clean experiment. This choice, however, leads to the challenge of having to detect the very low energetic protons in the same detector as the electrons. This can not be achieved with proton detectors used in other neutron decay studies, i.e. surface barrier detectors, PiN diodes, and multi channel plates, since these detectors are not available in sufficient sizes and/or have a rather low detection efficiency for the electrons.

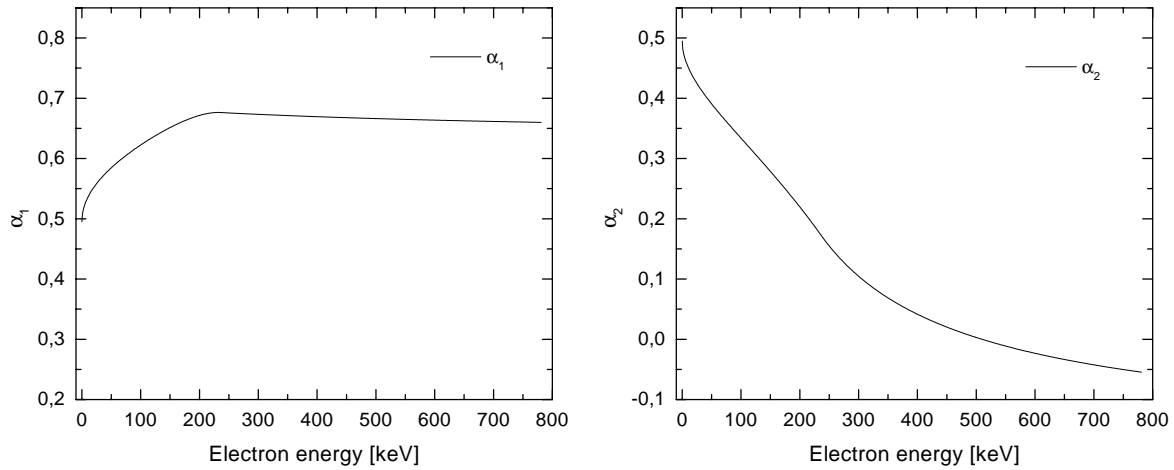


**Figure 5.1:** The two possible e,p asymmetries in Perkeo.

We want to use a method described in [Dob75] and [Str78] to detect the protons. The idea is to accelerate the protons onto a thin foil by applying a potential of about 20 keV to the foil. When crossing the foil the protons produce secondary electrons which are in turn accelerated by the same field onto the plastic scintillator where they are detected. On the other hand, the primary electrons of the decay lose only very little energy passing through the foil. Thus the protons will be detected in delayed coincidence with the electrons. A schematic of this method is shown in Fig. 5.2.

With an average of four secondary electrons produced one would obtain a signal corresponding

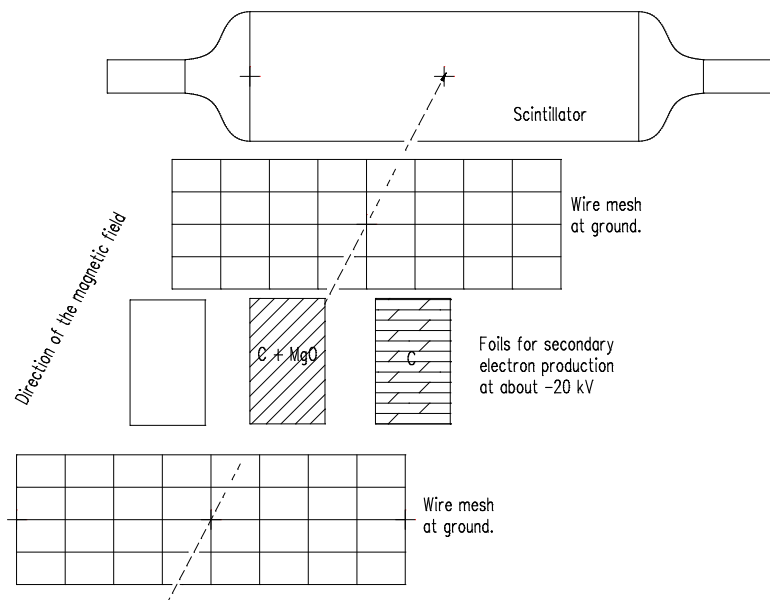


**Figure 5.2:** A schematic of the proton detection. Two wire meshes define ground potential. The protons from neutron decay are accelerated onto the foils on high voltage. The emitted secondary electrons from the foils are in turn accelerated onto the plastic scintillator.

to 80 keV in the detector. This would already be above the threshold of our detectors in the last beam time. However, since the number of secondary electrons will be statistically distributed we will need to improve the light collection efficiency to lower the thresholds while at the same time try to obtain as many secondary electrons as possible. The foils should be made as large as possible to obtain high statistics and to avoid edge effects, currently we plan on a foil size of  $12 \times 9 \text{ cm}^2$ . In the following sections systematic effects of this scheme, the detector design, and results of test measurements are discussed.

## 5.2 Statistical sensitivity

Using a Monte Carlo routine to model the neutron decay, the experimental asymmetries were simulated. The analytical expressions for the two asymmetries were derived by F. Glück [Glü95]. Assuming no Fierz interference and 100% polarization of the neutrons the expression for  $\alpha_1$  is given by:

$$\alpha_1[r < 1] = \frac{B(1 - \frac{1}{3}r^2) - A\beta(1 - \frac{2}{3}r)}{2 - r + \frac{1}{2}a\beta(\frac{1}{2}r^2 - 1)} \quad (5.3)$$

$$\alpha_1[r > 1] = \frac{\frac{2}{3}B - \frac{1}{3r}A\beta}{1 - \frac{1}{4r}a\beta} \approx \frac{2}{3}B - \frac{1}{3r}\beta \left( A - \frac{B \cdot a}{2} \right) \quad (5.4)$$

$$\text{with } r = \beta \frac{E_e}{E_\nu} = \frac{p_e}{p_\nu}.$$

Here  $a$ ,  $A$ , and  $B$  are the angular correlation coefficients defined in Eq. (2.25),  $E_\nu$ ,  $E_e$  the neutrino and total electron energy respectively and  $\beta$  the electron velocity in units of the speed of light. In the given approximation the proportionality to  $B$  becomes clear for  $r > 1$ <sup>1</sup>. In Fig. 5.3 the asymmetries for different values of  $B$  are plotted to show this proportionality.

The analytical function, Eq. 5.3, was incorporated into our fitting program. In Fig. 5.4 simulated data and a fit are shown. The sensitivity to  $B$  was found to be:  $\Delta B/B = 2.6/\sqrt{N}$ , where  $N$  refers to the total number of neutron decays in the spectrometer, confirming the result already obtained in [Glü95]. This sensitivity was calculated using all electron energies and assuming to have two proton detectors on both sides of the neutron beam. In practice one will use only part of the electron spectrum. For very low energies the potential of the foils becomes a concern (Section 5.3.5) and for high energies the magnetic mirror effect becomes large (Section 5.3.2). Using only electron energies between 200 and 400 keV the statistical sensitivity to  $B$  is  $\Delta B/B = 4/\sqrt{N}$ . Thus to obtain a statistical uncertainty of  $\Delta B/B = 0.1\%$  we need  $1.6 \cdot 10^7$  events. With 5 days as a maximum amount of pure measuring time this leads to a minimum neutron decay rate of only:

$$N_0 = \frac{1.6 \cdot 10^7}{5 \cdot 24 \cdot 3600} \cdot 2 \approx 75 \text{ Hz} \quad (5.5)$$

---

<sup>1</sup>Using realistic values for the beam polarization  $P$  and the spin flip efficiency  $f$  the approximation has to be modified only slightly leading to:  $Pf \cdot \{2/3B(1 + 2/3B \cdot P(1 - f)) - \beta/3r(A - Ba/2)\}$ . Furthermore, it should be noted that the function is differentiable also at the point  $r = 1$ , corresponding to  $E_{e,\text{kin}} \approx 236 \text{ keV}$ .

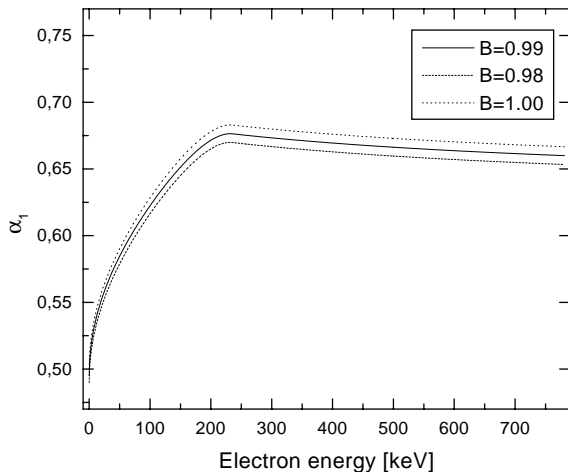


**Figure 5.3:** The experimental asymmetry  $\alpha_1$  for changes of  $B$  by 1%.

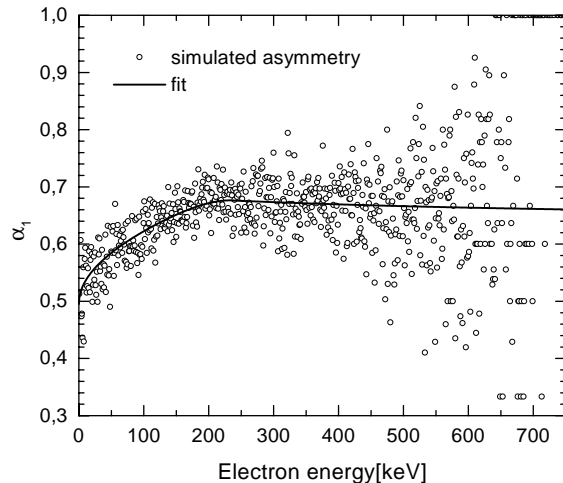


**Figure 5.4:** Fit to the simulated asymmetry  $\alpha_1$ .

The factor of 2 enters assuming that we will only have one proton detector. In order to be able to do also a variety of systematic checks a decay rate in the range of 100 to 150 Hz is desirable. The most precise measurement of  $B$  to date [Ser98] had a count rate of 0.6 Hz reaching a statistical uncertainty of 0.25%. The other important contributions to the uncertainty of their final result of  $B = 0.9801(46)$  were the uncertainty in the polarization of the beam (0.25% in  $B$ ) and the energy resolution of their electron detector (0.2% in  $B$ ). With our measurement scheme not being sensitive to the exact electron energy and a polarization analysis using  $^3\text{He}$  spin filters significant improvements in these points can be expected from our measurement.

## 5.3 Systematic effects

### 5.3.1 Proton time of flight

Another question addressed with the MC program was the time of flight of the protons. Their time of flight is dominated by the time they spend in the region close to the neutron beam where the magnetic field is still nearly homogeneous and the electric field is zero. The time of flight  $t$  over a distance  $d$  parallel to a constant magnetic field can be calculated from the proton energy and the angle of emission  $\theta_0$  with respect to the magnetic field according to:  $t = d/(v \cos \theta)$ , where  $v$  refers to the proton velocity. The time of flight spectra thus calculated for the two neutron spin states are shown in Fig. 5.5. The important point to note is that the time of flight spectra are significantly different for the two neutron spin states.

The problem is caused primarily by protons emitted at close to  $90^\circ$  to the magnetic field since there the time of flight diverges. In practice, however, due to the decreasing magnetic field this situation is significantly improved. A decrease in magnetic field strength from 100% to 99% is sufficient to change an emission angle of  $90^\circ$  to  $84^\circ$ . In a more detailed calculation the

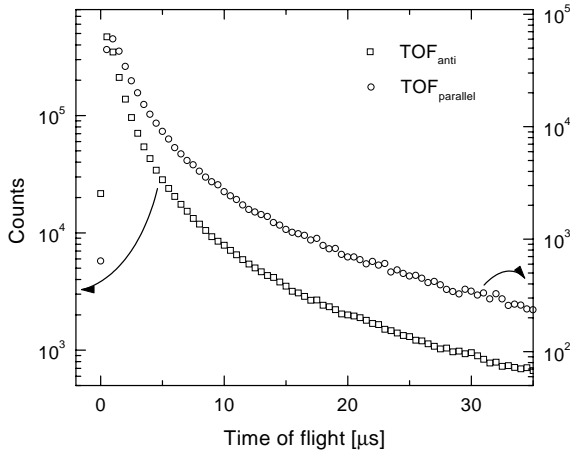


**Figure 5.5:** Proton time of flight spectra for the two different spin states over a distance of 10 cm not taking into account the decrease of the magnetic field.

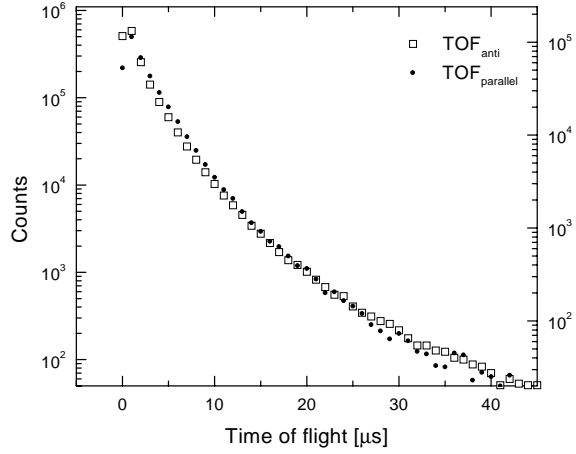


**Figure 5.6:** The same spectra now taking into account the magnetic field gradient.

magnetic field gradient was taken into account. In the beam time the magnetic field was measured at various points in the decay volume, an example of a scan along the magnetic field direction, is shown in Fig. 5.7. In a region of at least 10 cm across the neutron beam the magnetic field strength can be described by a quadratic approximation:

$$B(x) = B_0 \left( 1 - \left( \frac{x}{l} \right)^2 \right), \quad (5.6)$$

where the  $x$ -direction is parallel to the magnetic field.

The parameter  $l$  was found to vary between 74 and 80 cm over the decay volume, with  $l$  decreasing towards the center. Using Eq.(5.6) the time of flight  $t$  for a proton emitted from some position  $x_0$  until it reaches a distance  $d$  from the center can be calculated analytically to be:

$$t(x_0, d, v, \theta_0) = \frac{d_{\text{eff}}(x_0, d, \theta_0)}{v} \quad (5.7)$$

$$d_{\text{eff}}(x_0, d, \theta_0) = \frac{l}{a} \ln \left( \frac{\frac{ad}{l} + \sqrt{1 - a^2 + \left( \frac{ad}{l} \right)^2}}{\left| \frac{ax_0}{l} + \cos \theta_0 \right|} \right) \quad \text{with} \quad (5.8)$$

$$a = \frac{\sin \theta_0}{\sqrt{1 - \left( \frac{x_0}{l} \right)^2}}, \quad (5.9)$$

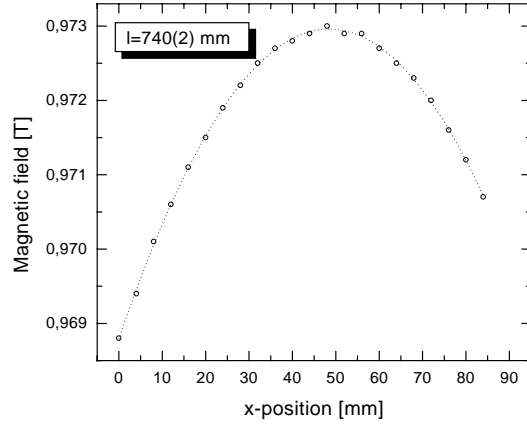


**Figure 5.7:** An example of the magnetic field measured in the decay volume, with the  $x$ -direction along the magnetic field. The maximum of the field is aligned with the neutron beam. The field is well described by Equation 5.6. From the fit to the magnetic field  $l = 740(2)$  mm has been extracted.

where again  $v$  is the velocity of the proton and  $\theta_0$  is the initial angle between the proton momentum and the magnetic field. In the limit that the proton is emitted parallel to the magnetic field:

$$d_{\text{eff}} \rightarrow d. \quad (5.10)$$

With this equation for the time of flight the MC was repeated. The resulting spectra for the two spin states are shown in Fig. 5.6. The tails corresponding to long times are strongly suppressed as expected. Still the spectra are somewhat different, though.

Fig. 5.8 shows the proton detection efficiencies depending on the length of the coincidence window obtained by integrating the time of flight spectra. For coincidence times larger than  $26 \mu\text{s}$  the difference is less than 0.1%. The systematic change in the value for  $B$  obtained is shown in Fig. 5.9. For coincidence times of about  $30 \mu\text{s}$  or more the effect on  $B$  is smaller than 0.05%. Therefore the coincidence time window must be made at least that long. The width of the neutron beam does not significantly change this estimate as was found by varying it in the MC. The increase of events with long time of flight due to protons emitted from the side of the neutron beam opposite the proton detector is cancelled by protons being emitted on the same side as the proton detector.

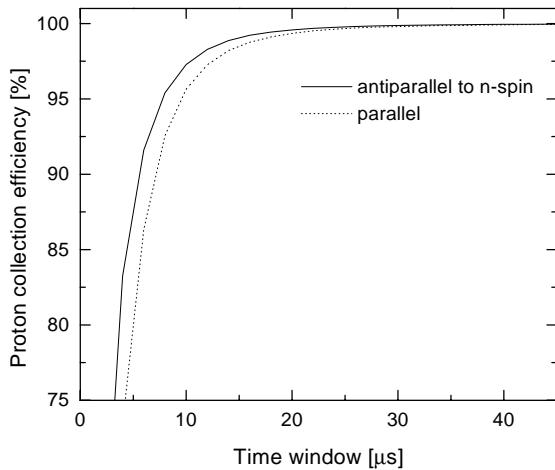


**Figure 5.8:** Fraction of protons arriving in a time window for the two spin states. The efficiency is calculated by integrating the curves in fig. 5.6.

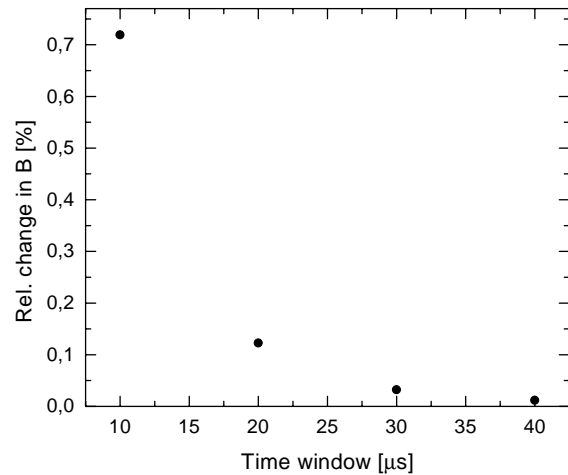


**Figure 5.9:** The effect of the protons missed due to a limited length of the time window on the determination of  $B$ .

An estimate for the minimum time of flight is required as well. When electron and proton are emitted into the same hemisphere, the maximum longitudinal energy (parallel to the magnetic field) the proton can have is 324 eV. Therefore its maximum longitudinal velocity is about  $25 \text{ cm}/\mu\text{s}$ . Assuming a distance of 10 cm without electric field and another 20 cm with a constant electric field of 1 kV/cm the time of flight is:

$$\Delta t \approx 400 \text{ ns} + 200 \text{ ns} = 600 \text{ ns}. \quad (5.11)$$

The time the secondary electrons need to reach the scintillator is negligible in this estimate. On the other hand, the maximum time of flight between the two scintillators is about 60 ns for

the primary electrons from neutron decay as can be seen from Fig. 3.4.1. Thus, the electrons and protons will be easily resolved. This estimate also justifies why in the above calculations the proton time of flight was only evaluated to a distance  $d = 10$  cm from the beam center where the electric field was assumed to set in. The additional time of about 200 ns spent in the electric field will not change the estimated  $30 \mu\text{s}$  time window required.

### 5.3.2 Magnetic mirror effect

The magnetic mirror effect has not been included in the analysis of the time of flight. With the given approximation for the magnetic field, Eq. (5.6), the condition for a proton to be reflected, Eq. (3.4), translates into:

$$a = \frac{\sin \theta_0}{\sqrt{1 - \left(\frac{x_0}{l}\right)^2}} > 1. \quad (5.12)$$

These events have been discarded in the simulation of the time of flight spectra. However, the occurrences were counted. The magnetic mirror probabilities, averaged over the neutron spin states, were found to be 1.85% and 3.6% for beam widths of 4 and 8 cm respectively assuming  $l = 75$  cm for the magnetic field. In order to calculate the effect on the determination of  $B$ , the magnetic mirror probability for the electrons has to be taken into account as well. The condition for the electron to be reflected is the same as for the proton. In another MC calculation experimental asymmetries  $\alpha_1$  were simulated including the magnetic mirror effect, considering all possible combinations that lead to electron and proton ending up in the same hemisphere. The result was that the sensitivity of the asymmetry  $\alpha_1$  to the magnetic mirror effect increases strongly for high electron energies. An example for such a spectrum is shown in Fig. 5.10.

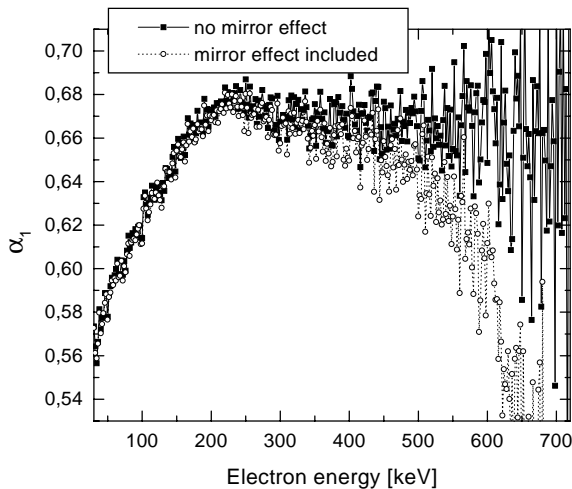


**Figure 5.10:** The magnetic mirror effect significantly decreases the asymmetry  $\alpha_1$  at large electron energies. The shown simulation assumes  $l = 75$  cm and a width of the neutron beam of 8 cm.

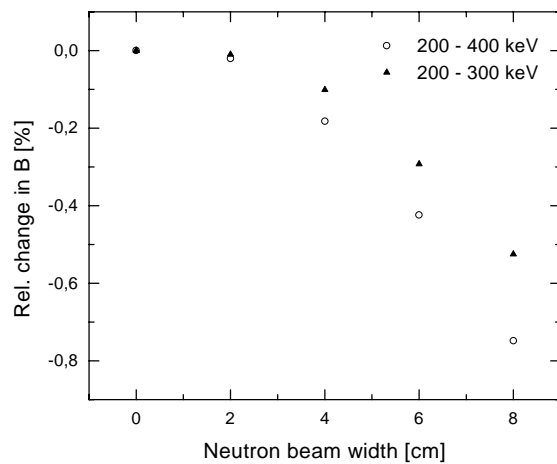


**Figure 5.11:** The relative change of  $B$  due to the magnetic mirror effect depending on the width of the neutron beam and on the energy region analysed.

The reason for this energy dependence can be understood from momentum conservation. Since the neutrino is (nearly) massless and the proton very massive compared to the leptons, it follows that the neutrino momentum is related to the electron energy by:

$$p_\nu = \Delta - m_e - E_e, \quad (5.13)$$

where  $\Delta = 1.29 \text{ MeV}$  is the mass difference between neutron and proton.

Thus for electron energies larger than  $E_e > 235 \text{ keV}$  ( $p_e > 544 \text{ keV}$ ) the electron momentum is larger than the neutrino momentum. In these cases a minimum angle between electron momentum and magnetic field direction is required, in order for the proton to have the possibility to be emitted into the same hemisphere as the electron. This is shown in Fig. 5.12. For a given electron momentum the circle indicates the possible directions of the neutrino momentum. The case shown, with the electron momentum component in the direction of the magnetic field being equal to the total neutrino momentum, corresponds to the minimum angle between electron momentum and magnetic field. For smaller angles, electron and proton will always be emitted into opposite hemispheres. For larger angles, the probability that electron and proton are emitted into the same hemisphere increases. The minimum angle, given by  $\theta_{\min} = 90^\circ - \arcsin(p_\nu/p_e)$ , increases with electron energy. Therefore, the higher the electron energy the larger are the required angles between electron momentum and magnetic field, leading to an increasing magnetic mirror effect.

The dependence of the value of  $B$  obtained from these asymmetries on the size of the neutron beam and on the energy region analysed is shown in in Fig. 5.11. The effect is decreased by making the beam more narrow and by lowering the upper energy limit in the analysis. In both cases statistics is lost. Analysing only the region of 200 to 300 keV the statistical sensitivity would be  $\Delta B/B = 5/\sqrt{N}$ . The effect of a misalignment of the neutron beam center and the maximum of the magnetic field has not been examined, yet. It is to be expected that an averaging over two detectors on either side of the beam is required as in the case of the electron asymmetry. Therefore, even if only one proton detector will be used, it will be necessary to take data with the detector placed on either side of the beam.

### 5.3.3 Accidental coincidences

The large coincidence time window of about  $30 \mu\text{s}$ , required to efficiently collect the protons, leads to a large number of accidental coincidences obtained. The lowest rate of true events is obtained when proton and electron are detected in the hemisphere parallel to the neutron spin:

$$N_{\text{true}}^{\uparrow\uparrow} = x \cdot N_0, \quad (5.14)$$

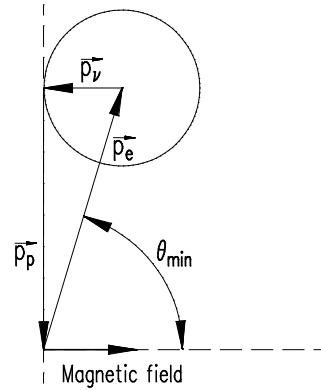


**Figure 5.12:** The minimum detected angle between electron momentum and magnetic field direction is shown. For smaller angles, the proton and the electron will always be emitted in opposite hemispheres.

where  $N_0$  is the rate of neutron decays inside the decay volume and  $x \approx 3.9\%$  is the probability for the electron and the proton to be emitted both in the hemisphere parallel to the neutron spin. The total rate in the detector can be written as the sum of electron, proton and background events:

$$N = N_e + N_p + N_{\text{back}} = f \cdot N_0 + N_{\text{back}}, \quad (5.15)$$

where  $f \approx 86\%$  is the sum of the probabilities for the electron and proton individually to be emitted parallel to the neutron spin. The values of  $x$  and  $f$  were obtained from MC calculations. The rate of accidentals  $N_{\text{acc}}^{\uparrow\uparrow}$  within a coincidence time  $\tau$  is (in a linear approximation) given by  $N^2 \times \tau$  and the ratio of accidental to true events  $R$  is then:

$$R = \frac{N_{\text{acc}}^{\uparrow\uparrow}}{N_{\text{true}}^{\uparrow\uparrow}} = \frac{(f \cdot N_0 + N_{\text{back}})^2 \tau}{x \cdot N_0}. \quad (5.16)$$

Thus the rate of background counts, leading to a certain accidentals to true signal ratio, can be calculated depending on the rate of neutron decays  $N_0$  in the spectrometer, using the given values for  $x$ ,  $f$ , and  $\tau = 30 \mu\text{s}$ . The result is shown in Fig. 5.13. Assuming a reasonable decay rate of  $N_0 \approx 100 \text{ Hz}$ , a background rate of about 80 Hz already leads to a fraction of about 20% accidental coincidences. Thus it is crucial to minimize the background. In any case the correction for accidental counts will have to be done. They can be measured by the delayed coincidence technique and by making the time of flight window long enough to measure the asymptotic value.

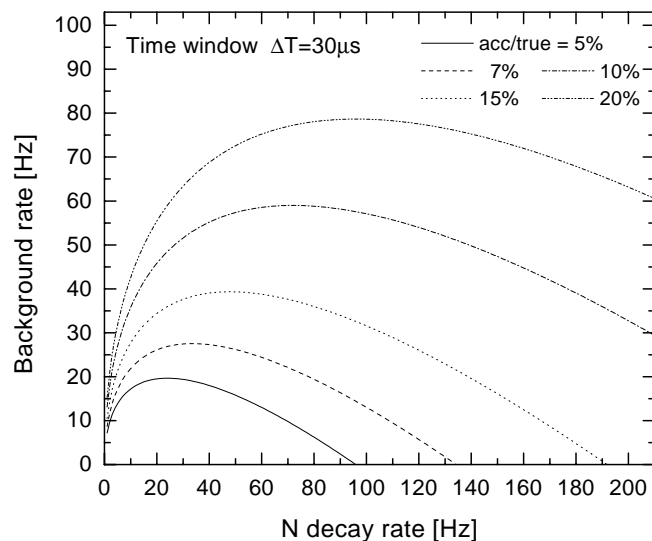


**Figure 5.13:** The relation between the neutron decay rate, the background rate and the obtained accidentals/signal ratio for a given time window.

### 5.3.4 The potential of the neutron beam

In Fig. 5.2 a mesh on zero potential is shown to define the potential of the neutron beam. Using the MAFIA program the electric field was calculated. It was found that with just one grid the potential in the region of the neutron beam is still about  $-100$  V and changes by as much as  $40$  V across the neutron beam. Thus all protons with a longitudinal energy of less than  $100$  eV would be directed onto the proton detector, independent of the hemisphere into which they had been emitted. The potential of the neutron beam has to be better defined for a  $B$  measurement.

The sensitivity of the measurement to the neutron beam not being on zero potential has also been simulated by a MC calculation. It was assumed that all protons emitted with a longitudinal energy of less than  $E = e\Phi$  are detected in the proton detector independent of their angle of emission. This corresponds to a situation where the potential in the decay volume is uniform, its magnitude is  $\Phi$ , and outside the neutron beam the potential is zero before the magnetic field gradient bends the proton momenta forward. The result, Fig. 5.14, was that the potential in the decay volume has to be smaller than  $\Phi \approx 1$  mV to insure that the effect on  $B$  is less than  $0.2\%$ . This estimate is conservative since the largest contribution to the effect is due to protons emitted at close to  $90^\circ$  to the neutron spin. For these cases even the small magnetic field gradient in the decay volume will significantly improve the situation. However, to include the effect of the magnetic field, maps of both the electric and the magnetic fields with their relative positioning are required.

Different electric field configurations were calculated using the MAFIA program with the goal of finding a configuration that leads to a potential of less than  $1$  mV in the region of the neutron beam. The result from a calculation yielding a sufficient suppression of the electric field is shown in Figs. 5.15 and 5.16. In the decay volume the maximum absolute value of the potential obtained is less than  $0.3$  meV. In this calculation a grounded box was placed

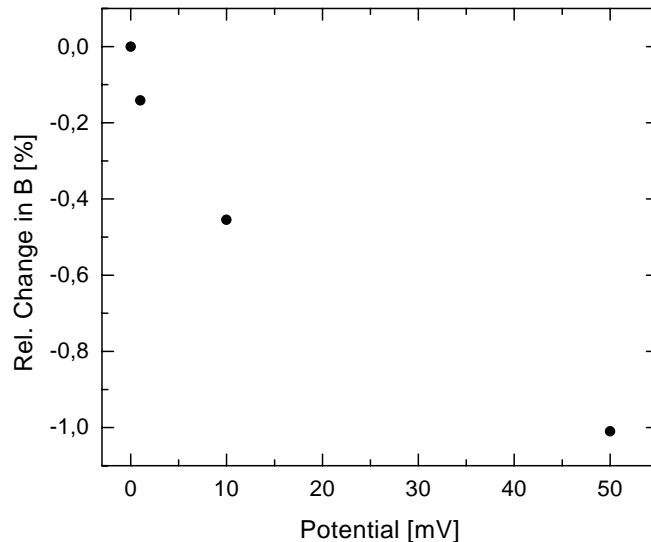


**Figure 5.14:** The sensitivity of  $B$  to the potential in the decay volume. The high sensitivity is due to the  $\sin(\theta)$  factor in the phase space leading to most protons being emitted nearly vertical to the neutron spin.

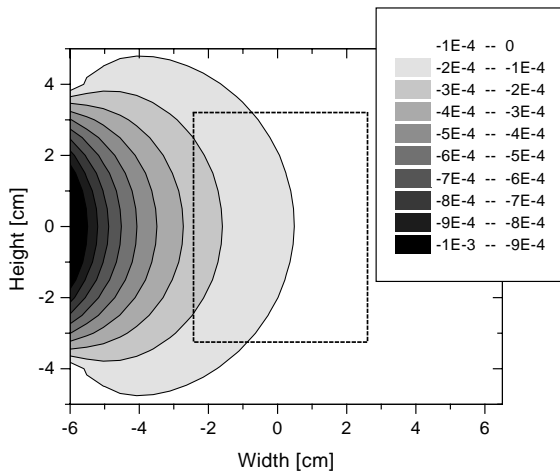


**Figure 5.15:** The potential in Volt over the cross section of the central detector region. The dashed line indicates the decay volume. The maximum potential encountered by the neutrons is less than 0.3 mV.

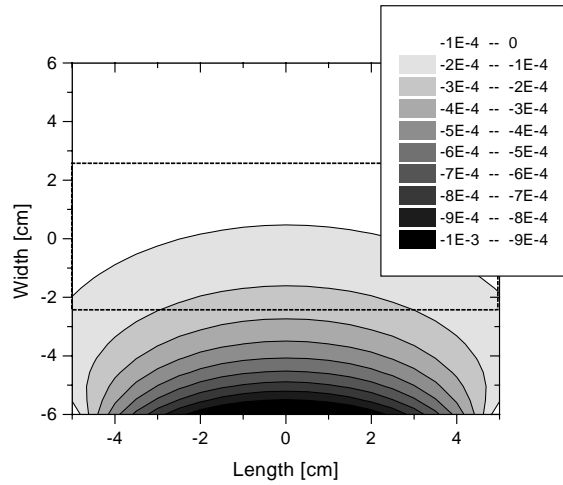


**Figure 5.16:** The potential in Volt along the central detector region (top view). The dashed line indicates the decay volume. Again the maximum potential encountered by the neutrons is less than 0.3 mV.

around the neutron beam with an aperture of  $12 \times 14 \text{ cm}^2$  (width  $\times$  height) for the neutron beam and apertures to the sides of dimensions  $10 \times 8 \text{ cm}^2$  for the electrons and protons. In addition four 1-dimensional grids with a wire spacing of 1 cm were placed in a grounded frame of dimensions  $12 \times 9 \text{ cm}^2$  between the foil and the neutron beam. The distance between the neutron beam center and the first grid was 8 cm in agreement with the calculations done before, where the electric field was assumed to significantly accelerate the protons at 10 cm from the beam center.

### 5.3.5 Primary electrons from neutron decay and the high voltage

The electrons from neutron decay also have to pass the foils on high voltage. Due to the gyrating motion this corresponds to a cut in the longitudinal energy of the electrons. We use the decreasing magnetic field to translate this into a cut in total energy. The longitudinal energy  $E_l(x_f)$  of an electron that was emitted perpendicular to the magnetic field is related to the magnetic field  $B(x_f)$ , both at the position of the foil  $x_f$ , by (Section 3.2.1):

$$\frac{E_l(x_f)}{E(x_0)} = 1 - \frac{B(x_f)}{B(x_0)}, \quad (5.17)$$

where  $E(x_0)$  and  $B(x_0)$  are the total kinetic energy and the magnetic field strength at the point of the decay  $x_0$ . Turning this argument around this implies a minimum total energy above which all electrons make it through the foils. For a potential of 25 keV and  $B(x_f)/B(x_0) = 3/4$  this energy threshold is 100 keV. To minimize this threshold requires to place the foils far from the neutron beam. A value of  $B(x_f)/B(x_0) = 3/4$  is obtained at a distance of about 30 cm from the center of the beam.

On the other hand, this threshold can be used to examine the calibration sources. The Auger electrons, included in our analysis of the calibration sources, can be suppressed with the high voltage turned on. Their influence on the detector calibration can thus be measured directly.

### 5.3.6 Summary of design criteria

The systematic effects discussed lead to different design criteria that are summarized here:

- The electric potential has to be constant on the level of 1 mV in the region of the neutron beam, leading to a preference for a small beam cross section with a grounded box around it.
- In order to insure that all electrons above  $\sim 100$  keV kinetic energy will pass through the foils at high voltage, the foils have to be placed at a distance from the neutron beam where the magnetic field has decreased to at least  $3/4$  of its maximum value, i.e. about 30 cm from the beam center. With a foil size of  $12 \times 9$  cm<sup>2</sup> this leads to a length and height of the decay volume of 9 cm and 6.8 cm respectively.
- The magnetic mirror effect requires to also reduce the width of the neutron beam and to limit the maximum electron energy used in the analysis in order to keep the correction on the same size as the statistical uncertainty. The width of the neutron beam should be made no larger than  $\sim 5$  cm.
- The long time of flight of the protons leads to a large contribution of accidental events to the signal. To minimize this effect, the accelerating electric field should start as close to the neutron beam as possible while the homogeneity of the field in the decay volume has to be preserved.

As opposed to the  $A$  measurement, in a  $B$  measurement the neutron beam has to be restricted much stronger. The given requirements lead to a reduction of the expected decay rate to about 15% of the 300 Hz in the  $A$  measurement. Nevertheless, with an increase of at least a factor of 3 in neutron beam intensity at the new PF1 beam the expected decay rate is  $0.15 \cdot 3 \cdot 300 = 135$  Hz. This is well above the minimum required from the statistical sensitivity of  $N_0 = 75$  Hz.

## 5.4 Detector design

The foils should be as large as possible to obtain sufficient statistics and to minimize edge effects. On the other hand the foils need to be extremely thin for the protons to be able to pass through and conducting to allow setting them on high voltage. In Table 5.1 the energy loss of protons in carbon is shown. The projected range can be identified with the penetration depth since after being accelerated in the electric field all protons hit the foils at close to normal incidence. Thus the maximum thickness of the foils is about  $40$   $\mu\text{g}/\text{cm}^2$ . This led to the choice of carbon as foil material, being the most commonly available material for foils that thin. Carbon however, is not the ideal element in terms of having

$E_p$ [keV]	Stopping power [keV·cm <sup>2</sup> /μg]	Proj. range [μg/cm <sup>2</sup> ]
10	0.41	26.5
15	0.47	36.9
20	0.51	46.4
25	0.55	55.3
30	0.58	63.7

**Table 5.1:** The total stopping power and projected range of protons with corresponding kinetic energies in amorphous carbon [Ber93]. The projected range is the range projected on the initial momentum direction.

Material	Secondary electron emission probability
C (diamond)	2.8
C (graphite)	1
Al	1
Al <sub>2</sub> O <sub>3</sub> (layer)	2 to 9
MgO (crystal)	20 to 25
MgO (layer)	3 to 15

**Table 5.2:** The secondary electron emission probability is given as number of secondary electrons emitted per primary electron incident normal to the surface. Therefore these numbers are just a general reference [Whe67].

a large secondary electron emission probability. Some secondary electron emission coefficients for different materials measured with normally incident electrons are given in Table 5.2. The large ranges of values indicate the high sensitivity to surface contaminations which in our case leads to the requirement that all foils have to be tested individually.

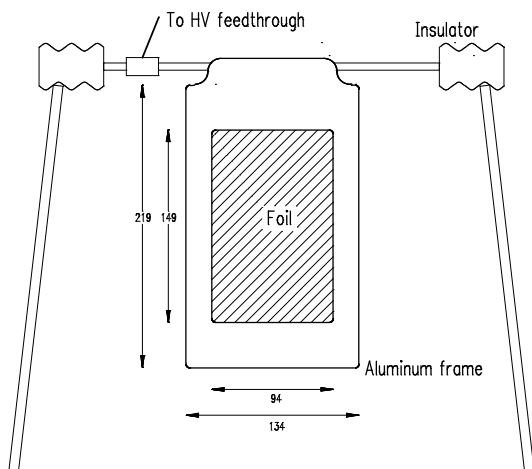


**Figure 5.17:** In the new detector design the use of insulators has been minimized. The frame on which the foil is mounted is completely covered by the proton detector. Any sharp edges were avoided and the outside was polished. For the beam a new version will be built with the foil placed horizontally.

The general trend in Table 5.2 of insulators having a comparatively high secondary electron emission probability can be understood in terms of their band structure. Secondary electrons with energies less than the gap width have no more electronic energy loss mechanisms available, leading to a higher probability of reaching the surface. Since there has been some experience already with a MgO layer on carbon foils [Sch96], we chose to explore this possibility as well. The average secondary electron emission probabilities for our foils were measured both in the forward and backward directions in a separate experiment in Munich [Pes98]. The result was that we expect about 3 secondary electrons in the forward direction for a pure carbon foil and 4.5-6 with an additional MgO layer. The foils are mounted on Aluminum frames which in turn are mounted in the proton detector.

In the last beam type a prototype was tested. A high voltage induced background made the proton detection impossible [Ast97]. One explanation is a possible ionization of residual gas atoms still present in the vacuum chamber. However, in the pressure range from  $10^{-6}$  to  $10^{-5}$  mbar no pressure dependence was found [Pes98] [Bül98]. Another or additional explanation is due to charging up and secondary electron emission from the insulator out of which the proton detector was made. Such a surface effect is required since the temperatures and field strengths in the setup

are too low to explain the observed background by either Richardson or field emission effect. In a new detector design, shown in Fig. 5.17, any insulator and sharp edges were avoided as much as possible, leading to a substantial decrease of the background. The onset of high voltage induced background was increased from  $\sim 6$  keV to  $\sim 16$  keV [Bül98]. A typical example of a background measurement is shown in Fig. 5.18. The high voltage induced background rate at 20 kV is about 100 Hz. This can only be a rough estimate since the actual rate depends sensitively on the surface condition and the history of the system. The background is reduced by leaving the high voltage on for several hours and by slowly raising it to the point where discharges set in. This process has been automated leading to the kind of measurement shown in Fig. 5.18 with several entries for each potential, which is raised until the increase in the countrate reaches a chosen limit.

The high voltage induced background has to be compared to the background measured during the last beam time. With ‘shutter up’ (Fig. 3.1) closed, the background rate in one detector was about 35 Hz. For the *B* measurement the scintillator will be made only about 1/3 the size of the one in the last beam time. With the limited foil size available a larger scintillator is not necessary. Since the background rate from the shutter is proportional to the scintillator size the background rate currently would be dominated by the high voltage induced background. To separate the requirements for the proton detector design from the design of the frames, the proton detector is made to incorporate the foil frames such that possible edges of the foil frames are covered. With these improvements proton detection in the PERKEO spectrometer became possible.

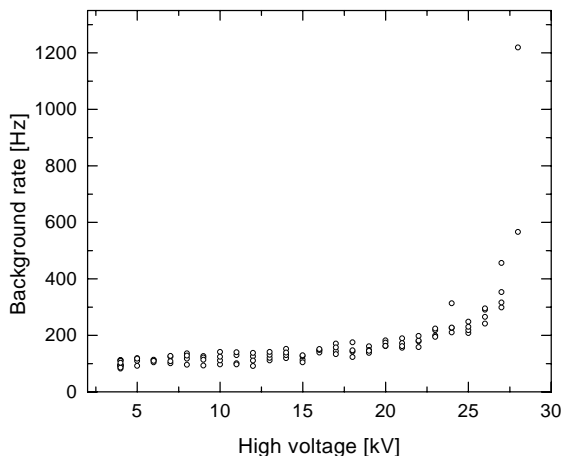


**Figure 5.18:** A typical example of the background rate depending on the applied high voltage measured when the bending magnet in the proton source is turned of.

## 5.5 Test measurements

For test purposes a proton source was constructed. Residual gas atoms are ionized by electron impact and then accelerated and mass selected by electric and magnetic fields [Bül98]. The setup for the tests described in the following is shown in Fig. 5.19. In order to maximize the light collection efficiency, a scintillator was attached directly to a photomultiplier tube.

In first measurements the ground potential on the side of the scintillator had been defined by a wire grid. In these tests the proton detection efficiency changed drastically after small discharges that occur occasionally at high voltages. This is shown in Fig. 5.20 where the proton rate was corrected for background by taking the difference of measurements with the

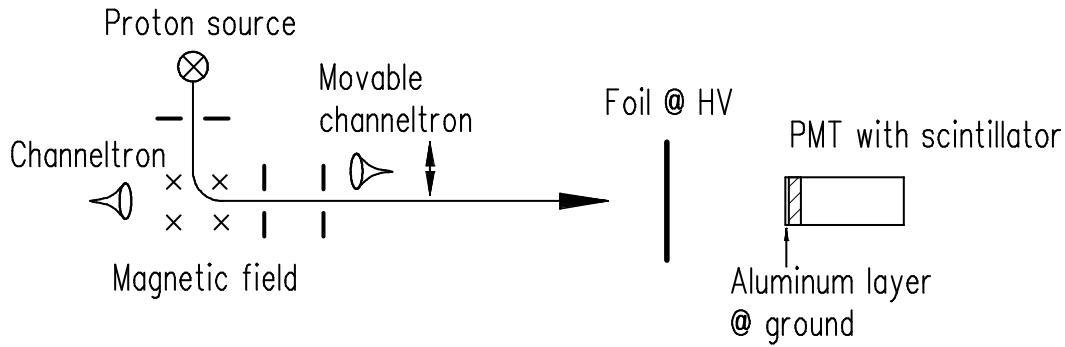


**Figure 5.19:** A schematic of the setup for testing the proton detector (top view). Residual gas atoms are ionized and accelerated in the source. Protons are selected in a bending magnet. Two channeltrons were used for systematic tests.

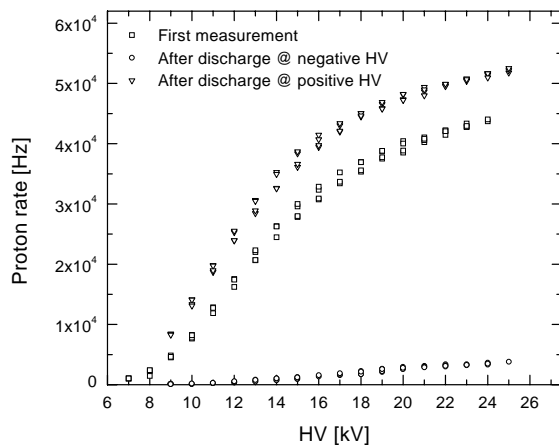


**Figure 5.20:** After a discharge with negative HV the scintillator is negatively charged and the proton detection efficiency nearly vanishes. After reversing the voltage and inducing another discharge the scintillator is positively charged and protons are detected with an even higher efficiency than originally.

magnetic field in the proton source on and off. Apparently the scintillator was charged to a similar potential as the one of the foils by the discharges, hence the secondary electrons could no longer be detected. A thin layer of Aluminum was sputtered on the scintillator to prevent this. This layer was connected to the vacuum chamber to avoid charging of the scintillator at the same time making the wire grid superfluous. The thinness of the layer was estimated to be about  $\sim 300$  nm, since it is semitransparent. The additional energy loss of electrons at 20 keV is  $\Delta E = 0.8$  keV. Thus the energy loss is tolerable while the light collection efficiency, especially when read out from the back, is increased.

In Fig. 5.21 proton energy spectra are shown for different foil potentials. At a potential of 30 kV the proton signal is well separated from the background. From the change in peak positions with high voltage applied one can obtain calibration curves for the first three peaks shown in Fig. 5.22. Since the gains from the peaks behave as 1 : 2.1(2) : 3.6(3) we deduce that the three peaks correspond to the cases with one, two, and three secondary electrons being emitted.

The proton energy spectra were described by a sum of monoenergetic electrons with energies  $n \times HV$ , where  $n$  was in the range from 1 to 9. Then the spectra were convoluted with our detector function (Section 3.3) and in a fit routine the probabilities for the different numbers of secondary electrons emitted were determined. An example of such a fit is shown in Fig. 5.23

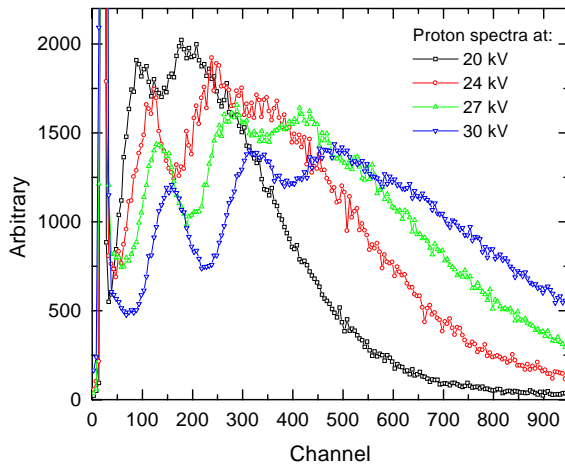


**Figure 5.21:** Proton spectra measured with a carbon foil at different potentials.

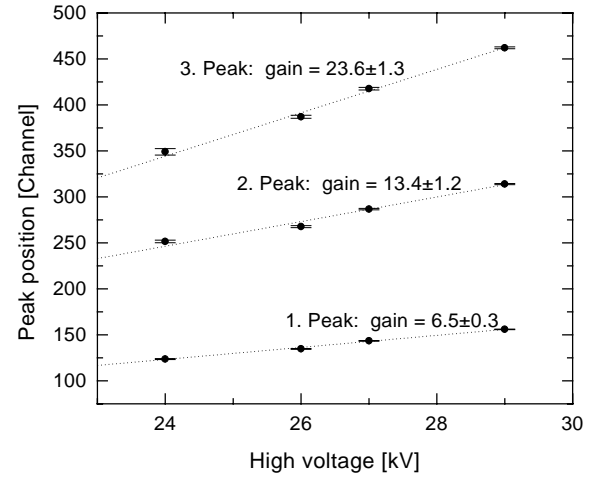


**Figure 5.22:** The change of the different peak positions with increasing potential gives the gain in channels/keV for each peak.

and the corresponding distribution of secondary electrons is shown in Fig. 5.24. From the width of the first peak the number of photoelectrons per MeV,  $p_{\text{MeV}} = 550$ , was obtained. The pedestal was measured to be  $C_{\text{ped}} = 10$ .

In order to calibrate the energy, the gain obtained in each fit was multiplied with the corresponding high voltage. This yields a channel number corresponding to the first peak, including however the gain obtained from the whole spectrum. In Fig. 5.25 the results are shown versus the high voltage. From a linear fit to the data the gain is determined to be  $g = 6.58(14)$  channel/keV and from the extrapolation of the fit to the pedestal an unaccounted energy loss of  $E_0 = 6.5(8)$  keV was found.

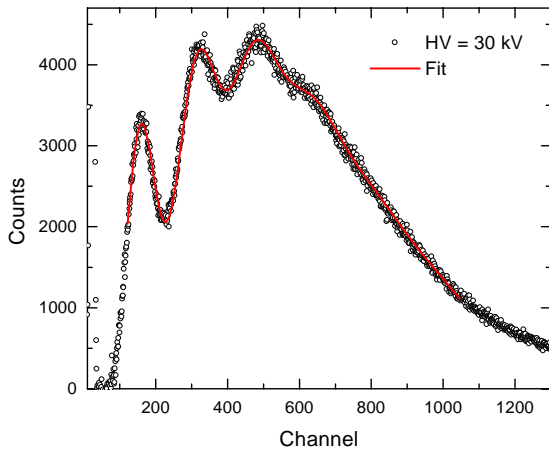


**Figure 5.23:** The proton energy spectrum measured with a carbon foil at 30 keV is shown together with a fit from which the distribution of secondary electrons was obtained.

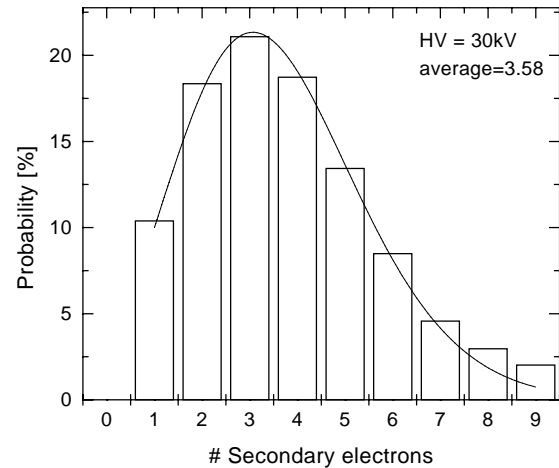


**Figure 5.24:** The distribution of secondary electrons for a carbon foil at 30 keV.

The uncertainties were inflated to get  $\chi^2 = 1$  in the fit in order to obtain reasonable error estimates.

This energy calibration was further checked by an absolute calibration using a  $^{241}\text{Am}$  source that produces an X-ray with 59.5 keV. Above a much higher contribution from the lower energy X-rays the photo peak was detectable as shown in Fig. 5.26. While the peak position of  $C_{\text{Am}} = 390(3)$  is higher than the peak corresponding to two secondary electrons produced at 30 keV ( $\approx 310$ ) it is in agreement with the above calibration. Since the X-ray energy is deposited directly inside the scintillator the dead layer energy loss  $E_0$  does not apply here, leading to the expectation:  $C_{\text{exp}} = 6.58 \cdot 59.5 + 10 = 402$ .

Carbon foils with an additional layer of MgO have been tested next. Proton spectra measured with the same foils before and after an additional MgO layer had been deposited are shown in Fig. 5.27. As expected the signal is strongly enhanced. At a potential of 22 kV the signal from the pure carbon foil was still difficult to separate from the background and the maximum was around channel 200. With the MgO layer, the signal at the same voltage was already better separated from the background and the maximum of the spectrum was above channel 400. When the high voltage was raised further to 29 kV the main maximum moved up to around channel 700.

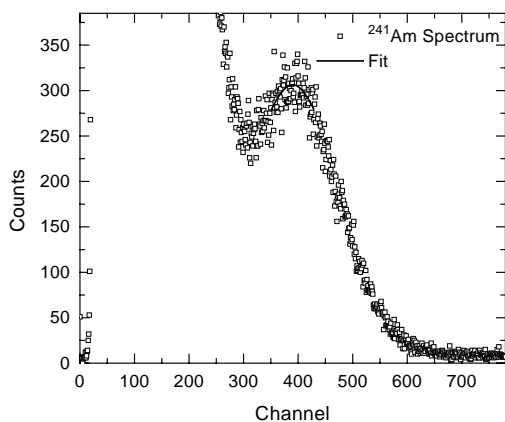


**Figure 5.26:** The photopeak of a  $^{241}\text{Am}$  source with a Gaussian fit. From this fit the peak position was determined to be  $C_{\text{Am}} = 390(3)$ .

The fits were compared to the total number of events to get a measure for the detector inefficiency. This way fractions on the order of 0.1 to 0.3% were obtained. The loss fractions decreased

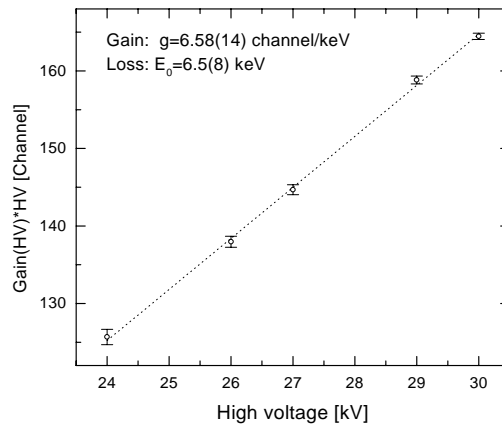


**Figure 5.25:** Calibration of the detector from fits to the proton spectra at different potentials. From the linear fit a gain of  $g = 6.58(14)$  channel/keV and an unaccounted energy loss of  $E_0 = 6.5(8)$  keV were found. The gain agrees well with the one obtained from the shift of the first peak directly (Fig. 5.22).

Distributions of secondary electrons emitted were obtained from fits to these spectra as well. The results for the two MgO spectra shown in Fig. 5.27 are given in Fig. 5.28. The average number of secondary electrons from the pure carbon foil was 3.58 at 30 keV, somewhat higher than expected from the experiment in Munich. For the foils with MgO layer the average is increased up to 4.9 at 29 keV, in agreement with the expectations from the measurements in Munich [Pes98].

Since the peak corresponding to only one secondary electron emitted is well resolved from the background in the proton energy spectra, the threshold can be set in the minimum below the peak. The number of events falling below this assumed threshold in the extensions of the

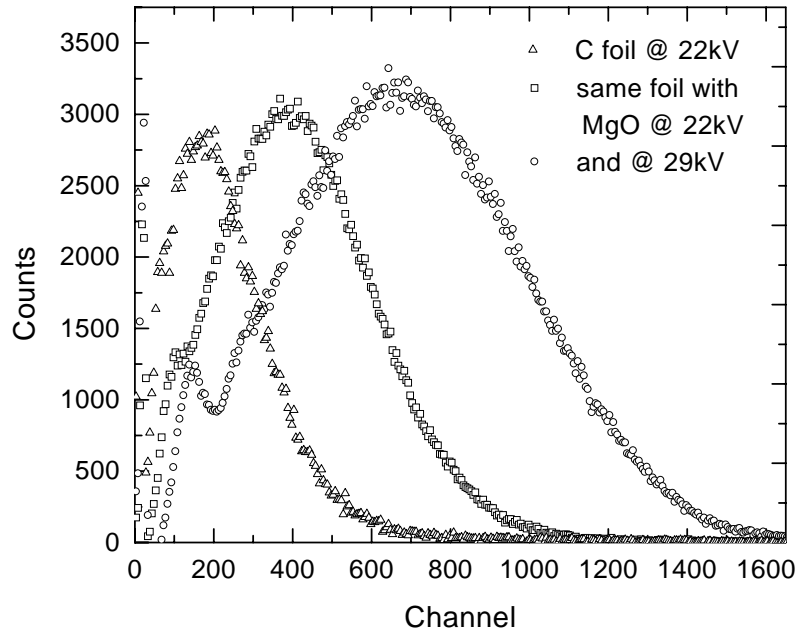


**Figure 5.27:** The proton energy spectrum measured with a carbon foil at 22 keV and subsequently with the same foil with an additional MgO layer at the same potential and also at 29 keV. The number of secondary electrons emitted is strongly increased. Already at 22 keV the signal is now well separated from the background.

with increasing potential applied but were similar for foils with and without MgO layer. The larger signal from foils with a MgO layer did not improve the situation due to the increased background observed from foils with MgO.

However, a second and larger contribution to events missed in the proton detector is expected from events where no secondary electrons are emitted. In order to evaluate the size of this

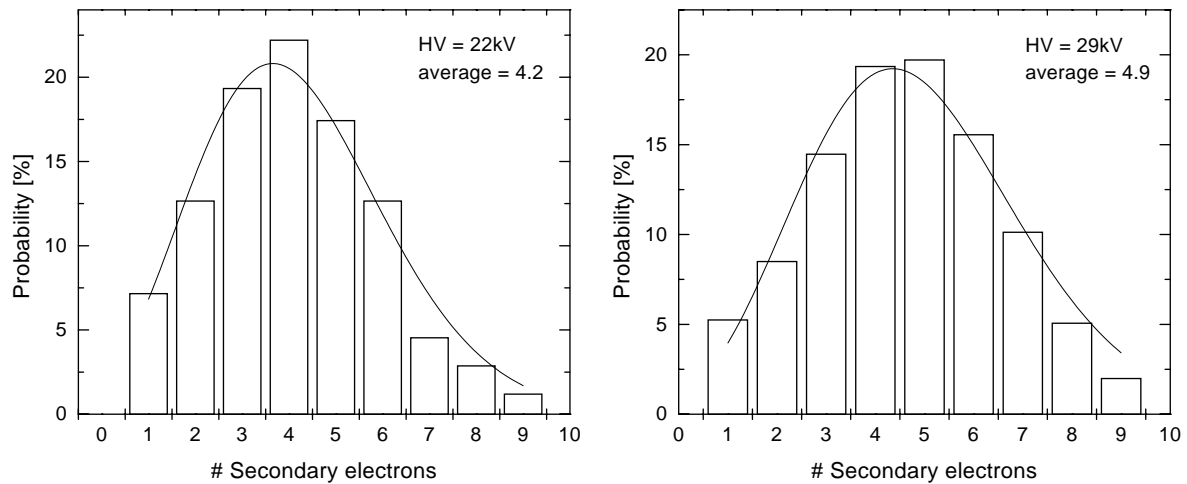


**Figure 5.28:** The distribution of secondary electrons obtained from fits to the two spectra using a foil with a MgO layer. A fit using a Poisson distribution yielding the given averages is shown as well.

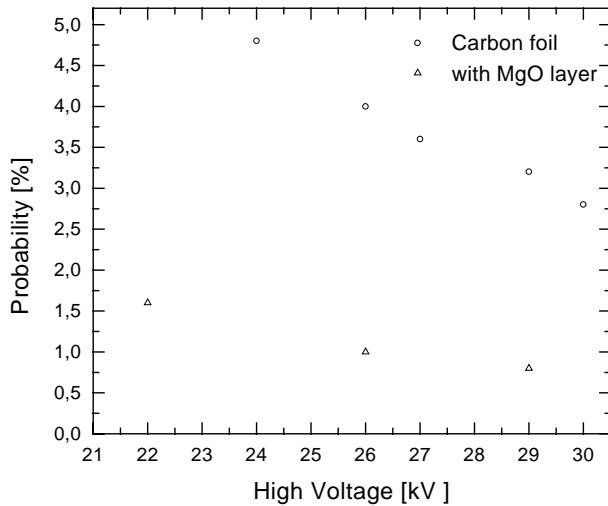


**Figure 5.29:** The probability that no secondary electron is emitted is shown versus the potential of the foils. The assumption that the Poisson distributions can be extended to the case without secondary electron emission is made.

effect, the probability that no secondary electron is emitted has to be estimated. Therefore the fit of a Poisson distribution to the measured secondary electron distributions is included in Figures 5.24, and 5.28. The Poisson fit was never satisfactory using the uncertainties in the secondary electron intensities as obtained from the fits to the proton spectra. However, the Poisson distributions are a reasonable assumption in order to extrapolate the observed intensities to the case without secondary electron emission. The resulting probabilities to miss a proton for the two foil types depending on the high voltage are shown in Fig. 5.29. The proton detection efficiency of the detector using a foil with a MgO layer is increased to 98 to 99 % as opposed to 95 to 97 % for a pure carbon foil.

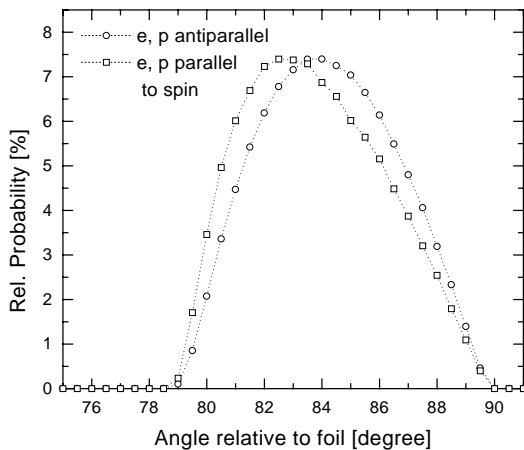


**Figure 5.30:** The distributions of incident angles on the foil is shown for a potential of 20 keV. The decreasing magnetic field has been neglected in this calculation and will lead to the true angles being even closer to normal.

incidence on the foil has been calculated by adding a momentum corresponding to a longitudinal energy of 20 keV to the momenta with which the protons were emitted. Thus both

As long as the detection efficiency is independent of the proton phase space an imperfect detection efficiency just leads to a loss of statistics. The more critical question is, whether the detection efficiency depends on the angle or the energy with which the protons have been emitted. In this respect a high detection efficiency is useful since only the phase space dependency of the difference to 100 % is relevant. After being accelerated in the electric field no large dependencies are expected. With a maximum proton energy of 750 eV, the relative variation of the kinetic energy is on the order of:

$$\frac{\Delta E}{E} \approx \frac{750 \text{ eV}}{20 \text{ keV}} = 3.8 \%. \quad (5.18)$$

And the angle of incidence on the foil is close to normal for all protons. This is shown in Fig. 5.30 where the distribution of angles of

the energy and the angle with which the protons hit the foil show only small variations depending on the phase space of emission. Therefore, the detection efficiency should be almost independent of the proton phase space as well. Nevertheless, work is in progress to check this expectation experimentally [Bra00].

# Chapter 6

## Summary

The major objective of this thesis was the measurement of the correlation coefficient  $A$  in neutron decay. The result obtained:  $A = -0.1189(8)$  is the most precise determination of this quantity to date, yielding for the ratio of axial to vector coupling constant:  $\lambda = -1.2740(21)$ . This result is in agreement with the previous  $A$  measurement using the PERKEOII spectrometer [Abe97], whereas an inconsistency prevails between the PERKEOII measurements and the ones by other groups. However, the advantage of the PERKEOII spectrometer is that its systematic effects are smaller by about one order of magnitude than in any of the other experiments, lending our result an increased credibility. Eventually, this issue will have to be clarified by future experiments.

The most interesting implication of our result is the value of the  $V_{ud}$  element of the CKM matrix which can be determined from a combination of the correlation coefficient  $A$  and the neutron lifetime. Since the CKM matrix merely relates the quark eigenstates of the weak interaction with the quark mass eigenstates it has to be unitary, leading to the requirement that the squares of the elements in each row and column have to add up to one. This condition can be tested most precisely in the first row, where  $V_{ud}$  gives the largest contribution to the sum. The other elements in the first row,  $V_{us}$  and  $V_{ub}$ , are determined in the decays of heavy mesons and play only a minor role in the unitarity test. With  $V_{ud}$  determined from nuclear beta decays, a deviation from the unitarity condition is found. However, its significance is controversially discussed since the precise experimental results are obscured by nuclear structure dependent corrections [Tow98]. These limiting theoretical corrections do not enter in the evaluation of  $V_{ud}$  from neutron decay data thus allowing to clarify this situation. Our result,  $V_{ud} = 0.9713(14)$ , leads to a violation of the unitarity condition on the level of  $3\sigma$ . While the current status of the experimental situation is not satisfactory this result is tantalizingly similar to the one obtained from nuclear beta decay.

The second part of this thesis was dedicated to the preparation of a neutrino asymmetry measurement. Since the neutrino can not be detected efficiently, one has to rely on a coincident detection of the proton and the electron instead. An additional constraint of our experimental scheme is that the proton and the electron from a decay have to be measured in the same detector, in which case the momentum direction of the neutrino can be inferred directly. The solution is to convert the protons to electrons by secondary electron emission from thin foils on negative high potential and to detect the secondary as well as the decay electrons in a scintillator [Str78]. Such a proton detector was built and was shown to work reliably with

the proton signal well separated from the background. Several analytical and Monte Carlo calculations were performed as well, in order to estimate systematic effects in the experimental realization of a  $B$ -measurement using this detector. The results led to specific design criteria for the implementation of the proton detector in the PERKEO II spectrometer allowing for a systematically clean measurement on the level of about 0.2%. The determination of the correlation coefficient  $B$  is planned for the beginning of the year 2000.

# Appendix A

## The fit function for the experimental asymmetry

Here, the complete function used in the fit of the experimental asymmetry is given. Eq. (4.25) is convoluted with the detector response function  $f(C, E)$ , Eq. (3.13), in the fitting routine:

$$A_{\text{exp}}(C) = \frac{1}{2}fp \frac{\int dE f(C, E)F(E)'[1 - W_1(E)] \cdot A(E)\beta}{\int dE f(C, E)F(E)'[1 - W_2(E)]}, \quad (\text{A.1})$$

where  $f, p$  are the polarization and spin flipping efficiencies,  $C$  is the channel number,  $\beta$  is the electron velocity in units of the speed of light, and an energy dependence is included in the correlation coefficient  $A(E)$ . In addition, the corrections for the edge effect,  $W$ , are included explicitly (see Section 3.3.4).

The corrected Fermi spectrum  $F(E)'$ , with energies in the following in units of MeV, is given by:

$$F(E)' \propto \underbrace{(E_0 - E)^2 \sqrt{E^2 - m_e^2}}_{\text{phasespace}} (E + m_e) (1 + \delta_R(E)) (1 + R_0(E)) F_C(E), \quad (\text{A.2})$$

where  $E$  is the kinetic energy of the electrons with the maximum of

$$E_0 = \Delta - \frac{\Delta^2 - m_e^2}{2m_n} - m_e \approx 0.782 \text{ MeV}, \quad (\text{A.3})$$

and  $m_e$  is the electron mass,  $m_n$  is the average nucleon mass, and  $\Delta = 1.293 \text{ MeV}$  is the total energy released in the decay. The corrections to the phase space factor are external radiative corrections,  $\delta_R(E)$ , corrections for proton recoil,  $R_0(E)$ , and Coulomb corrections,  $F_C(E)$ .

The external radiative correction,  $\delta_R(E)$ , to first order in the fine structure constant  $\alpha$  is

given in [Sir67]:

$$\begin{aligned} \delta_R(E) = & \frac{\alpha}{2\pi} \left\{ 3 \ln \frac{m_p}{m_e} - \frac{3}{4} \right. \\ & + 4 \left( \frac{\operatorname{atanh} \beta}{\beta} - 1 \right) \left[ \frac{E_0 - E}{3(E + m_e)} - \frac{3}{2} + \ln \frac{2(E_0 - E)}{m_e} \right] \\ & + \frac{4}{\beta} L \left( \frac{2\beta}{1 + \beta} \right) \\ & \left. + \frac{\operatorname{atanh} \beta}{\beta} \left[ 2(1 + \beta^2) + \frac{(E_0 - E)^2}{6(E + m_e)^2} - 4 \operatorname{atanh} \beta \right] \right\}, \end{aligned} \quad (\text{A.4})$$

where  $L(z)$  ist die Spence-Funktion:

$$L(z) = \int_0^z \frac{\ln(1-t)}{t} dt. \quad (\text{A.5})$$

The explicit form of  $R_0(E)$ , the recoil correction, is given in [Wil82]:

$$\begin{aligned} R_0(E) = & \frac{1}{1 + 3\lambda^2} \left\{ 2 \frac{E + m_e}{m_n} + \lambda^2 \left[ 10 \frac{E + m_e}{m_n} - 2 \frac{m_e^2}{m_n(E + m_e)} - 2 \frac{E_0 + m_e}{m_n} \right] \right. \\ & \left. + \lambda(1 + 2\kappa) \left[ 2 \frac{E_0 + m_e}{m_n} - 4 \frac{E + m_e}{m_n} + 2 \frac{m_e^2}{m_n(E + m_e)} \right] \right\} \\ \approx & 10^{-3} \cdot \left\{ -3.58 - \frac{0.723}{(E + m_e)} + 7.66(E + m_e) \right\}, \end{aligned} \quad (\text{A.6})$$

where  $\kappa$  is half the difference of the anomalous magnetic moments of proton and neutron, related to the weak magnetism form factor defined in Eq.(2.18) by  $\kappa = g_{WM}/2$ . The standard model prediction  $\kappa = 1.85$  was used in the fit routine.

The Coulomb corrections take the interaction between the outgoing electron and proton in the final state into account. Here an approximation, the Fermi function  $F_C(E)$ , is used:

$$F_C(E) = \frac{2\pi\alpha/\beta}{1 - \exp(-2\pi\alpha/\beta)}. \quad (\text{A.7})$$

The corrections for the edge effect are given in [Bae96]:

$$W_1(E) = \frac{\sqrt{E^2 + 2Em_e}}{c} \frac{4}{3eBL} \quad (\text{A.8})$$

$$W_2(E) = \frac{\sqrt{E^2 + 2Em_e}}{c} \frac{\pi}{2eBL}, \quad (\text{A.9})$$

where  $B$  is the magnetic field strength,  $L$  is the length of the decay volume,  $e$  is the electron charge, and  $c$  is the velocity of light.

Finally, the energy dependence of  $A$  due to nucleon recoil terms is given in [Wil82]:

$$A(E) = A' \left\{ 1 + A_{\mu M} \left[ A_1 \frac{E_0 + m_e}{m_e} + A_2 \frac{E + m_e}{m_e} + A_3 \frac{m_e}{E + m_e} \right] \right\} \quad (\text{A.10})$$

with

$$\begin{aligned}
 A_{\mu\text{M}} &= \frac{-\lambda + 2\kappa + 1}{-\lambda(1 + \lambda)(1 + 3\lambda^2)} \frac{m_e}{m_n} && \sim -1.7 \cdot 10^{-3} && \text{(A.11)} \\
 A_1 &= \lambda^2 - \frac{2}{3}\lambda - \frac{1}{3} && \sim 2.1 \\
 A_2 &= \lambda^3 - 3\lambda^2 + \frac{5}{3}\lambda + \frac{1}{3} && \sim -8.7 \\
 A_3 &= 2\lambda^2(1 + \lambda) && \sim -0.87.
 \end{aligned}$$

Outer radiative corrections  $\delta A_R$ , that are nearly independent of energy, still have to be applied to  $A'$  in order to obtain the correlation coefficient  $A$ :

$$A' = A \cdot (1 - \delta A_R/A) . \quad \text{(A.12)}$$

This correction accounts for the change of electron momenta due to photon emission. The value used (Table 4.6) is  $\delta A_R/A = 9 \cdot 10^{-4}$  with an estimated relative uncertainty of 10 % [Glü92].



# Acknowledgements

At this point I would like to thank all the people who have contributed to the success of this project:

I am grateful to Prof. Dr. Dubbers, for giving me the opportunity to do this interesting work, for entrusting me with the PERKEO project, and for offering me the chance to present my results at various conferences.

The experience of Priv. Doz. Dr. Hartmut Abele was very helpful leading to many useful suggestions during his supervision of this dissertation. I also thank him for his stimulating enthusiasm in many interesting discussions.

Special thanks go to Dr. Stefan Baeßler, for his invaluable help during all phases of this thesis. He always found the time and had the detailed knowledge to answer my questions. His continued interest in this work, even when far away, is greatly appreciated.

The support of Diploma students was and is absolutely crucial to the project and I would like to thank Marga, Uta, Philipp, Christian, and Bernhard. My successor Michael Kreuz has already contributed to this work as well.

Furthermore, the whole ANP group will be missed. The always supportive atmosphere was very enjoyable and fortunately we shared more than ‘just’ physics. First of all I want to thank Frank<sup>1</sup>, Sascha and their fellow spin echo group members. Martin and the ultra cold neutron people, and our neighbours from the liquid helium laboratory, were always willing to help out with missing equipment as well. Harry helped in grounding the scintillator, and the sputtering group not only maintained the coffee room but is also building the new neutron guide. I owe Dr. Christian Schmidt a bicycle and many thanks for a place to stay. It was a pleasure to have Tanja and Claudia next doors, who frequently offered their help and their chocolates. Many useful suggestions were made by my room-mate Bernhard after careful proof reading.

Dr. Ferenc Glück provided interesting discussions on the theory of neutron decay and also MC simulations of our experiment. The random number generator I used in Monte Carlo calculations was written by Dr. Utz Schmidt.

The foils used in the proton detection were produced by target laboratories at the University of Munich and at the GSI in Darmstadt. The tedious task of producing the fragile foils was performed by Dr. Maier-Komor and Mrs. Nacke in Munich and the group of Dr. Lommel at the GSI. When the foils were really scarce, Priv. Doz. Dr. Klaus Jungmann helped us

---

<sup>1</sup>The L<sup>A</sup>T<sub>E</sub>X ‘Kwäck’

out and generously let us use some of his. I am also indebted to him for several stimulating questions and discussions.

The good cooperation with both the mechanical and electronics workshops at the Physical Institute is gratefully acknowledged.

For the beam time we spent several long months at the ILL in Grenoble and I would like to express my thanks to all who have helped us to overcome the many problems we faced. The *A*-measurement would not have been as successful without the two beam responsables Dr. Oliver Zimmer, who also pushed the  $^3\text{He}$  polarization analysis technique, and Dr. Valery Neshvizevsky, who performed the supermirror polarization analysis. The assistance of the various technical divisions at the ILL was indispensable.

Last but not least I want to express my gratitude towards my parents. They always supported and encouraged me throughout the years of my education.

# Bibliography

- [Aba96] S. ABACHI *et al.* Phys. Rev. Lett., **76**, 3271 (1996).
- [Abe92] ABE *et al.* Phys. Rev. Lett., **68**, 447 (1992).
- [Abe95] ABE *et al.* Phys. Rev., **D 51**, 4623 (1995).
- [Abe97] H. ABELE, S. BAESSLER, D. DUBBERS, J. LAST, U. MAYERHOFER, C. METZ, T. MÜLLER, V. NESVIZHEVSKI, C. RAVEN, O. SCHÄRPF, and O. ZIMMER. Phys. Lett., **B 407**, 212 (1997).
- [Abe98] H. ABELE. *Meßgrößen des Neutronzerfalls und das Standardmodell der Teilchenphysik*. Habilitation (1998).
- [Abr62] K. ABRAHAMS, O. STEINSVOLL, P. J. M. BONGAARTS, and P. W. LANGE. Rev. Sci. Instr., **33**, 524 (1962).
- [Ade93] E. G. ADELBERGER. Phys. Rev. Lett., **70**(19), 2856 (1993).
- [Als64] J. ALS-NIELSEN and O. DIETRICH. Phys. Rev., **B 133**(4), 925 (1964).
- [Arn99] R. A. ARNDT, R. L. WORKMAN, I. I. STRAKOVSKY, and M. M. PAVAN. nucl-th/9807087 (1999).
- [Ast97] M. ASTRUC HOFFMANN. *Ein Präzisionsexperiment zur Bestimmung der  $\beta$ -Asymmetrie im Neutronenzerfall*. Master's thesis, University of Heidelberg (1997).
- [Bae96] S. BAESSLER. *Die Betaasymmetrie im Zerfall des freien Neutrons*. Ph.D. thesis, University of Heidelberg (1996).
- [Ber63] J. BERGER. *Monte Carlo Calculation of the Penetration and Diffusion of Fast Charged Particles*, vol. I of *Methods in Computational Physics*. Academic Press (1963).
- [Ber93] M. J. BERGER. *Pstar Database*. NIST homepage: <http://physics.nist.gov> PhysRef-Data (1993).
- [Boo84] A. I. BOOTHROYD, J. MARKEY, and P. VOGEL. Phys. Rev., **C 29**(2), 603 (1984).
- [Bop86] P. BOPP, D. DUBBERS, L. HORNIG, E. KLEMT, J. LAST, H. SCHÜTZE, S. FREEDMAN, and O. SCHÄRPF. Phys. Rev. Lett., **56**(9), 919 (1986).

- [Bow99] C. J. BOWERS, S. J. FREEDMAN, B. K. FUJIKAWA, A. O. MACCHIAVELLI, R. W. MACLEOD, J. REICH, S. Q. SHANG, P. A. VETTER, and E. WASSERMAN. *Phys. Rev.*, **C 59**(2), 1113 (1999).
- [Bra00] B. BRAND. Master's thesis, University of Heidelberg. In progress.
- [Bül98] P. VON BÜLOW. *Aufbau eines Protonendetektors zur Messung der Neutrinoasymmetrie im Neutronenzerfall*. Master's thesis, University of Heidelberg (1998).
- [Byr94] J. BYRNE. *Neutrons, Nuclei and Matter: An Exploration of the Physics of Slow Neutrons*. Inst. of Physics Publ., Bristol (1994).
- [Cab63] N. CABIBBO. *Phys. Rev. Lett.*, **10**, 531 (1963).
- [Cla74] D. CLARK. *Nucl. Instr. Meth.*, **117**, 295 (1974).
- [Com73] E. D. COMMINS. *Weak Interactions*. Cambridge University Press, Cambridge (1973).
- [Com83] E. D. COMMINS and P. H. BUCKSBAUM. *Weak Interactions of Leptons and Quarks*. Cambridge University Press, Cambridge (1983).
- [Dob75] R. DOBROZEMSKY, E. KERSCHBAUM, G. MORAW, H. PAUL, C. STRATOWA, and P. WEINZIERL. *Phys. Rev. D*, **11**(3), 510 (1975).
- [Döh90] J. DÖHNER. *Der Beta-Zerfall freier Neutronen und rechtshändige Ströme*. Ph.D. thesis, University of Heidelberg (1990).
- [Don95] S. J. DONG, J.-F. LAGAË, and K. F. LIU. *Phys. Rev. Lett.*, **75**(11), 2096 (1995).
- [Dub91] D. DUBBERS. *Prog. Part. Nucl. Physics*, **26**, 173 (1991).
- [Eri99] T. E. O. ERICSON, B. LOISEAU, and A. W. THOMAS. hep-ph/9907433 (1999).
- [Ero91] B. EROZOLIMSKII, I. KUZNETSOV, I. KUIDA, Y. MOSTOVOY, and I. STEPANENKO. *Phys. Lett.*, **B 263**, 33 (1991).
- [Fer34] E. FERMI. *Zeitschrift f. Physik*, **88**, 161 (1934).
- [Fie98] K. FIEDERER. *Entwicklung und Produktion von Supermirrors für einen Neutronenleiter*. Master's thesis, University of Heidelberg (1998).
- [Fuj99] B. K. FUJIKAWA, S. J. ASZTALOS, R. M. CLARK, M.-A. DELEPLANQUE-STEPHENS, P. FALLON, S. J. FREEDMAN, J. P. GREENE, I.-Y. LEE, L. J. LISING, A. O. MACCHIAVELLI, R. W. MACLEOD, J. C. REICH, M. A. ROWE, S.-Q. SHANG, F. S. STEPHENS, and E. G. WASSERMAN. *Phys. Lett.*, **B 449**, 6 (1999).
- [Gla61] S. L. GLASHOW. *Nucl. Phys.*, **22**, 579 (1961).
- [Glü92] F. GLÜCK and K. TÓTH. *Phys. Rev.*, **D 46**(5), 2090 (1992).
- [Glü95] F. GLÜCK, I. JOÓ, and J. LAST. *Nucl. Phys. A*, **593**, 125 (1995).
- [Glü98] F. GLÜCK. Priv. comm.

- [Hei95] W. HEIL, H. HUMBLLOT, E. OTTEN, M. SCHAFER, R. SARKAU, and M. LEDUC. Phys. Lett., **A 201**, 337 (1995).
- [Hir96] M. HIRSCH, H. V. KLAPDOR-KLEINGROTHAUS, and O. PANELLA. Phys. Lett., **B 374**, 7 (1996).
- [Høg99] P. HØGHØJ, H. ABELE, M. ASTRUC HOFFMANN, S. BAESSLER, J. REICH, V. NESVIZHEVSKY, and O. ZIMMER. Nucl. Instr. Meth. Accepted for publication.
- [Hol74] B. R. HOLSTEIN. Rev. Mod. Phys., **46**, 789 (1974).
- [Jac57] J. D. JACKSON, S. B. TREIMAN, and H. WYLD JR. Phys. Rev., **106**(3), 517 (1957).
- [Kob73] M. KOBAYASHI and T. MASKAWA. Prog. Theo. Phys., **49**, 652 (1973).
- [Lar77] F. P. LARKINS. Atomic and Nuclear Data Tables, **20**(4), 311 (1977).
- [Led78] C. M. LEDERER and V. S. SHIRLEY. *Table of Isotopes*. 7 ed. Wiley-Interscience (1978).
- [Lee56] T. D. LEE and C. N. YANG. Phys. Rev., **104**, 254 (1956).
- [Lia97] P. LIAUD, K. SCHRECKENBACH, R. KOSSAKOWSKI, H. NASTOLL, A. BUSSIÈRE, J. P. GUILLAUD, and L. BECK. Nucl. Phys. A, **612**, 53 (1997).
- [Lip62] LIPKIN. *Beta decay for pedestrians*. North Holland Publ. Comp., Amsterdam (1962).
- [Liu94] K. F. LIU, S. J. DONG, T. DRAPER, J. M. WU, and W. WILCOX. Phys. Rev., **D 49**(9), 4755 (1994).
- [McF85] W. K. MCFARLANE, L. B. AUERBACH, F. C. GAILLE, V. L. HIGHLAND, E. JASTRZEMBSKI, R. J. MACEK, F. H. CVERNA, C. M. HOFFMAN, G. E. HOGAN, R. E. MORGADO, J. C. PRATT, and R. D. WERBECK. Phys. Rev., **D 32**, 547 (1985).
- [Met95] C. METZ. *Messungen zur Bestimmung der  $\beta$ -Asymmetrie im Neutronenzerfall mit Perkeo II*. Master's thesis, University of Heidelberg (1995).
- [Mül96] T. MÜLLER. *Messung der  $\beta$ -Asymmetrie im Neutronenzerfall mit Perkeo II*. Master's thesis, University of Heidelberg (1996).
- [NDS94] Nucl. Data Sheets, **72**(3) (1994).
- [Nes98] V. NESHVIZHEVSKI. Priv. comm.
- [new97a]  $\pi N$  Newsletter, **13**, 96 (1997).
- [new97b]  $\pi N$  Newsletter, **13**, 80 (1997).
- [Orm95] W. E. ORMAND and B. A. BROWN. Phys. Rev., **C 52**, 2455 (1995).
- [Pag75] H. PAGELS. Phys. Rep., **16**(5), 219 (1975).
- [Pas66] L. PASSELL and R. I. SCHERMER. Phys. Rev., **150**(1), 146 (1966).
- [Pau33] W. PAULI. Handbuch der Physik, **24**(1), 233 (1933).

- [PDG96] PARTICLE DATA GROUP. Phys. Rev., **D 54**, 1 (1996).
- [PDG98] C. CASO *et al.* European Physical Journal, **C 3**, 1. And 1999 partial update from URL: <http://pdg.lbl.gov> (1998).
- [Pes98] U. PESCHKE. *Messung der Neutronen- $\beta$ -Asymmetrie A mit Perkeo II & Sekundärelektronenemission an dünnen Folien*. Master's thesis, University of Heidelberg (1998).
- [Plo00] C. PLONKA. Master's thesis, University of Heidelberg. In progress.
- [Rah98] J. RAHM, J. BLOMGREN, H. CONDÉ, S. DANGTIP, K. ELMGREN, N. OLSSON, T. RÖNNQVIST, R. ZORRO, A. RINGBOM, G. TIBELL, O. JONSSON, L. NILSSON, P.-U. RENBERG, T. E. O. ERICSON, and B. LOISEAU. Phys. Rev., **C 57**(3), 1077 (1998).
- [Rav95] C. RAVEN. *Erste Messungen mit Perkeo II:  $\beta$ -Asymmetrie im Neutron-Zerfall*. Master's thesis, University of Heidelberg (1995).
- [Rei91] R. REINER. *Winkel-Korrelationskoeffizienten im Neutronen-Zerfall*. Master's thesis, University of Heidelberg (1991).
- [Sai95] K. SAITO and A. W. THOMAS. Phys. Lett., **B 363**, 157 (1995).
- [Sal68] A. SALAM. *Elementary Particle Theory*. Almqvist & Wiksells (1968).
- [Sch89] O. SCHÄRPF. Physica, **B 156 & 157**, 631 (1989).
- [Sch92] C. SCHMIDT. Master's thesis, University of Heidelberg (1992).
- [Sch95] K. SCHRECKENBACH, P. LIAUD, R. KOSSAKOWSKI, H. NASTOLL, A. BUSSIÈRE, and J. P. GUILLAUD. Phys. Lett., **B 349**, 427 (1995).
- [Sch96] P. V. SCHMIDT, L. WILLMANN, R. ABELA, J. BAGATURIA, W. BERTEL, B. BRAUN, H. FOLGER, K. JUNGSMANN, D. MZAVIA, G. ZU PUTLITZ, D. RENKER, T. SAKHELASHVILLI, and L. ZHANG. Nucl. Instr. Meth., **A 376**, 139 (1996).
- [Ser95] A. P. SEREBROV, A. ALDUSHCHENKOV, M. S. LASAKOV, I. A. KUZNETSOV, and I. V. STEPANENKO. Nucl. Instr. Meth., **A 357**, 503 (1995).
- [Ser98] A. P. SEREBROV, I. A. KUZNETSOV, I. V. STEPANENKO, A. ALDUSHCHENKOV, M. S. LASAKOV, Y. A. MOSTOVOI, B. G. EROZOLIMSKII, M. S. DEWEY, F. E. WIETFIELDT, O. ZIMMER, and H. BÖRNER. JETP, **86**(6), 1074 (1998).
- [Sir67] A. SIRLIN. Phys. Rev., **164**(5), 1767 (1967).
- [Str78] C. STRATOWA, R. DOBROZEMSKY, and P. WEINZIERL. Phys. Rev. D, **18**(11), 3970 (1978).
- [Tow77] I. S. TOWNER, J. C. HARDY, and M. HARVEY. Nucl. Phys., **A 284**, 269 (1977).
- [Tow95] I. S. TOWNER and J. C. HARDY. Nucl-th/9504015 (1995).
- [Tow98] I. S. TOWNER and J. C. HARDY. Nucl-th/9809087 (1998).

- [Wei58] S. WEINBERG. Phys. Rev., **112**(1375) (1958).
- [Wei67] S. WEINBERG. Phys. Rev. Lett., **19**, 1264 (1967).
- [Whe67] N. R. WHETTEN. *Methods of Experimental Physics*, vol. 4. Academic Press. Chapter: Secondary Electron Emission (1967).
- [Wil82] D. H. WILKINSON. Nucl. Physics, **377 A**, 474 (1982).
- [Wil95] D. H. WILKINSON. *Proceedings of the Yamada Conference*, 307 (1995).
- [Wu57] C. S. WU, E. AMBLER, R. HAYWARD, D. HOPPES, and R. HUDSON. Phys. Rev., **105**, 1413 (1957).
- [Wu66] C. S. WU and S. A. MOSZKOWSKI. *Beta Decay*, vol. XVI of *Monographs and Texts in Physics and Astronomy*. Interscience Publisher (1966).
- [Yer97] B. YEROLIMSKY, I. KUZNETSOV, Y. MOSTOVOY, and I. STEPANENKO. Phys. Lett., **B 412**, 240 (1997).
- [Zim95] O. ZIMMER. *Spinfilter und Doppelbrechung thermischer Neutronen durch ein polarisiertes Protonentarget*. Ph.D. thesis, TU Munich (1995).
- [Zim99a] O. ZIMMER, T. M. MÜLLER, P. HAUTLE, W. HEIL, and H. HUMBLLOT. Phys. Lett., **B 455**, 62 (1999).
- [Zim99b] O. ZIMMER, P. HAUTLE, W. HEIL, D. HOFMANN, H. HUMBLLOT, I. KRASNOSCHEKOVA, M. LASAKOV, T. M. MÜLLER, V. NESVIZHEVSKY, J. REICH, A. SEREBROV, Y. SOBOLEV, and A. VASSILEV. To be published.